universität wien

DISSERTATION

Titel der Dissertation

„Theory and Spectroscopy on functionalized Graphene and Graphite Intercalation Compounds“

verfasst von

Julio Cesar Chacón Torres

angestrebter akademischer Grad

Doktor der Naturwissenschaften (Dr. rer. nat.)

Wien, 2013

Studienkennzahl lt. Studienblatt:	A 791 411
Dissertationsgebiet lt. Studienblatt:	Physik
Betreuer:	Univ.-Prof. Mag. Dr. Thomas Pichler

Abstract

Intercalation compounds of nanocarbon systems have a broad range of potential applications ranging from Li ion Batteries to organic superconductors with a high transition temperature. The interaction between the intercalant and graphitic systems play a key role in the understanding of their structure as well as the complex interplay between charge transfer and covalency. Especially, the fraction of van der Waals, ionic and covalent character whose interaction is a key for understanding their electronic and optical properties as well as their application potential in superconductivity, and nanoelectronics. In this thesis, I will present a detailed spectroscopic analysis from functionalized Graphene and Graphite Intercalation Compounds (GIC). Three main studies were conducted: (i) Raman and ab-initio analyses in Potassium GICs, (ii) Raman spectroscopy in superconducting graphite compounds, and (iii) Raman spectroscopy of nitrogen doped graphene. In order to be able to conduct the first and the second study, the implementation of a set-up system in which a controlled intercalation and de-intercalation experiment, and Raman measurements can be performed both at the same time, and under high vacuum conditions was crucial, and will be described. Once this system was fully operating, a detailed multi frequency resonant Raman measurements of potassium graphite intercalation compounds (GICs) were performed. From a well controlled and consecutive in situ intercalation and high temperature de-intercalation approach six stages in potassium GICs were obtained. The Raman spectrum of each intercalation stage were recorded, and positions of the G and 2D lines as a function of staging were analyzed. From a lineshape analysis of the spectrum acquired, the contribution of each vibrational mode observed was elucidated, being assigned to each corresponding physical phenomena, and proven by using ab-initio calculations. The results revealed the following: (i) In stage I GICs, the intrinsic Raman lineshape is described by a Fano function, which strongly dependent on the actual defect content in the sample and intercalation region, and has important implications for the electron phonon coupling responsible of superconductivity in this systems. (ii) The Raman response of stages II to VI were acquired. The contribution from the two G-line components and the 2D-line were assigned to a charge transfer and induced strain mechanism within the whole intercalation compound. These results were proven by ab-initio calculations, which revealed that most (but not all) of the transferred charge remains on the graphene sheets adjacent to the intercalant layers, which leads to an electronic decoupling from the single graphene layers, and the ones sandwiched between intercalant. Due to this decoupling, the frequency ob-

served in the 2D-mode was correlated to internal induced strain. (iii) From a combined Raman and XPS analysis of nitrogen doped graphene the effects of dopant bonding configurations on vibrational properties of graphene can be elucidated. The outcomes of this thesis demonstrate that Raman spectroscopy is a very powerful tool to identify the phonon contribution from heavily, and weakly doped carbon compounds. Moreover, it allow us to extract the local internal strain in pristine and weakly charged single, double, and multi-layer graphene by just measuring the frequency of the 2D-line. This strain can additionally be correlated to the in-plane lattice constants of GICs determined by x-ray diffraction. Ab-initio calculations became an outstanding technique to proof charge transfer, structural and vibrational responses in carbon compounds under strain and doping.

Zusammenfassung

Nanostrukturierte Interkalationsverbindungen von Kohlenstoff haben ein breites Anwendungsspektrum von Li Ionen Batterien bis hin zu organischen Hochtemperatursupraleitern. Die Wechswirkungen zwischen den Ionen und dem graphitischen Kohlenstoff sind entscheidend für die Struktur und das komplexe Wechselspiel von Ladungstransfer und kovalenten Bindungen. Das Zusammenwirken von van der Waals, ionischen und kovalenten Kräften bedingt die elektronischen und optischen Eigenschaften, die wiederum die Grundlagen für supraleitende und nanoelektronische Anwendungen sind. Die vorliegende Dissertation beinhaltet eine fundierte spektroskopische Untersuchung von modifizierten Graphen und Graphitinterkalationsverbindungen (GICs). Die drei Schwerpunkte sind: (i) Raman und ab-initio Untersuchungen von Kalium GICs sowie Raman Untersuchungen von (ii) supraleiten GICs und (iii) stickstoffdotierten Graphen. Für die ersten beiden Schwerpunkte musste zunächst ein eigener mobiler Versuchsaufbau entwickelt werden der die kontrollierte thermische Interkalation und Deinterkalation im Hochvakuum und gleichzeitige Ramanmessungen erlaubt. Mit diesem Aufbau wurden dann mehrfärbige resonante Ramanmessungen von Kalium GICs durchgeführt. Durch die Kombination von genau dosierten Interkalations und Deinterkaltionsschritten konnten sechs verschiedene stochiometrische Phasen von K-GICs hergestellt werden. Die Ramanspektren aller sechs Phasen wurden gemessen und die Positionen der G und 2D Linien als Funktion von K/C_{8n} erfasst. Die Profilanalyse der einzelnen Spektren quantifiziert die Beiträge der einzelnen Phononen und ihre jeweilige elektronische Kopplung. Die Daten und Ihre Interpretation sind im Vergleich mit ab-inito Rechnungen bestätigt. Die Ergebnisse sind: (i) In GICs KC_8 ist die intrinsische Linienform eine, stark von der Defektkonzentration abhängige, Fanofunktion. Die zugrunde liegende Kopplung von Phononen und Elektron ist von besonderem Interesse für die Supraleitung in GICs. (ii) Die Ramanspektren der Graphitinterkalationsverbindungen (GICs) KC_8 bis KC_{48} wurden gemessen. Die Beiträge der beiden Komponenten der G und der 2D Linien konnten mit dem Ladungstransfer und den mechanischen Spannungen innerhalb der GICs in Relation gebracht werden. Diese Interpretation wird durch ab-initio Rechnungen unterstuetzt, die einen fast vollständigen Ladungstransfer ausschließlich zu den nächst gelegenen Graphenlagen zeigen, was wiederum eine elektronische Entkopplung der inäquivalenten Graphenlagen bedeutet. Die Verschiebung in der Position der 2D Linie rührt vom den mechanischen Spannungen in den geladenen Graphenlagen. (iii) Die Kombination von Ramanspektroskopie und XPS erlaubt

Besonderheiten im Phononenspektrum von stickstoffdotierten Graphen auf bestimmte Stickstoffbindungsarten zurückzuführen. Die Resultate dieser Dissertation belegen das Ramanspektroskoie ein ideale Methode ist um die Phononenbeiträge von stark und leicht dotieren Kohlenstoffphasen zu identifizieren. Sie ermöglicht uns die intrinsischen Verspannungen im natürlichem und leicht dotierten einzel, doppel oder mehrlagigen Graphen über die Verschiebung der 2D Linie zu messen. Diese Verschiebung lässt sich direkt mit Röntgenstrukturdaten von GICs eichen. Ab-inito Rechnungen sind das Mittel der Wahl um Dotierungs und Spannungs abhängigen Ladungstransfer, Struktur und Phononen in sp^2 Kohlenstoff zu belegen.

Acknowledgement

Over the past years I have received support and encouragement from a great number of individuals. Prof. Dr. Thomas Pichler has been my supervisor and mentor. His support and guidance have made this a thoughtful and rewarding journey possible. I want to thank him for giving me the opportunity to join this big scientific family, in a completely different country and culture which brought me the possibility not only to became a former scientist but also a person with an international and multidisciplinary experience.

Along my PhD, I had the opportunity to meet and interact with highly specialized people during conferences, meetings, research stays, and group discussions. For instance, I would like to thank, Prof. Dr. Ludger Wirtz, who has been my mentor, regarding ab-initio theory. His help to disentangle my experimental observations gave us the opportunity to show up our results in an international journal and conferences.

I want to show my gratitude to Profs. Mauricio Terrones, Paola Ayala, Ferenc Simon, and Drs. Yadira Vega, Fernando Rodríguez, and Florentino López who introduced and though me along the first steps of my PhD. Also thanks to the Electronic Properties of Materials' Group at the University of Vienna, colleges and partners who were always there for me when I needed them.

I want to specially thank my wife Fany Mendez, and my family who fully supported me to move to Vienna, and gave me the courage to continue every time I was almost giving up.

Last but not least, I want to acknowledge the financial support of the project FWF-I377-N16, and the OEAD AMADEUS PROGRAM financing.

Julio Cesar Chacón Torres
Wien, 2013

Statutory Declaration

I declare that I have authored this thesis independently, that I have not used other than the declared sources / resources, and that I have explicitly marked all material which has been quoted either literally or by content from the used sources.

Wien, _____ _____

Place, Date Signature

Eidesstattliche Erklärung

Ich erkläre an Eides statt, dass ich die vorliegende Arbeit selbstständig verfasst, andere als die angegebenen Quellen/Hilfsmittel nicht benutzt, und die den benutzten Quellen wörtlich und inhaltlich entnommene Stellen als solche kenntlich gemacht habe.

Wien, am _____ _____

Ort, Datum Unterschrift

Preface

All of the work presented henceforth was conducted in the Electronic Properties of Materials group at the University of Vienna, Faculty of Physics; and in collaboration with the Department of Chemistry, University of Liverpool UK, the Department of Physics and Astronomy at Clemson University USA, and the Physics and Material Sciences Research Unit, Campus Limpertsberg, University of Luxembourg.

During this work I was responsible for all major areas of concept formation, data collection and analysis, as well as manuscript composition under the supervision of Prof. Dr. Thomas Pichler. The theoretical calculations were conducted by Prof. Dr. Ludger Wirtz at the University of Luxembourg. Regarding Chapter 4.5, I was involved throughout the project in the Raman characterization of the samples, and data analysis for the manuscript composition while the main manuscript preparation, and data analysis was performed by Dr. R. Podila at Clemson University.

The results of this thesis have helped to clarify and provide additional information to the open questions around graphite intercalation compounds, and graphene functionalization, doping and induced strain by introducing a controlled in-situ doping system from where Raman spectroscopy can be measure with out exposing the samples to air. Chapters 4.1, 4.2, 4.3, 4.4, and 4.5 have been published a long this PhD work in peer reviewed journals as: ACS Nano, Physical Review B, and Physica Status Solidi B: Basic Solid State Physics.

Contents

Chapter 1

INTRODUCTION

1.1. Graphene based materials, an overview

Graphene, as a new material and "the mother of all graphitic forms" [1] has been considered as the building material for any sp^2 hybridized carbon allotrope. The term *graphene* first appeared in 1987 [2] to describe single layers of graphite, and as one of the components in graphite intercalation compounds (GICs). However, at the very first time, graphene was not considered as a real material since theoretically predicted that 2D crystals are thermodynamically unstable and could not exist in a free state [3, 4]. Nevertheless, different efforts were performed in order to synthesize graphene from a top-down approach by trying to split graphite into individual sheets in a mechanical or chemical way. While looking for the precious 2D graphene, different low dimensional carbon allotropes were discovered like fullerenes [5] (0D and Nobel Prize in Chemistry 1996 to Robert F. Curl Jr., Sir Harold W. Kroto and Richard E. Smalley), and carbon nanotubes (1D) [6] in 1985 and 1991, respectively. In 2004, finally the first experimental evidence of graphene was obtained by Andre Geim, and Konstantine Novoselov [1] Nobel Prize in 2010 "for groundbreaking experiments regarding the two-dimensional material graphene" by introducing the "Scotch tape method", in which a piece of tape is used to peel graphene flakes off of a chunk of graphite. This discovery resulted in single- and few-layer graphene flakes pinned on silicon substrates by only van der Waals forces and could be made free-standing by etching away the substrate [1, 7–10], which allowed scientists to probe graphene's intrinsic properties.

The first studies in graphene, revealed exceptional electrical [11, 12], thermal [13], and mechanical [14] properties. For instance, an ambipolar field effect [11], the quantum Hall effect at room temperature [12, 15–19], measurements of extremely high carrier mobility [9] and even the detection of a single molecule absorption events [20, 21] were observed; which highlighted the importance of graphene. These properties generated a huge interest in the possible implementation of graphene into devices, and various applications (e.g., field effect transistors (FETs), sensors, electrochemical capacitors/super capacitors, lithium ion batteries (LIBs), fuel cells, and solar cells) [22], all of which are included in the future generations of high-speed and radio frequency logic devices, thermal and electrical conductive composites, sensors, as well as trans-

parent electrodes for displays (e.g. organic light-emitting diodes, LEDs) and solar cells. Nevertheless, the investigation regarding applications of graphene-based materials has just begun, and many challenges and opportunities still remain. Despite the intense interest and continuing experimental success reported by applied physics and device fabrication, the implementation of graphene widespread has yet to occur. The later is based in the difficulty and reliably of producing high quality samples, especially in any scalable way [23]. The challenge here is obtaining the optimum performance, which directly depends on the number of graphene layers present and the general quality of the crystal lattice. Also, in order to enable applications in batteries, super capacitors, separation technologies, and as support for catalysis, the hierarchical structure of graphene assemblies must be controlled to make the surface of individual sheets maximally accessible [24], which is still not completely accomplished. An open gate to improve the performance of these graphene based devices has been revealed by combining graphene with composites. For example, graphene-nanocrystal composites (graphene-NC) [25] have been considered as one of the promising alternatives to electrode materials in energy devices due to the superior electrical conductivity, high specific surface area, and good chemical stability of graphene and high electrochemical/electro-catalytic activities from the NC. Recent studies have shown considerably improvement in its performance in energy storage/conversion devices [25, 26].

Finally, the properties of graphene hold a wide opportunity branch combining them not only with polymers but also with another functional nanomaterials to form hybrid nanostructures with properties tailored for intended applications, as early observed in graphite intercalation compounds [27]. Graphene-based hybrid materials open up new frontiers in science and technology and expand the scope of graphene's applications as synergetic effects can result from the interaction between graphene and the nanomaterials supported on it. For instance, GICs offer the possibility to change the electronic properties of graphene turning it into a superconducting material [28]. Thus, the study of graphene and functionalized graphene turned back into graphite and GICs, which bring out the importance of this initial raw material from where this research on carbon has began, and from where intrinsic properties of graphene can be directly extracted as it will be shown a long this thesis work.

1.2. Graphite and Graphene

In this chapter I will introduce the physical, structural and electronic characteristics of graphene as the understanding of them is indispensable for this thesis.

Graphite is a mineral with hexagonal lattice (see Fig. 1.1). It has been the starting material to study graphene by chemical exfoliation. Graphite originates as the final product of metamorphism* of either carbon bearing fluids or carbonaceous matter [30]. It also occurs in igneous rocks and in meteorites [31]. Graphite is an anisotropic material conformed of graphene layers stacked one on top of the next one. It is considered a good electrical and thermal conductor along the layers, while they are poor perpendicular to the layers. This fact is caused due to the strong

*In geology metamorphism refers to the changes in mineral assemblage and texture that result from subjecting a rock to conditions such pressure, temperature, and chemical environments different from those under which the rock originally formed [29].

in-plane metallic bonding between carbon atoms, in contrast to the weak van der Waals forces between the layers. Thus, it has been used for electro-chemical and arc discharge electrodes, as well as electric brushes. As a result of graphite anisotropy, the carbon layers which conform it can slide with respect to one another quite easily, which make graphite a good lubricant, pencil material [32], and graphene precursor. Graphite consists of a lamellar arrangement of carbon atoms in hexagons with sp^2 hybridization yields a hexagonal lattice, with a 3D crystal structure, which belongs to the $P6_3/mmc$ (D^4_{6h}) space group. Each layer locates on top of the next one in a Bernal stacking which implies that half of the carbon atoms in the boundary layer are located in the center of the hexagons of the neighboring plane (ABA-stacking in the hexagonal structure) [33]. In Fig. 1.1 c) the lattice parameters of graphite are represented in a schematic model. The separation between carbon atoms is $a = 1.42\mathring{A}$, and $c = 3.35\mathring{A}$ between each layer. There are 4 atoms per unit cell, labeled as A, A$'$, B and B$'$ in Fig. 1.1 c). The atoms A and B are on one layer plane and the atoms A$'$ and B$'$ are on a boundary layer plane displaced by the crystallographic *c-axis* distance. The atoms A and A$'$ differ from the atoms B and B$'$ in the sense that the A and A$'$ atoms have neighbors directly above and below in the adjacent layer planes whereas atoms B and B$'$ do not have neighbors on top or bellow due to the ABA-stacking. The bonding between each layer in graphite is the result of a van der Walls interaction which comes from the delocalized π-orbital in the A atoms. The structure of graphite was determined, and confirmed in 1924 by using X-ray diffraction by Bernal J.D. [34]. The case of graphene is simpler than graphite as it has the same hexagonal arrangement of atoms, but it is not repeated along the *c-axis* (z direction in Fig. 1.1 c). It has a lattice parameter of $a = 1.42\mathring{A}$ and belongs to the P3m space group. On the one hand, graphene exhibits a high crystal quality that electrons can travel sub-micrometer distances without scattering, which makes XRD diffraction not a suitable characterization technique. Thus, graphene's atomic structure has been proven by employing transmission electron microscopy (TEM) of graphene layers directly suspended in between metallic grids [7], which has offered an ample scope for fundamental research and new technologies.

Turning into graphene, this material is a single planar carbon layer in a honeycomb arrangement (see Fig. 1.1 b) and can be produced from a mechanical or chemical exfoliation of graphite, organo-chemical synthesis and/or chemical vapor deposition [35]. It is formed of carbon atoms arranged in a 2D honeycomb lattice. Its importance comes from the fact that it is a purely 2D material with exceptional properties. From the electronic side, it is a zero-gap semiconductor and electrons can flow very quickly through this sheet even at room temperature. As this layer has one atom thickness, it is almost transparent which makes it to be extremely interesting for optical applications. Graphene also exhibit interesting mechanical properties with spring constants ranging from 1 to 5 N/m in suspended graphene sheets, and Young's modulus of 0.5 T Pa with tensions of hundreds of nanonewtons [14]. Last, but not least, graphene's properties could lead to a revolution in many technological applications as mentioned before such as: Flexible touchscreen displays [36], Graphene for terahertz electronics [37], Electrochemical applications of graphene [38], and Graphene sensors [25] which makes the study of graphene a very exiting and promising research field. For all these potential applications, the basic understanding of the physical properties is an indispensable prerequisite. In order to understand the physical properties of graphite, and graphene, one need to understand and study how the atoms or molecules of

this material are arranged in their *crystal structure*, and how this influences the electronic and optical properties [39].

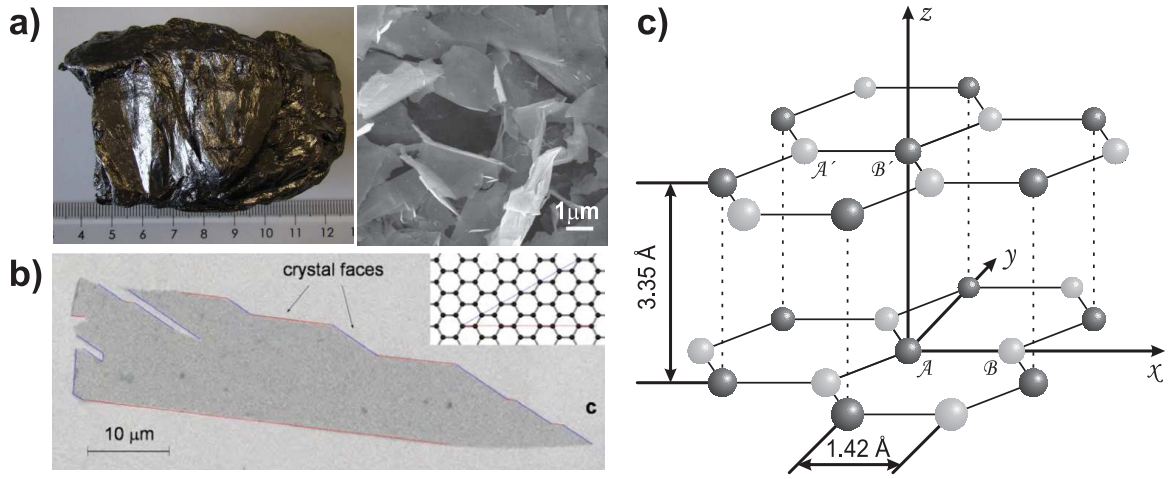

Figure 1.1.: In the left panel of a), a natural graphite rock from mine in presented. The right panel of a) is a micrography of graphite flakes after exfoliation of natural graphite taken from Ref. [40]. b), A graphene sheet freely suspended on a micron-size metallic scaffold [1]. c), Crystal structure of graphite reproduced from Ref [32].

1.2.1. Electronic properties, crystal structure and Brillouin zone

The electronic properties of graphene and graphite come directly from their chemical composition. Both contain only carbon atoms, whose electronic configuration is $1s^2 2s^2 2p^2$ and hence 4 valence electrons are available for bond formation. The $1s^2$ electrons are part of to the ion core, while the remaining four are valence electrons. These electrons in the $2s$ and $2p$ orbitals have the possibility to form three kind of hybridizations: sp, sp^2, and sp^3. Typical examples of these hybridizations are: 1D carbyne (sp); fullerenes (0D), carbon nanotubes (1D), graphene (2D) and graphite (3D), all of them sp^2 hybridized; and diamond which corresponds to sp^3 hybridization. According to their electronic configuration, the properties of each carbon allotrope can exhibit a different electronic behavior as described in Fig. 1.2. There we can observe the different kind of electronic bands for different carbon materials. For example: graphite, as a semi-metal, exhibit a gap between the conduction and the valence band. In this case, the bands are near enough to the Fermi level to be thermally populated with electrons or holes leading into p- or n-type doping characteristic in GICs. On the other hand, carbon nanotubes can depict two different kind of behavior either as an insulator or as a metal. Insulators exhibit a gap between the conduction and the valence band, where the E_F lies, while in metals these bands tend to overlap crossing the Fermi level. The last two novel carbon materials are fullerenes and graphene, from which the first one acts as an insulator, meanwhile graphene has a zero gap between the conduction and the valence bands, being this one of its most interesting intrinsic properties.

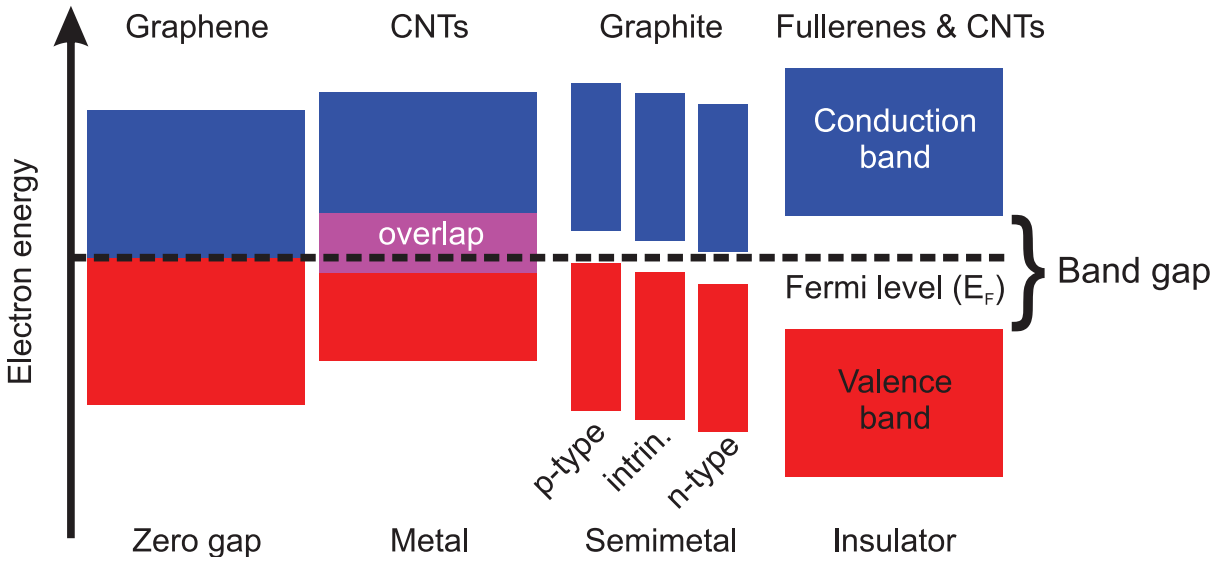

Figure 1.2.: Schematic filling of electronic band structure diagram in various types of materials. at equilibrium.

In graphene, every carbon atom has a covalent bond to three in-plane nearest neighbors. Each of these bonds have a sp^2 hybridization and give rise to three orbitals called σ and a perpendicular delocalized π-orbital (see Fig. 1.3 a). The π-orbital is crucial when analyzing the electronic and optical properties in graphene and graphite as it is strongly influenced by environments which can introduce or extract charge into the system. One way to study the behavior of this orbital, is by solving the electronic structure of the crystal. In case of graphite and graphene, 3D and 2D structures govern their electronic properties respectively. The unit cell of graphene is a rhombus which includes two carbon atoms (A and B) as depicted in Fig. 1.3 b). These atoms can not be connected using unit vectors $\vec{a}_1$ or $\vec{a}_2$, which means that they are inequivalent. These unit vectors have lengths of $|\vec{a}_1| = |\vec{a}_2| = \sqrt{3}a_0 = a$, where a_0 is the C-C distance (1.42Å). Their coordinates are given by:

$$\vec{a}_1 = \frac{a}{2}\left(\sqrt{3}\hat{x}+\hat{y}\right) \qquad \text{and} \qquad \vec{a}_2 = \frac{a}{2}\left(-\sqrt{3}\hat{x}+\hat{y}\right) \tag{1.1}$$

The first Brillouin zone (1st BZ) in graphene is represented by the reciprocal vectors $\vec{b}_1$ and $\vec{b}_2$ depicted in Fig. 1.3 c). These vectors are given by the condition $\vec{b}_i \cdot \vec{a}_j = 2\pi\delta_{ij}$, and can be written as:

$$\vec{b}_1 = \frac{2\pi}{a}\left(\frac{\sqrt{3}}{3}\hat{k}_x+\hat{k}_y\right) \quad \text{and} \quad \vec{b}_2 = \frac{2\pi}{a}\left(\frac{-\sqrt{3}}{3}\hat{k}_x+\hat{k}_y\right) \tag{1.2}$$

Graphene diverges from the majority of the three-dimensional materials due to its intrinsic zero-gap semiconductor behavior. The understanding of its electronic structure, must be considered the starting point in finding the band structure of graphite. In 1947 P. R. Wallace [41] showed a

linear relation for energies at the k-space in graphene (reciprocal space), in which (at low energies) the six intersections of the two-dimensional hexagonal Brillouin zone lead to a negligible effective mass for electrons and holes [42]. Due to this linear or "conical" dispersion effect, observed at low energies, the electrons and holes around these six high symmetry points used to behave like relativistic particles, and can be described by using a Dirac equation for spin-1/2 [43, 44]. Hence, the electrons and holes are called Dirac fermions also called graphinos [45], and the six corners of the Brillouin zone are called Dirac points [43]. The equation from which the energy in the reciprocal space (E($\hat{k}$))can be described is $E = \hbar v_F \sqrt{k_x^2 + k_y^2}$; where the Fermi velocity $v_F \simeq 10^6$ m/s [44].

Throug the time, many studies have been performed to examine the influence of interactions between graphene planes in hexagonal graphite and lead to the standard model of energy bands called Slonczewski and Weiss-McClure or "SWMcC" approximation [46, 47]. The simulation of the electronic band structure in graphitic materials has been regularly done using a tight-binding model (TB model) calculations, which is an approach that uses a set of wave functions based upon superposition of wave functions for isolated atoms located at each atomic site belonging to the graphene planes, and taking into account the first, second, or even third nearest neighbors for more accuracy [33, 48]. In order to disentangle the difference between each approximation model, one can start from deriving the most general form of a tight-binding Hamiltonian H, with an overlap matrix S,

$$\begin{vmatrix} H_{AA}(k) - E(k)S_{AA}(k) & H_{AB}(k) - E(k)S_{AB}(k) \\ H^*_{AB}(k) - E(k)S^*_{AB}(k) & H_{AA}(k) - E(k)S_{AA}(k) \end{vmatrix} = 0 \tag{1.3}$$

where $E(k)$ are the electronic eigenvalues. By considering two equivalent carbon atoms A and B carbon in a graphene layer. The solution to Eq. 1.3 can be written as:

$$E(k)\pm = \frac{-(-2E_0 + E_1) \pm \sqrt{(-2E_0 + E_1)^2 - 4E_2E_3}}{2E_3} \tag{1.4}$$

where the electronic eigenvalues are

$$\begin{aligned} E_0 = H_{AA}S_{AA} \qquad E_1 = S_{AB}H^*_{AB} + H_{AB}S^*_{AB} \\ E_2 = H^2_{AA} - H_{AB}H^*_{AB} \qquad E_3 = S^2_{AA} - S_{AB}S^*_{AB} \end{aligned} \tag{1.5}$$

Once that the Hamiltonian Eq. 1.3 has been solved, the nearest-neighbor tight-binding dispersion as in Ref. [49] can be derived. Considering an atom A_0 as shown in Fig. 1.4 a) whose nearest neighbors are B_{11}, B_{12}, and B_{13}, we can define the terms H_{AA} and H_{AB} from our Hamiltonian as the following:

$$\begin{aligned} H_{AA} = \tfrac{1}{N} \textstyle\sum_{R_A} \sum_{R_{A'}} e^{ik(R_{A'} - R_A)} \langle \varphi_A(r - R_A) | H | \varphi_A(r - R_{A'}) \rangle \\ H_{AA} = \tfrac{1}{N} \textstyle\sum_{R_A} \langle \varphi_A(r - R_A) | H | \varphi_A(r - R_{A'}) \rangle = \varepsilon_{2p} \end{aligned} \tag{1.6}$$

Where N is the number of unit cells in the crystal, R_A and $R_{A'}$ are the radius positions of atoms A and A', respectively, and φ_A denotes the p_z atomic wave functions, which brings the basis for the crystal Bloch functions. The overlap matrix element S_{AA}=1, by assuming a normalization of the atomic wave function $(\varphi_A(r-R_A)|H|\varphi_A(r-R_{A'}=1)$. In order to find H_{AB}, one should sum over the three nearest neighbors components shown in Fig. 1.4 a)

$$\begin{gathered} H_{AB} = \frac{1}{N}\sum_{R_A}\sum_{R_B} e^{ik(R_B-R_A)}\langle\varphi_A(r-R_A)|H|\varphi_B(r-R_B)\rangle \\ H_{AB} = \gamma_0(e^{ikR_{11}} + e^{ikR_{12}} + e^{ikR_{13}}) \end{gathered} \tag{1.7}$$

where $\gamma_0 = \langle\varphi_A(r-R_A)|H|\varphi_B(r-R_{1i})\rangle\,, \quad (i=1,2,3)$. The same treatment applies to the overlapping matrix element

$S_{AB} = s_0(e^{ikR_{11}} + e^{ikR_{12}} + e^{ikR_{13}})$ leading $s_0 = \langle\varphi_A(r-R_A)|\varphi_B(r-R_A-R_{1i})\rangle\,, \quad (i=1,2,3)$

where R_{1i} is the vector pointing from the atom A_0 to atoms B_{1i} in Fig. 1.4 a). By introducing the Hamiltonian, and the overlap matrix into Eq. 1.4 and 1.5, the following function can be defined:

$$\begin{gathered} f(k) = 3 + u(k) \\ = 3 + 2cos(k\cdot a_1) + 2cos(k\cdot a_2) + 2cos(k\cdot(a_1-a_2)) \\ = 3 + 2cos(2\pi\, ak_1) + 2cos(2\pi\, ak_2) + 2cos(2\pi\, a(k_1-k_2)) \end{gathered} \tag{1.8}$$

where the components of a wave vector k in units of the reciprocal graphene lattice vectors k_1 and k_2 are $k_i = k\cdot(a_i/2\pi)$, from where the well-known result [49] revealed as:

$$E\pm(k) = \frac{\varepsilon_{2p} \pm \gamma_0\sqrt{f(k)}}{1 \pm s_0\sqrt{f(k)}} \tag{1.9}$$

The parameters ε_{2p}, γ_0, and s_0 are found by fitting experimental or first-principles data. A universal set of third-nearest-neighbor tight-binding parameters has been presented by Grüeneis et al. [50] (Table 1.1 for calculation of the quasi-particle (QP) dispersion of N stacked sp^2 graphene layers ($N=1,\ldots,\infty$) with AB stacking sequence. These parameters were also fit to ab-initio calculations, allowing to describe the whole π "experimental" band structure of graphite, by using just one set of parameters. The later is important to describe low-energy electronic transport and high-energy optical properties of graphene layers.

The nearest-neighbor tight-binding derivation of graphene was initially performed to study the low-energy properties of graphite as the coupling between graphene layers. Its importance comes regarding the interaction between graphene and further intercalants in GICs, and/or substrates as shown by Allard, *et al.* [51]. The results from this TB calculations are shown in Fig. 1.4 c), where the improved set of TB-GW parameters where used in order to determine the electronic band dispersion of multilayer graphene considering a three dimensional cell-structure Fig. 1.4 b) with nearest neighbors A_1 B_1, and A_2 B_2.

Table 1.1.: 3rd nearest-neighbor tight-binding parameters for few-layer graphene and graphite. All values except the ones for s_0^1 s_0^2, and s_0^3 are in eV. These parameters are valid in the 3D, and 2D regime (graphite and graphene) [50].

Method	γ_0^1	γ_0^2	γ_0^3	s_0^1	s_0^2	s_0^3	γ_1	γ_2	γ_3	γ_4	γ_5	E_0	Δ
3NN TB-GW	-3.4416	-0.7544	-0.4246	0.2671	0.0494	0.0345	0.3513	-0.0105	0.2973	0.1954	0.0187	2.2624	0.0540
3NN TB-LDA	-3.0121	-0.6346	-0.3628	0.2499	0.0390	0.0322	0.3077	-0.0077	0.2583	0.1735	0.0147	-1.9037	0.0214

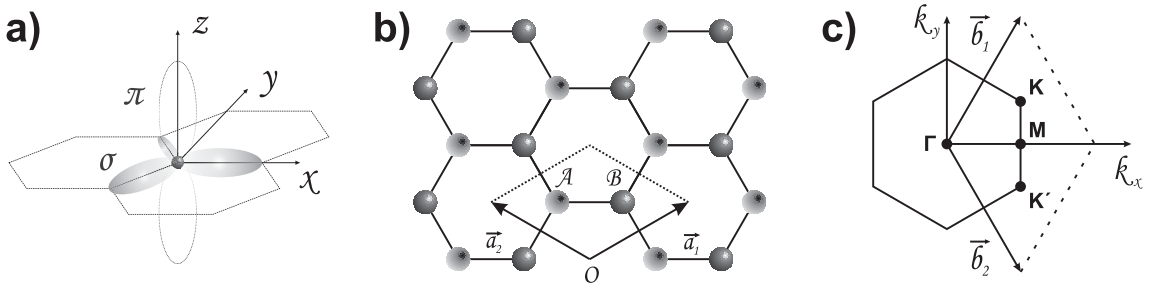

Figure 1.3.: Honeycomb lattice, orbitals and its Brillouin zone of graphene. a) Three σ in-plane orbitals are represented, and two delocalized π-orbitals. b) Lattice structure of graphene, made out of two atoms (A,B) enclosed in a rhombic lattice where a_1 and a_2 are the lattice unit vectors. c) Corresponding Brillouin zone. The high symmetry points are labeled as Γ, **K**, and **M**. The Dirac cones of graphene locate at the **K** and **K**′ points.

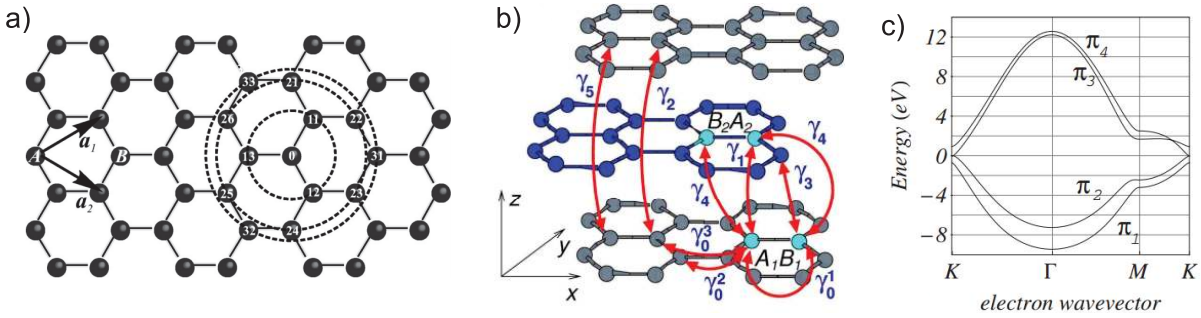

Figure 1.4.: a) Graphene hexagonal lattice based in two atoms (A and B). An arbitrary atom A_0 has three nearest neighbors B_{1i}, ans six next-nearest neighbors, and three second nearest neighbors (A_{2i}, and B_{3i} respectively). b)3D Graphite unit cell consists of four atoms (A_1, B_1, A_2, and B_2) in light-blue. The red arrows denote the interatomic tight-binding hopping matrix elements γ_0^1, γ_0^2, γ_0^3, γ_1, ..., γ_5. The overlap matrix elements s_1, s_2, and s_3 not shown couple the same atoms as γ_0^1, γ_0^2, and γ_0^3. c) Calculated TB-GW graphite dispersion along the high symmetry points **K** Γ **M** **K**. Figure adapted from Refs. [48, 50]

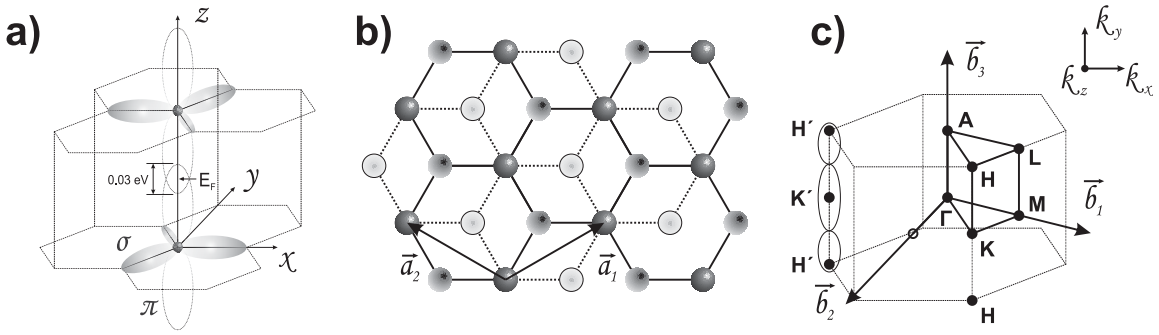

Figure 1.5.: 3D graphitic lattice, orbitals and 1st BZ. a) The σ in-plane orbitals are represented in each layer plus two overlapped π-orbitals. Temporary dipoles effect in graphite creates an attraction between carbons' A forming weak bonds – Van der Waals' force– b) There are four atoms per unit cell in graphite, namely atoms A, B, A$'$ and B$'$ enclosed in a rhombic lattice where a_1, a_2 and a_3 are their lattice unit vectors. c) Corresponding 3D-Brillouin zone. The high symmetry points are labeled as Γ, **K**, **M**, **L**, **A** and **H** in k-space.

Turning into the 3D-graphite, first it must be pointed that the hexagonal mesh of graphite contains four atoms and the π electrons give rise to four energy bands instead of just two as it is in graphene [52]. Hence, in addition to the in-plane wave vector k, an additional perpendicular k_z vector will be introduced as an anisotropic parameter and explained in detail in the following:

Graphite has a layer structure in which the atoms are arranged in a hexagonal pattern within each layer and the layers are stacked in AB sequence [34], which results in a hexagonal unit cell. The translation vectors of the graphite crystal structure are shown in Fig. 1.5 b), as:

$$\vec{a}_1 = \frac{a}{2}\left(\sqrt{3}\hat{x}+\hat{y}\right) \qquad \vec{a}_2 = \frac{a}{2}\left(-\sqrt{3}\hat{x}+\hat{y}\right) \qquad \vec{a}_3 = c\hat{z} \tag{1.10}$$

where a is the lattice constant and $c = 6.6708\mathring{A}$. The reciprocal lattice vectors $\vec{b}_1$, $\vec{b}_2$ and $\vec{b}_3$ can be written as:

$$\vec{b}_1 = \frac{2\pi}{a}\left(\frac{\sqrt{3}}{3}\hat{k}_x+\hat{k}_y\right) \qquad \vec{b}_2 = \frac{2\pi}{a}\left(\frac{-\sqrt{3}}{3}\hat{k}_x+\hat{k}_y\right) \qquad \vec{b}_3 = \frac{2\pi}{c}\hat{k}_z \tag{1.11}$$

In graphite, each carbon atom has four valence electrons and there are four atoms per unit cell. Therefore, there exist 16 energy bands from which 12 are σ-bands and 4 are π-bands (exemplified in Fig. 1.5 a). From the twelve σ-bands, six are bonding and six are anti-bonding, being separated

by 5 eV. In between those two groups lie the π-bands. Two π-bands are bonding and two are anti-bonding ones. Every band is coupled, while in order to preserve the hexagonal structure in graphite, the four π-bands are strongly coupled. Graphite holds 16 electrons per unit cell, from which 8 energy bands are filled. In the middle of the four π-bands lies the Fermi level. The highest valence band (π-bands), overlap at the Brillouin zone edges **HKH** and $\mathbf{H}'\mathbf{K}'\mathbf{H}'$, making graphite a semi-metal. The overlap energy of the valence band is about 0.03 eV (see Fig. 1.5 a). The corresponding Fermi surface is formed by three elongated pockets with a trigonal distortion along the **HKH** or $\mathbf{H}'\mathbf{K}'\mathbf{H}'$ edges of the hexagonal BZ and correspond to different charge carriers (a pocket of holes in the center and electrons on both sides) [33]. In three dimensions, the energy bands, high symmetry points and reciprocal vectors are shown in Fig. 1.5 c).

1.2.2. Phonon Dispersion and Lattice Vibrations

The lattice vibrations in a crystal are described by phonons. The vibrational modes of an atomic crystal lattice depends only on the crystal structure, as predicted by the group theory in their corresponding irreducible representation [53]. These vibrations are separated into three acoustic modes, a wave vector and the number of optical modes relative to finite frequencies when two ore more atoms are present in the unit cell. The frequencies of normal modes directly depends on the force constants whose direction is defined by the atomic displacement respect to the coherent motion of the excitation wave leading in two possibilities: longitudinal (L) or transverse (T) modes [33]. Depending on the type of movement and the lattice symmetry, the vibrations may present or not a change in the dipole moment, which for instance will introduce changes in the electronic charge. This situation leads to a coupling of the electromagnetic radiation with the electric field and the absorption phenomenon. Thus, a vibration mode is active by IR spectroscopy when dipole moment changes are present during the vibration [54]. In the case of Raman scattering, a vibration mode will be active if the electronic polarization is changed by the vibrational mode. Summarizing, antisymmetric vibrational modes (called *u* for ungerade) which belong to polar IR active groups, and the symmetric modes (also called *g* for gerade) which are Raman active.

Now, being N the number of atoms in the unit cell of a crystal, there exist in total $3N$ phonon branches. In graphene there are two atoms per unit cell and consequently six phonon branches. In a 3D crystal like graphite, there are three acoustic branches which implies another three optical phonons. The phonon modes, optical and acoustic, have been confirmed by various experimental [58–65] and theoretical [55, 66, 67] studies. When investigating the physical properties of graphite, one can take into account only a single hexagonal plane of carbon atoms (graphene), due to the weak interaction between the layers. However, even a weak interaction can alter the selection rules in a crystal. Graphene belongs to the D_{6h} symmetry group with six vibrational modes identified in the center of the 1st BZ [68]. According to group theory, they can be summarized in the following irreducible representation:

$$\Gamma = A_{2u} + 2B_{1g} + E_{1u} + 2E_{2g} \tag{1.12}$$

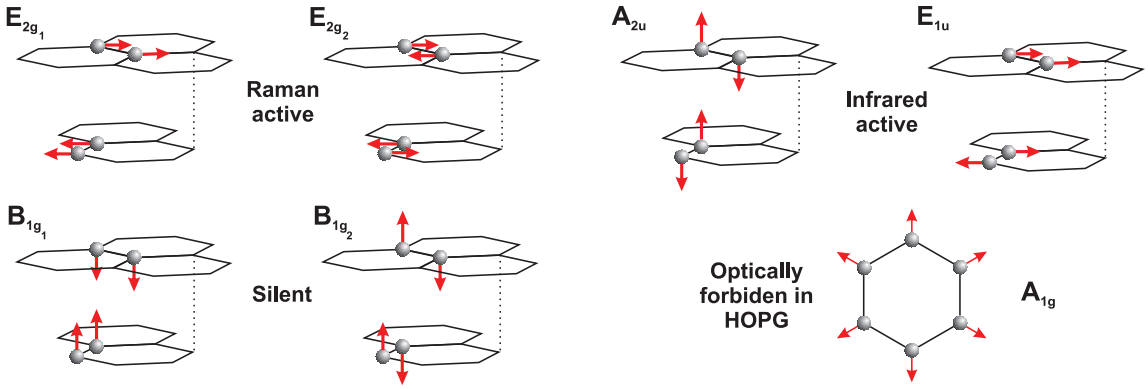

Figure 1.6.: Γ-point phonon-displacement pattern for graphene and graphite. Gray spheres represent inequivalent carbon atoms. Red arrows show atom displacements. The phonon mode which give rise to each vibration is labeled as Raman-active (R), infrared-active (IR) and silent (inactive) modes. In the bottom right of the figure, the atom displacement for the A_{1g} mode at K is shown, this mode is forbidden in Highly Oriented Pirolytic Graphite (HOPG). Figure adapted from [55–57]

The A_{2u} and E_{1u} representations are IR active; the B_{1g} mode is a doubly degenerated optical phonon mode, in which the carbon atoms move perpendicular to the graphene planes. The E_{2g} mode, also doubly degenerated, is an in-plane optical Raman active vibration . These different atomic vibrations are represented in Fig. 1.6. Two of those modes are not detectable (silent); two are observable only by IR and two by Raman spectroscopy. In the case of Graphite, it has four atoms per unit cell ($N = 4$), thus twelve vibrational modes, consisting of three acoustic modes ($A_{2u} + E_{1u}$), three IR active ($A_{2u} + E_{1u}$), four Raman active ($2E_{2g}$), and two silent modes ($2B_{1g}$) [56]

The phonon dispersions of single-layer graphene (SLG) comprise three acoustic (A) and three optical (O) branches. The modes with out-of-plane (Z) motion are considerably softer than the in-plane longitudinal (L) and transverse (T) ones [61]. In Fig. 1.7 a), the phonon dispersion relations for 3D graphite are represented from inelastic x-ray scattering (IXS) [69]. The direct comparison from the experimental IXS to the GW ab-initio calculations are in perfect agreement, disentangling the contribution from each phonon. As can be seen, the three branches are almost touching each other at K, revealing the TO phonon to be the responsible from the kink in the ARPES measurements of doped graphene layers. For comparison, in Fig. 1.7 b), the phonon dispersion of ab-initio calculations [66] of a 2D graphene sheet is depicted. With out considering the fact that the y-scale is different in both graphs, very little difference is detected between the structure of the 2D and 3D phonon density of states. This is due to the weak inter-planar coupling in graphite.

In order to further study these optical and acoustic phonons in graphite and graphene, one can directly relate the eigenvectors for the optically allowed Γ-point vibrations for graphite from

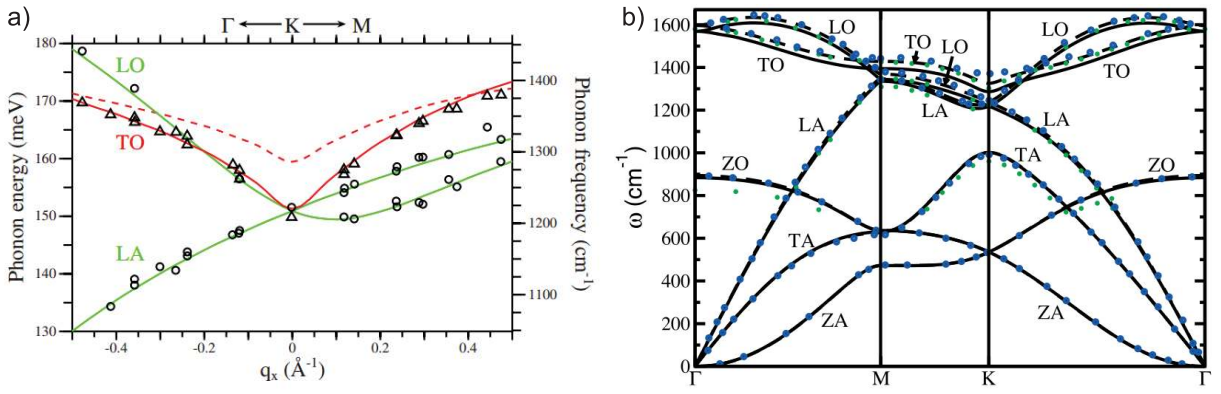

Figure 1.7.: Graphite and Graphene dispersion modes of acoustic and optical phonons versus wave vector in *k*-space. In panel a) the phonon dispersion of graphite from inelastic x-ray scattering (symbols) are compared to GW ab-initio calculations (solid line) are shown. In the right-side b) phonon dispersion of graphene by ab-initio calculations is presented (solid line) and compared with LDA, and GGA calculations (green and blue dots). Figures obtained and adapted from [69] and [66] respectively.

the phonon dispersion in Fig. 1.7 a). The importance of these phonon dispersions have shown two Kohn anomalies at the Γ-E_{2g} and **K**-A_1 modes [69, 70]. The anomalies were revealed by the presence of two sharp kinks with a slope proportional to the square of the electron-phonon coupling. Thus, from extracting the phonon dispersion in graphite, one can directly determine the EPC responsible for superconducting GICs. The frequency where each vibrational mode can be observed are: E_{2g_1} at 42 cm^{-1}, and E_{2g_2} at 1582 cm^{-1} Raman active; double degenerated E_{1u} at 1588 cm^{-1}, and non-degenerate A_{2u} at 868 cm^{-1} IR active; and finally a two doubly degenerated B_{1g} mode at 127, and 870 cm^{-1} neither Raman nor infrared-active. The graphical representation of these modes in the case of graphene, is explained in Fig. 1.8 as optical transitions between the π and π^* bands, and its experimental counterpart (Raman spectrum).

The doubly degenerated (iTO and LO) phonon mode (E_{2g} symmetry) at the Brillouin zone are named G-band in Raman spectroscopy. This is the unique band which comes from a normal first order Raman scattering process in graphene (left side Fig. 1.8 a). The double-resonance process shown at the center and right side of Fig. 1.8 a) begins with an electron of wave-vector *k* around **K** absorbing a photon of energy E_{laser}. The electron is inelastically scattered by a phonon or a defect of wave vector *q* and energy E_{phonon} to a point belonging to a circle around the **K** point, with wave vector $k+q$, where **K'** point is related to **K** by time reversal symmetry [71]. The electron is then scattered back to a *k* state, and emits a photon by recombining with a hole at a *k* state. In the case of the D-band, the two scattering processes consist of one elastic scattering event by defects of the crystal and one inelastic scattering process by the emission or absorption of a phonon, as shown in Fig. 1.8 a). The result from this double resonance process are the G' and D-bands which involve two iTO phonons near the **K** point for the G' band or one iTO phonon and one defect in the case of the D-band. Since the G' band is approximately twice the D band frequency, some authors define it as 2D-band for the case of graphene and graphite [72]. In the special case of graphene, where the valence and conduction bands are almost mirror bands of one another

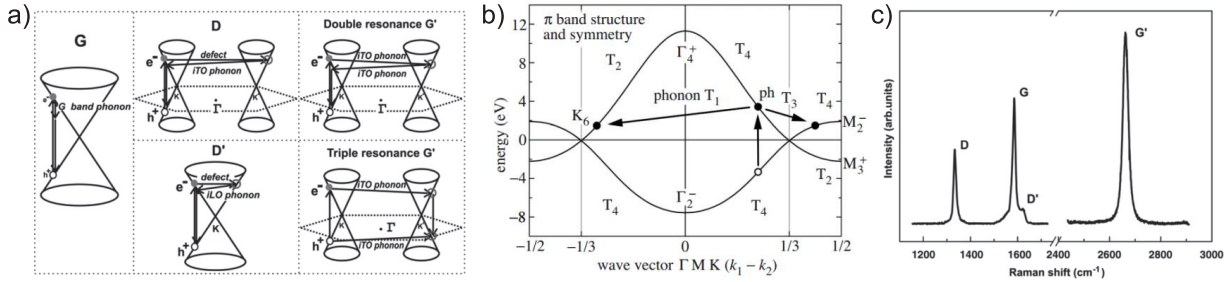

Figure 1.8.: a) First, second, and third resonant processes for mono-layer graphene [75] b) Electronic band structure and symmetry of the π and π^* states in graphene along the Γ **M** **K** direction [55] c) Raman spectrum of a graphene showing the main Raman features, D, G and G'-bands, taken with a laser excitation energy of 2.41 eV [75]

relative to the Fermi energy, an important effect takes place, the "triple resonance (TR) Raman process" [73]. The TR process in Fig. 1.8 a) considers, instead of the electron being scattered back by a phonon with wave vector $-q$, that the hole will be scattered by a wave vector $+q$. In this case, the electron-hole generation is a resonant process, in which both the electron and hole scattering processes will be resonant, and finally the electron-hole recombination at the opposite side with respect to the K point will also occur near the **K** point between an electron and a hole in resonance states. Therefore, for TR all steps in the usual double resonance process now become resonant. The last DR process called D', is a weak disorder-induced feature, which locates at $\sim$1620 cm^{-1} (center of Fig. 1.8 a). For instance, these defect/disorder induced features (D, D', and 2D or G' bands) had been used to characterize the crystal size of graphene based materials where the use of Raman scattering as a tool very accurate structural analysis of nano-graphite has been pointed [74].

Once the resonant Raman features in graphene has been explained, for comparison, in Fig. 1.9 one can visualize an archetypical Raman spectra of graphene and bulk graphite measured at 514.5 nm excitation wavelength [72]. The two most intense features are the G peak at 1580 cm^{-1} (E_{2g_2}), and a peak at $\sim$2700 cm^{-1} (G' or 2D). Finally, a feature around 3250 cm^1 depicts the triple resonance process previously described, and also called 2D' [72]. In the right side of Fig. 1.9, one can observe a significant change in the shape and intensity of the 2D peak of

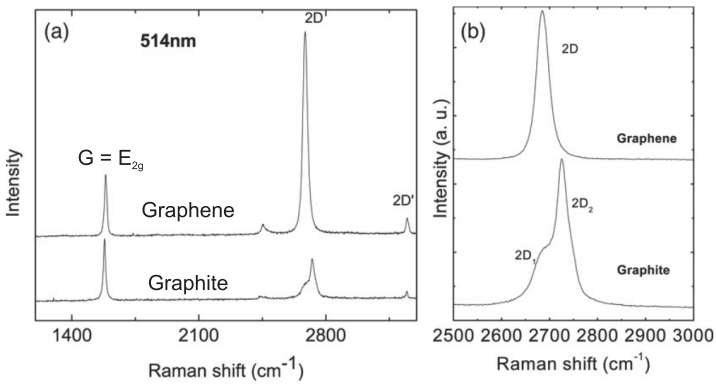

Figure 1.9: a) Comparison of the Raman spectra of graphene and graphite measured at 514.5 nm. b) Comparison of the 2D peaks in graphene and graphite. Figure adapted Ref. [72].

graphene compared to bulk graphite. The 2D peak in bulk graphite consists of more than one components, and leads information about the number of layers in the graphene or graphite sample, as a mono-layer graphene has a single, sharp 2D peak. The Raman spectrum in these graphene based materials could bring a lot of important information, and regarding intrinsic properties of graphene. For instance the 2D peak in GICs has never been studied before, and will be used to reveal some hidden information regarding mono- and multilayer graphene.

1.3. Graphite Intercalation Compounds

Graphite has a rich chemistry. Due to its amphoteric character [†] it can participate in reactions as either a reducing agent (electron donor) or an oxidizer (electron acceptor). This is a direct consequence of its electronic structure, which results in both an electron affinity and an ionization potential of 4.6 eV [35]. A large number of experiments [27, 77] for graphite focus on the insertion of additional chemical species between the basal planes, or intercalation has been also performed by looking for graphene production as a way for exfoliation of individual layers [78]. Graphite intercalation compounds (GIC) have long been the focus of intensive research, Shaffault is accredited with the first intercalation compound using potassium, dating back to 1841 [79]. However, the first systematic studies of these compounds began in 1930 with the introduction of X-ray diffraction (XRD) techniques for stage index (n) determination, further on Rüdorff and Schulze [80] in 1954 presented one of the first structures for KC_8 GICs becoming a field of intense activity due to their superconductivity [81] behavior since 1965.

GICs consist of a consecutive stacking of graphene layers with intercalated alkali-metals (K, Li, Cs, Rb), alkali-earth-metals (Cs), or rare-earth elements as well as p-type dopands like $FeCl_3$, AsF_5, H_2SO_4, HNO_3, etc. in between [27, 28, 77, 82–87] forming three-dimensional structures (see Fig. 1.10). Naturally, the properties of a given GIC depend on the specific chemical species that occupies the carbon interlayer space. Intercalant species are generally classified as donors or acceptors according to whether they give electrons to the graphite layers or extract electrons from the graphite layers. GICs appear to be the only layered compounds sufficiently ordered to exhibit "staging" in which the number of graphitic layers in between adjacent intercalants can be varied in a controlled fashion. The stage of a compound refers to the number of graphitic layers in between adjacent planes of intercalant.

In order that intercalation can be carried out, the intercalation mechanism must be understood. A dramatic aspect of intercalation mechanism was demonstrated by Gilbert Hooley in 1977 [88]. By alternately encapsulating the end basal planes or the edges of a graphite specimen before exposing it to bromine vapor, he found that the bromine enters from the edges as expected, but only if the end basal planes are also exposed. Another experiment showed that with no encapsulation the first intercalation occurred at the ends of a c-axis-oriented cylinder. Hooley reasoned that a surface reaction on the exposed c face triggered intercalation by distorting the carbon p_z charge density in the gap just below the surface, and that such a charge distortion was

[†] An amphoteric specie is a molecule or ion that can react as an acid as well as a base [76].

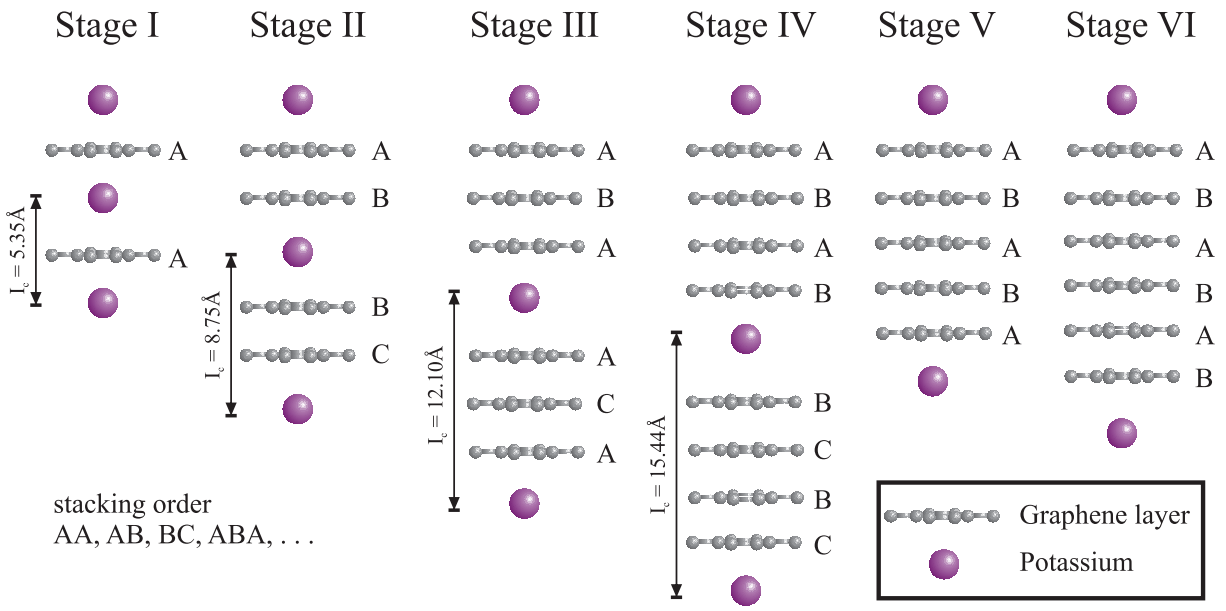

Figure 1.10.: Schematic diagram illustrating the staging phenomenon in graphite-potassium interaction compounds for stages I to VI. The potassium layers are indicated as purple balls, and the graphene layers by gray honeycomb networks.

necessary to permit intercalation to occur. In one model, a chemisorption process on the c faces triggers the first intercalation; this then distorts the next space, and the process bootstrapped until a uniform compound is achieved. In Hooley's works, the intercalation threshold is also described as function of the intercalant species, temperature, characteristics of the host crystal (Natural graphite, highly oriented pirolytic graphite "HOPG", bulk graphite, etc.), and intercalant vapor pressure, which must exceed the threshold pressure p_t. For example, regarding the sample size, p_t is lower for smaller sample thicknesses, so that thin samples intercalate more readily than thick samples. With respect to sample perfection, p_t is lowest for single crystal flakes, higher for HOPG host materials and yet higher for carbon fibers [27, 88]. These previous factors must be taken in consideration when synthesizing GICs, as it is crucial for a proper stage and intercalant concentration determination. Another important piece of study in GICs has been the fact of charge transfer. This is a subject of intensive study even nowadays, because this process controls the bonding between intercalant and graphene layers and also plays a major role in determining the electronic properties of the final compound [89].

Turning into the possible applications of graphite intercalation compounds, Inagaki [90] has pointed that GICs highlight from other materials due to their high electrical conductivity. As Electrodes for primary and secondary batteries, where their characteristics are high electrical conductivity and easy diffusion of electrochemically active species between the graphite layers. Large amounts of hydrogen can be stored in the functional space in alkali metal-GICs. Exfoliated graphite prepared by rapid heating of GICs leads to bulk production of graphene sheets which may be promising for industrial applications. However, in order to achieve these applications,

first of all, the intercalation process, mechanism and properties must be entirely understood, and further on, the different problems from the engineering point of view, issues such as host graphite, synthesis, stability, etc. must be solved like:

i One characteristic of carbon and graphitic materials is that they have various structures and textures. Thus a more detailed and systematic understanding of the effects of host materials on the structure and functions of GICs is needed to obtain high functionality and attain stability of GICs to be manipulable in air.

ii Further development of host materials for GICs. E.g. Graphite films prepared from different organic polymers are promising as hosts for GICs. Vapor-grown and mesophase-pitch-based carbon fibers (particularly interesting due to their wide cross section textures), and kish graphite, recovered from cast iron processing.

iii Development of new intercalation techniques which provides an insight for easier and more controllable intercalation processes, which could be extended into bulk productions.

iv Most GICs are not stable in air, water, or different organic media, and so techniques to stabilize the GICs have to be developed.

The previous open a wide range of research opportunities in this field. For instance, it has been proven that the inter-layer spacing in GICs can be increased due to intercalation from 0.34 nm (3.4 $\AA$) in pristine graphite to more than 1 nm in some GICs, which further exaggerates the anisotropy of many properties in this material [27, 91]. Thus, the possibility to increase the interlayer spacing in graphite (due to intercalation), also present a significant reduction in the van der Waals forces between adjacent sheets, which leads into the route to study single layers of graphene from a from a top-button approach [91–93] as will be see along this thesis.

1.3.1. Structural and Electronic Properties of GICs

GICs are classified in stages *I*, *II*, *III*, ..., *n* where stage *n* means that one intercalant layer follows after *n* (AA, ABA, ABC, etc. stacked) graphene layers depending on the stage (Fig. 1.10). The content of intercalant in each stage is determined from the stoichiometric formula XC_{12_n} with the exception of the stage I compounds whose chemical formula XC_8, where X is the type of intercalant. Thus, we have KC_8 as stage I, KC_{24} as stage II, KC_{36} as stage III, etc., and so on in potassium GICs.

Since many properties measurements are strongly dependent on the stage index, it is important to characterize samples to be used for property measurements with regard to stage index and stage fidelity. This type of characterization of graphite intercalation compounds is provided by X-ray diffraction using (00*l*) reflections. Sample characterization for stage index *n* and repeat distance between intercalant and graphene layers (I_c) had been carried out for large numbers of compounds and the results are given in various review articles [94–96] from where accurate staging determinations were performed by studying the (00*l*) diffractograms. From these diffrac-

tograms, the diffraction angles θ_l corresponding to the various $(00l)$ reflections are determined, and using Bragg's law:

$$l\lambda = 2I_c \sin\theta_l \tag{1.13}$$

I_c, the repeat distance (see Fig. 1.11), can be accurately evaluated. Since the graphite interlayer separation is essentially unaffected by intercalation, the stage index n can be found from the relation:

$$I_c = nc_0 + d_i = (n-1)c_0 + d_s \tag{1.14}$$

where c_0 is the distance between adjacent graphite layers ($c_0 = 3.35$ $\AA$) and $d_s = c_0 + d_i$ is the distance separating two graphite layers between which an intercalate layer is sandwiched. Analysis of $(00l)$ diffractograms show that for a given intercalant, d_s and c_0 are essentially independent of stage as illustrated in Table 1.2. The validity of Eq. 1.14 provides strong evidence that the n graphite layers remain essentially unperturbed by the intercalation process.

Table 1.2.: Repeated distance I_c for graphite-potassium intercalation compounds from Ref. [82]

I_c (experimental) $\AA$	Stage ($n=$)	I	II	III	IV
Rüdorff and Schulze [80]		5.41	8.77	12.12	15.49
Nixon and Parry [97]		5.35	8.72	12.10	15.45
Underhill (private communication)		5.32	8.74	12.07	15.44
Calculated $(5.41 + 3.35(n-1)\AA)$		5.41	8.76	12.11	15.46

In order to full characterize and understand the structural properties in GICs a combination of Raman spectroscopy and XRD, [98, 99] was used to assign and analyze the vibrionic structure for *stage I* to *stage VI* in Alkali GICs (see Fig. 1.11). For instance, Solin and Nemanich had presented the diffraction patterns for the $(00l)$ reciprocal lattice lines of potassium GICs for *stage I* to *VI* (see Fig. 1.11 left panel). Also, he reported a characteristic Raman spectra from each of those stages (Fig. 1.11 middle and lower right panels) revealing a linear in-plane lattice expansion [97] as a function of inverse stage for *stage III* to *VI*, and a clear Fano line-shape in *stage I* GICs independent of the intercalant. These results from Solin and Nemanich were crucial in the study of GICs, as they served to distinguish between "outer" graphene layers that are adjacent to an intercalant layer which are usually heavily charged and referred as bounding layer in the literature, and the "inner" layers that carry very little charge which are referred as interior layers in the literature. To highlight the importance of the charge transfer we will refer to them in the following as charged (c) and uncharged (uc) layers.

The structure and arrangement of atoms in GICs is governed by the *Nearest Layer* (NL) model from Nemanich and Solin [60, 100], while the kinetics of the transformation between stages respond to the Dumas-Hérold model where there are no completely unfilled layers in staged compounds but rather "pinched off" voids within partially filled layers [101]. Basically, when pristine

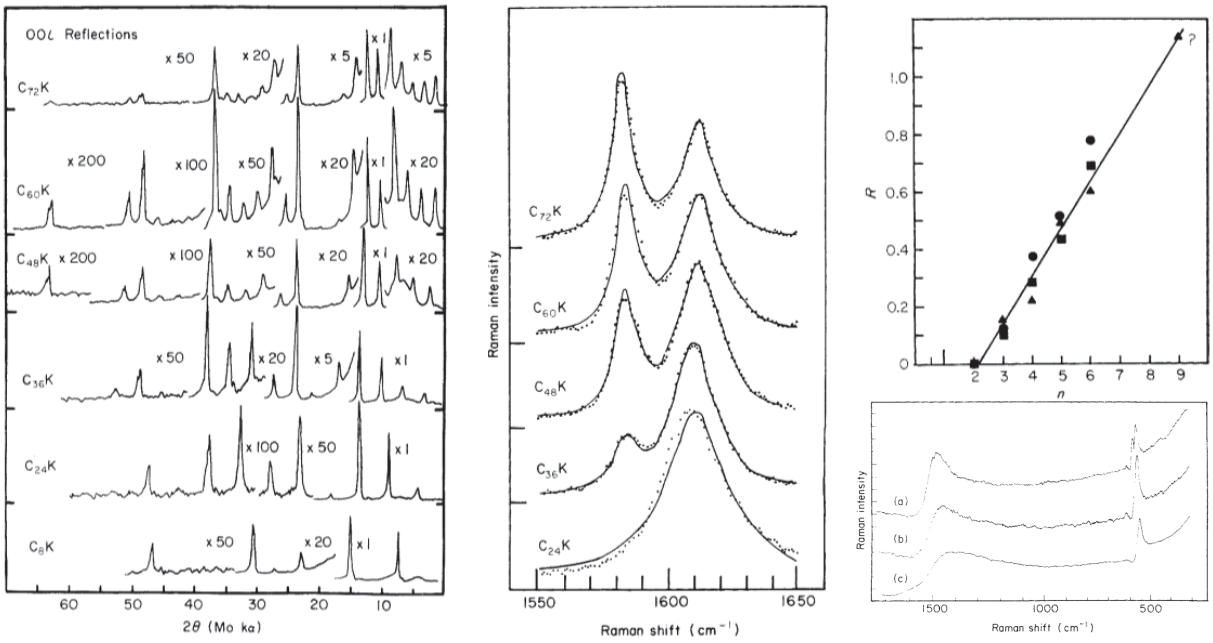

Figure 1.11.: Figure adapted from Ref. [99] results. Left – diffraction patterns from K-GICs ranging from *stage I* to *VI*. Middle – Typical Raman spectrum for K doped graphite ($2 \leq n \geq 6$). Right top – intensity ratio (**R**=I_c/I_{uc}) for $n \geq 2$ K, Rb, and Cs samples. Right lower – Raman spectra of the *stage I* (a) C_8Cs, (b) C_8Rb; and (c) C_8K, archetypical Fano lineshape.

graphite is intercalated, the nearest layer environment of carbon layers in the intercalated compound will depend on the stage of intercalation but is restricted to one of the three configurations observed in Fig. 1.10. The first configuration, show the possibility to have single carbon layers surrounded by intercalant layers. In the second configuration, there are two carbon layers with intercalant boundary systems. Finally, the third system presents the possibility to have a mixture of two carbon layers surrounded by intercalant plus a single carbon layer in between them. An extension of this model can be observed in Fig. 1.10 where the number of single carbon layers not surrounded by intercalant tend to increase as increasing the stage n.

This *Nearest Layer* model was invoked in order to explain the splitting of the G line (see Fig. 1.11 middle) for Alkali GICs when $n \geq III$. The relative intensity ratio **R** of the NL model plotted as a function of stage in Fig. 1.11, proofs the validity of the NL model which if the total charge transferred to the carbon layers is independent of stage, the linear dependence of R with stage implies that the transferred charge remains partially localized on the K boundary layers. We have proven this previous fact, and the results will be shown in section 4.4. Therefore, accordingly to the NL model, the lower-frequency G-line at about 1580 cm^{-1} in GICs corresponds in position to the G-line of neutral graphite and was therefore ascribed to the uc layers (supported by the fact that it is absent in *stage I* and *stage II* GICs). The higher-frequency line at about 1610 cm^{-1}, which is present for all stages, was consequently ascribed to the c layers, even though the exact mechanism of the stiffening remained unclear at the time. The stiffening has by now been understood as the effect of non-adiabaticity onto the vibrations of charged graphene

layers [102] and *ab-initio* calculations of *stage I* GICs have indeed confirmed the strong blue-shift of the G-line [103]. The NL model has been successful in identifying the different stages through the relative intensities of the G-lines of uc and c layers. However, the model alone is not able to explain the subtle frequency shifts of the G-line for the different stages and has not yet been used to investigate the dependence of the 2D line on staging.

One of the major effects of intercalation in graphite is the change of the inter-planar distance, which for instance is $c = 3.35\mathring{A}$ in pristine graphite. Small variations in the inter-planar spacing are expected for graphite layers adjacent to the intercalate layer (the graphite bounding layers) because of the different charge distributions at this interface and the introduction of the intercalant it self. In Table 1.2 the interlayer spacing (I_c) at stages I to VI are presented. The in-plane ordering in the graphitic planes is the same as in pristine graphite, with approximately the same in-plane lattice constant $a = 2.46\mathring{A}$ with a nearest-neighbor carbon-carbon distance of 1.42 $\mathring{A}$. However, a small in-plane expansion due to intercalation has been found for potassium graphite intercalation compounds by Nixon and Parry [97], with an approximate linear dependence of the nearest-neighbor C-C distance on reciprocal stage ($1/n$) given by:

$$d_{C-C} = (1.4203 + 0.0113/n)\ \mathring{A} \tag{1.15}$$

It is important to mention the fact that this linear relation is just valid when $n \geq 3$ and not for highly intercalated potassium compounds as it will be further explained along this thesis.

1.3.2. Electronic band structure in GICs

Turning into the electronic properties of GICs, the physical basis to study them arises from the strong *intra-layer* bonding between both graphitic and intercalate layers, and the relatively weak *interlayer* bonding between graphite-intercalate and graphite-graphite layers in the intercalation compounds. The electronic structure of graphite has been described in the section 1.2 starting from a bi-dimensional approximation (Graphene) and turning into a more complex 3D-graphite by using the SWMcC model. From a first approach, McClure proposed a model for graphite intercalation compounds based on rigid SWMcC bands for the graphite π-bands to be applied in bromine GICs [27]. According to this model, the Fermi level is allowed to rise for donors to accommodate the additional electron carriers, while for acceptor compounds, the Fermi level is lowered to accommodate the additional holes. Further use of this model was performed by Dresselhaus *et al.* [27] in which a basic assumption of the model is pointed: "the intercalate layer is effectively screened by a single graphite bounding layer". Thus, for the graphene interior layers in intercalation compounds where the stage index is $\geq$4, the electronic structure should be basically graphitic, and therefore it could be described by the SWMcC model with a minor modification of the the seven parameters (γ_0,...,γ_5,Δ) identified from the overlap and transfer integrals within the framework of the tight binding approximation. In the practice they are regularly evaluated experimentally accordingly to magneto-reflection, Fermi-surface, Raman spectroscopy, and optical reflectivity studies performed in graphite intercalation compounds presented in Ref. [27]. However, this model is not applicable to high intercalation stages as KC_8, KC_{24}, and KC_{36} nor the linear dependence of the nearest-neighbor C-C distance.

Because of the superlattice structure in the c-direction for well-staged materials and the additional in-plane superlattice in the intercalate layers, zone-folding techniques are used to relate both the electron and phonon dispersion relations of the intercalation compounds to those of the graphite host. Zone folding is applied both to phenomenological and first principles calculations. The zone-folding technique is commonly used for metals where the free-electron dispersion relation belongs to $E(k) = \hbar^2 k^2/2m$ is folded into a Brillouin zone appropriate to the crystal symmetry of the metal. The effect of a periodic potential is then treated in perturbation theory in the context of the zone-folded representation or reduced zone scheme. In the case of intercalation compounds, the high symmetry of pristine graphite is used as an approximate symmetry for intercalated graphite, and the disturbance to the graphite periodicity by the intercalant is treated as a perturbation.

Several first principles band calculations have been carried out for graphite intercalation compounds, but all have so far focused on stage I compounds due to the complexity about the number of atoms contained in the supercell system for higher stage compounds. For the simplest intercalation compound, *stage I* LiC_6, there are six carbon atoms and one Li atom per unit cell, assuming $\alpha A \alpha A \alpha$ interlayer graphite (A) and intercalate (α) stacking order. Thus LiC_6 has 39 occupied orbitals out of a total of 70 orbitals, considering all $1s^2 2s^2 2p^6$ levels for both the C and Li atoms. The unit cell for a *stage II* LiC_{24} with the same in-plane superlattice, and assuming either AB or ABC interlayer stacking order, it will contain 36 carbon atoms and three lithium atoms, which for the same $1s^2 2s^2 2p^6$ levels give 390 orbitals, 225 of which are occupied. Because of the large number of orbitals that are involved in the higher stage compounds the analysis for higher stages become more complex and expensive (in therms of computational requirements), and therefore band structure calculations have been mostly performed for *stage I* compounds with small unit cells.

A phenomenological model which takes into account both the SWMcC model and the first principles band calculations for *stage I* alkali compounds has been presented by Dresselhaus and Leung in 1980 [27] describing a procedure to determine the band structure in GICs under a superlattice system, as described in the following:

The phenomenological model which gives rise to the energy $E(k)$ throughout the Brillouin zone, makes use of the three-dimensional Fourier expansion of the graphite π-bands to account for the optical properties of pristine graphite. In this model the superlattice periodicity appropriate to the intercalation compound is added to the basic graphite symmetry through suitable zone folding of the Brillouin zone for pristine graphite. The in-plane intercalate ordering gives rise to zone folding of the in-plane wave vectors, which for instance is sensitive to the intercalate species (K, Li, Ca, Cs, $FeCl_3$, etc.). The staging phenomenon introduces a c-axis superlattice structure which is incorporated into the calculation by c-axis zone folding, as the this interlayer-spacing (I_c) change as function of the intercalant and stage (see Fig. 1.10). The effect of the intercalate layer is treated by substitution of an intercalate layer Hamiltonian for one appropriate to a graphite layer. The interaction between graphite bounding layers and the intercalate layer is treated as a perturbation. This perturbation is dependent on band parameters that are related to the overlap between the graphite π-band p_z orbitals and orbitals on the intercalate layer. These band parameters can be evaluated by comparison with either first principles calculations

or experimental Fermi surface, optical and magneto-optical data to bring experimental values to the γ parameters. Finally, the dispersion relations in GICs can be obtained by this model for a p(2x2)R^o super structure. For example, the calculated phonon dispersion for stages n=1,2,3 are shown in Fig. 1.12 with a consistent parameters for graphite, and no additional intercalant parameters. In this form, the bands are broadly applicable to all compounds with the indicated in-plane structure, and serve a tool for first stage approximation studies in GICs band structure calculations.

The importance in understanding the band structure belongs to the superconductivity behavior presented in some *stage I* GICs where charge carriers are transferred from the γ to the π* band. The resulting band of hole-like γ states couples strongly to the host lattice providing a natural environment to realize a high-temperature phonon-mediated superconductivity compound. From the later, one can then infer that a complete band structure calculation could bring information no only about the coupling between the intercalant and graphene states, but for stages $\geq$3, it could bring information about the single graphene layers allocated in between carbon ones, and thus a better understanding of their inherent electronic properties and superconducting origin.

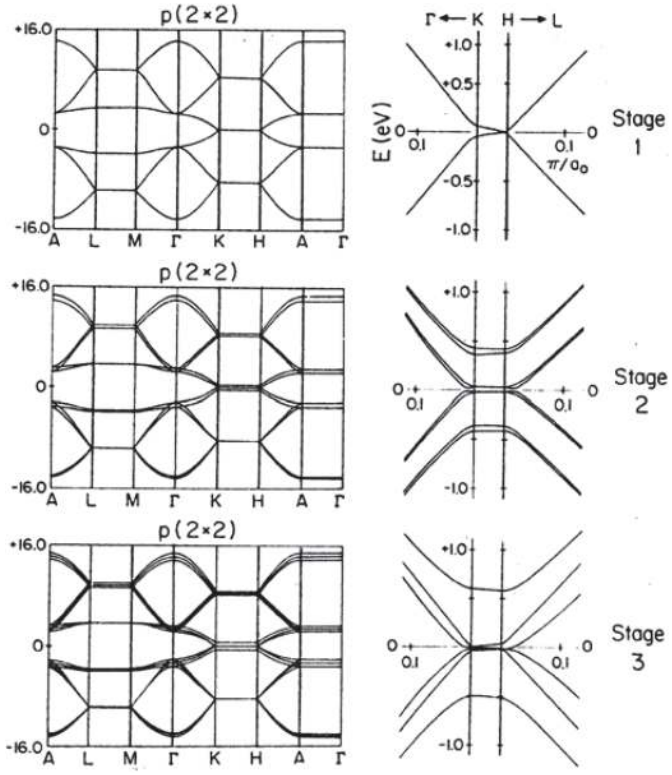

Figure 1.12: Electronic energy levels derived by zone folding of the SWMcC dispersion relations for a p(2x2) superlattice from stages n=1, 2, and 3. [82].

1.3.3. Superconductivity in GICs

Superconductivity is a quantum phenomenon which occurs at low temperatures in which the formation of electron pairs called "Cooper pairs" leads to the Meissner effect to occur with the expulsion of a magnetic flux of a type I superconductor and the observation of an ideal diamagnetic susceptibility (equal to $\kappa_d = -1/4\,\pi$ in emu CGS per volume unit) [33]. It was first studied by Henning and Meyer [104] in graphite intercalation compounds without complete success. Further studies were able to identify the superconducting transitions in the first stage compounds with the intercalants K, Rb and Cs [81, 105]. The first superconducting graphite intercalation compound to be reported was *stage I* KC_8 [27, 81, 106], which has a transition temperature of 0.15 K. Interestingly, whereas the metastable high-pressure phase LiC_2 has a superconducting transition (T_{sc}) at 1.9 K [107], the compounds LiC_6 (*stage I*) and LiC_3 are not found [108] to superconduct down to the lowest measured temperatures.

In 1991, the discovery of fullerene intercalation compounds, so-called fullerides, added a new family of organic superconductors of type A_3C_{60} (A=alkali-metal) [109–111]. Compared to classical superconductors, and in contrast to GIC the T_c observed in fullerides is high ranging from 18 K for K_3C_{60}, 28 K for Rb_3C_{60}, up to 39 K for Cs_3C_{60} [110–112]. Contrary to GIC, where the highest intercalation level represents the superconducting phase, for fullerides the superconducting phase is a line phase at half filling. Other stable fullerides A_1C_{60}, A_4C_{60} and A_6C_{60} are either normal metals, Mott-Hubbard insulators or charge transfer insulators [113]. Similar to GIC the superconducting coupling mechanism was described within the framework of BCS theory involving an electron phonon coupling to the intra-molecular modes of C_{60} [114]. Experimentally, most important for the coupling are the two low energy intra-molecular modes with H_g symmetry [115, 116], although theoretically the high frequency phonons have been predicted to play a significant role [117, 118].

The discovery of superconductivity in CaC_6 with a high T_c=*11.5 K* [119] in 2007, reloaded the interest in highly GICs and its properties. For instance, Kim et al. attribute superconductivity in CaC_6 to the high-energy C modes [120]. Hinks *et al.* [121] report that the low-energy modes of the intercalant were responsible for superconductivity inferred from specific heat analysis, while first principle calculations predicts equal coupling to both groups of phonons [122, 123]. Even more recent photoemission studies of the electronic structure in LiC_6, and and KC_8 [124, 125], a non-superconducting and a superconducting graphite intercalation compound respectively, have been performed in order to give an explanation to the superconducting behavior in GICs.

The origin of superconductivity in graphite intercalated compounds is controversial. Many theoretical groups have intended to explain this phenomena in GICs. Due to their layered nature and to the presence of an intercalant band at the Fermi level (E_F), Csányi et al. [126] have suggested a non-conventional exciton pairing mechanism [127]. On the other hand Mazin [128] has proposed an electronphonon mechanism mainly sustained by Ca vibrations. Calandra and Mauri have suggested that the pairing is mediated by the electron-phonon interaction and due to both Ca and C vibrations [122].

For instance, the strongest frequency mode in *stage I* GICs is a Fano mode of the G line at 1510 cm^{-1} in KC_8 and CaC_6, not like in LiC_6 (see Fig. 1.13 a) [57, 99, 129], which highlights the

importance of this mode to the superconductivity coupling mechanism within the BCS theory, and confirms the importance of this E_{2g_2} mode to non-adiabatic effects. By using this mode, we obtain a very good agreement to the theoretical predicted line width $\gamma^{EPC} = \Gamma_{ph}$ especially for CaC_6. However, the contribution of this phonon to the electron-phonon coupling constant (γ_{ph}) not enough to explain the high T_c in these graphite intercalated compounds [57, 129], in contrast it has been attributed to the in-plane TO phonon from the K point [62].

Since then, the identification of these first stage GIC has been done using different characterization techniques like: XRD [99], Raman spectroscopy [130], and more recently Angle Resolved Photoemission Spectroscopy (ARPES)[124]. ARPES studies on CaC6 [131], LiC_6 and KC_8 [124, 125] where the experimental Dirac cone expected at the **K** point in graphene is shown (Fig. 1.14) by using KC_8 ARPES analyses. Here, the two-dimensional band structure close to the Dirac point shows to be linear and two bands meet each other in one point. From this kind of experiments, values for the electron phonon coupling (EPC) had been reported on a graphene derived Fermi surface to graphene phonons strong enough to explain a T_c in the range of tens of Kelvin, indicating that graphene sheets provide crucial ingredients for superconductivity in GICs. These arguments put in evidence that the use of GICs (KC_8 in this case) far from the Fermi level but close to the Dirac point allows the observation of the intrinsic dispersion and electronic bands as if studying for doped or charged graphene. The origin and study of this doped graphene is still heavily debated, and the necessity of combining experimental analyses and simulations lies in the understanding of properties like heat, electrical transport, superconductivity and optics in graphene and graphite, which are governed by the interaction of electrons within the lattice vibrations. Even if the structure of the intercalation stages are well understood from XRD, and being studied by ARPES too, the intrinsic Raman response of GIC is still elusive as it is complicated by the fact of laser induced de-intercalation from a local heating of the sample with different laser power densities [60].

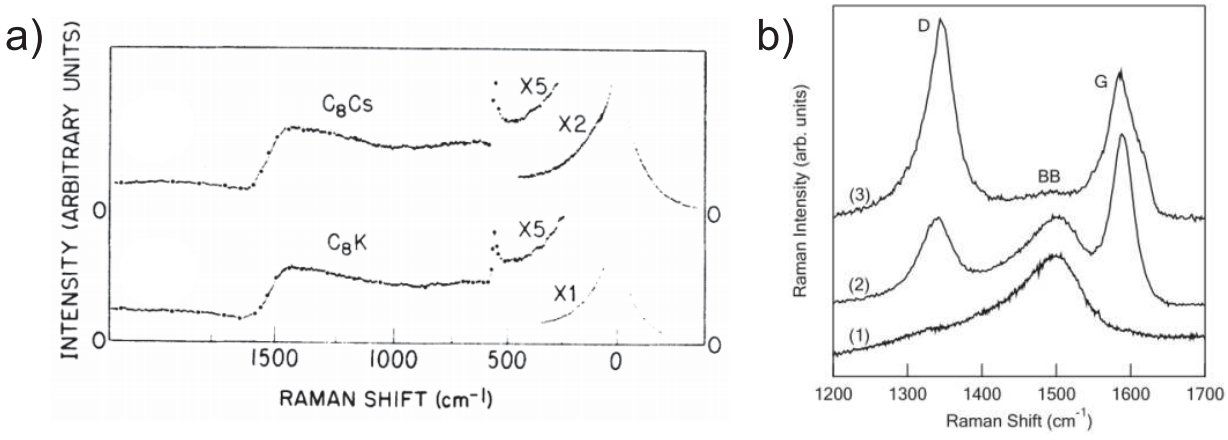

Figure 1.13.: a) KC_8 and CsC_8 characteristic Fano lineshape Raman spectrum from [60]. Two main components are depicted the main G-line component around 1510 cm^{-1}, and the c_z-mode at $\sim$550 cm^{-1} due to the inter-planar lattice vibrations. b) CaC6 [119] Raman spectrum, from where the button spectra refers to the not air exposed sample, while the others are air exposed after several hours. Disorder and de-intercalated peaks reveal the decomposition of the sample.

In addition, other factors such as intrinsic disorder of the crystal also strongly affect the Raman response in GIC. Previous experimental and theoretical results on the Raman response of KC_8 reported in the literature are not conclusive with respect to the **G-line** shape and position. In different studies a wide range of different **G-line** positions between $\sim$1400 cm^{-1} and $\sim$1600 cm^{-1} are reported: i.e. at $\sim$1500 cm^{-1} [27], between 1400 cm^{-1} and 1550 cm^{-1} [99], 1534 cm^{-1} [103], 1547 cm^{-1} [60], 1420 cm^{-1} and 1582 cm^{-1} [130]. The inconsistency of these reports can be related to an incomplete intercalation which can be denoted on their line position and line width as has been also shown in recent experiments on potassium doped graphene [132]. On the other hand defect modulation of the GIC can be another reason for different **G-line** responses. This has been for instance reported by Dean et al. [133] using a Micro-Raman study of different positions in a CaC_6 crystal, and by Hlinka [119] as seen in Fig. 1.13 b) where the Raman spectrum from a CaC_6 sample exposed to air was recorded. They noticed the appearance of a **D** mode in some zones of the sample, which is absent in the most reflecting and purest part of the sample. The knowledge of the intrinsic Raman response becomes especially important since superconductivity is based on electron phonon coupling (EPC) and involves the graphitic **G-line** phonons [133]. The renormalized position and line-width of these line directly determines the EPC constant in the superconducting GIC [103].

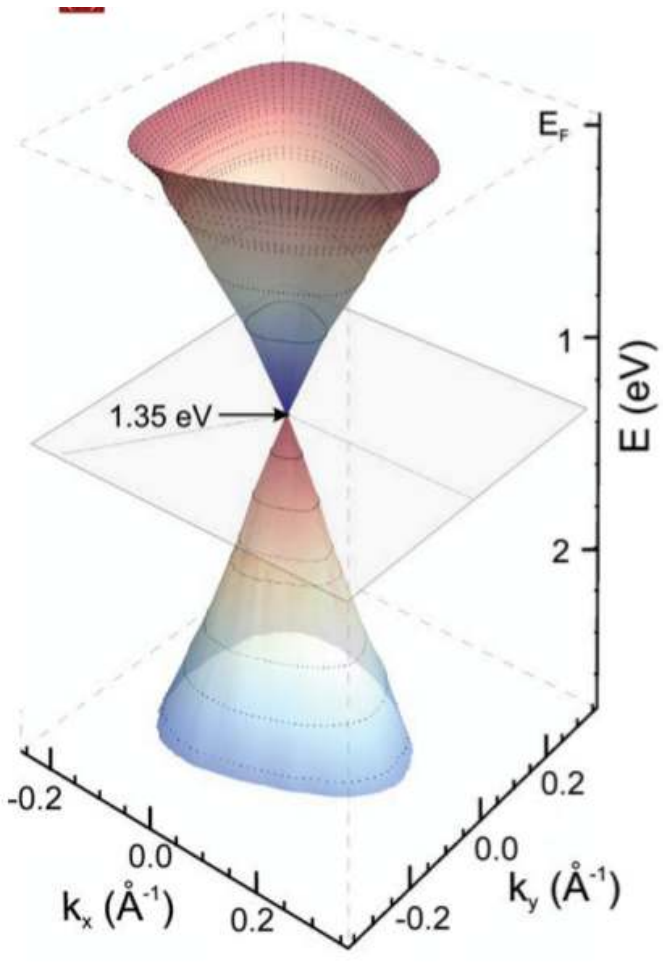

Figure 1.14: Experimental Dirac cone from the observed photoemission intensity maxima in KC_8 is depicted [124].

Raman and IR spectroscopy had became then an important tool to determine the exact contribution of each phonon, and it opened a route for revealing the coupling mechanism in superconducting fullerides and GICs. Hence, it serves as a key tool to analyze the electron phonon coupling constant (λ) from a renormalization of the optical response of the intra-molecular C_{60} modes and of the graphitic G-line response. Recent Raman studies on the G-line response of different *stage-1* GIC reported the assignment of the electron phonon coupling (EPC) induced line width γ^{EPC} to the 1510 cm^{-1} mode [103, 119, 133, 134], which has been explained by the inclusion of non adiabatic phonon calculations [103, 133]. However, the intrinsic G-line response in heavily doped graphite compounds are still elusive because of the influence of defects and laser induced deintercalation, as recently reported using a micro Raman analysis for CaC_6 [133] and for KC_8 single crystals [135].

1.4. Large scale pristine and functionalized graphene

1.4.1. Chemical Vapor Deposition of graphene

One approach to produce graphene, and study its novel properties, has been Chemical Vapor Deposition (CVD). CVD is a chemical process designed to produce high purity, quality, and performance solid materials. This technique is usually used to produce thin films in the semiconductor industry. In a general CVD process, a substrate also called wafer is exposed to one or more vapor precursors, which can react or decompose over the substrate surface in order to produce the desired material. By using metal-assisted thermal CVD, the synthesis of large areas of graphene has been achieved, being an exciting prospect for number of reasons: (1) it allows large area graphene synthesis on a wafer scale with high uniformity and low defects, (2) it allows exploration of a wide variety of transition metals as catalysts and in elucidating the role of various process parameters, (3) it allows the integration with high volume CMOS-based technologies, and (4) it may enable an understanding the synthesis mechanism of graphene using metal catalysts [136]. Different transition metals including nickel, copper, ruthenium, and cobalt have been previously reported in the fabrication of graphene by this CVD method [137–144]. The grown of graphene by CVD consist in the use of carbonaceous gaseous species, which reacted at high temperatures (900-1100 °C) in the presence of metal thin films/foils, which serve as a template in the decomposition of the carbon species and the nucleation of the graphene lattice. The graphene growth mechanism on a metal surfaces catalyst is most likely influenced by factors as: the carbon solubility limit in the metal, its crystal structure, lattice parameter, and thermodynamic parameters such as the temperature and pressure of the system. By far, different growth mechanisms have been attributed primarily to the carbon solubility in the metals such as Cu and Ni where the synthesis of graphene is limited to the surface of the catalyst, the growth temperature, and a precipitation of carbon from bulk to the surface of the metal upon cooling after the CVD synthesis [139–141]. It has been for instance demonstrated that the kinetics of graphene growth in a CVD process plays a critical role in the uniformity of large area graphene using a Cu catalyst. Although the thermodynamics of the synthesis system remains the same, whether the process is

performed at atmospheric pressure, low pressure (0.1-1 Torr), or under ultrahigh vacuum (UHV) conditions (10^{-4}-10^{-6} Torr), the kinetics of the growth phenomenon are different, leading to a variation in the uniformity of the graphene over large areas (wafer scale) [136] (see Fig. 1.15). These results showed in the literature of CVD graphene suggest further investigations to further control and understand the growth mechanism in graphene. Moreover, the possibility to change the precursors in the CVD process has brought the possibility to alter and improve the electronic properties of graphene as it will be shown in the next part.

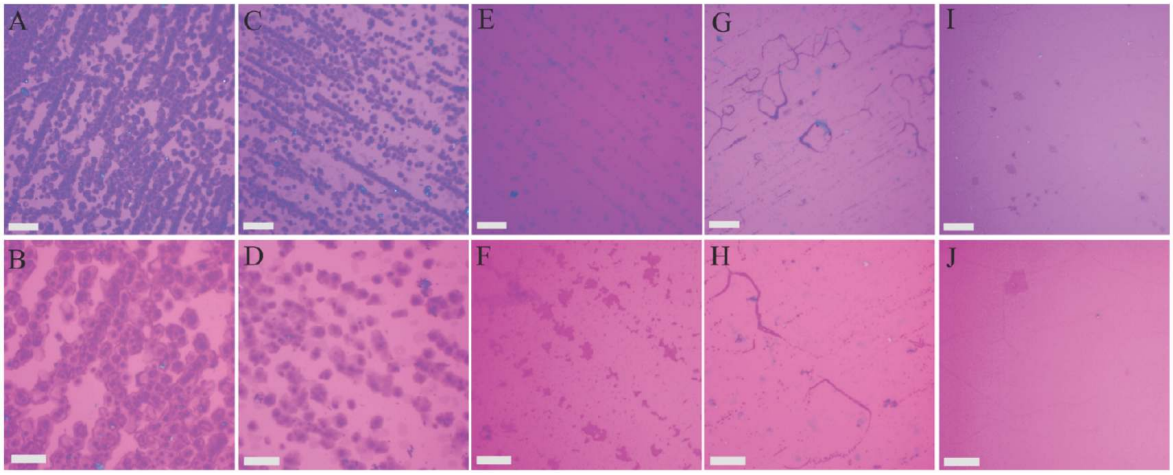

Figure 1.15.: Optical images of transferred graphene on 300 nm SiO_2 synthesized under atmospheric pressure CVD conditions using Cu as a catalyst at different methane gas compositions taken from Ref. [136]. The samples 1 to 5 are ordered from left to right. The concentration of methane in this experiment was decreased being sample six (S5) the one with the lowest content of methane. S1 (A, B), S2 (C,D), S3 (E, F), S4 (G, H), and S5 (I, J); scale bars (A, C, E, G, I, 20 μm; B, D, F, H, J, 10 μm).

The production of epitaxial graphene (EG) on diced (3 mm by 4 mm) commercial SiC wafers (11) is another outstanding technique followed by the CVD one in the route of large graphene production areas. The grown mechanism studied by Berger et al. [145] can be summarized in two main steps: (i) hydrogen etching to produce atomically flat surfaces in a SiC (11) crystal, and (ii) vacuum graphitization to produce an ultra thin epitaxial graphite layers. Moreover, this technique has been developed, and turned into a growth of graphene by thermal desorption of Si from SiC (sublimated epitaxial graphene: S-EG) [146] in order to improve the quality of the S-GE.

Graphene produced by sublimating Si from SiC heated to high temperatures (1200-2000 ^{o}C) is sensitive to the surface quality of the SiC substrates. Moreover, local scattering caused by charge buildup at the SiC substrate step edges can degrade electron transport properties and step edges give rise to the growth of additional one or two mono-layers that deteriorate the graphene thickness uniformity [146]. For instance, Strupinski2011 et al. have shown the possibility to apply

the CVD growth method of epitaxial graphene (CVD-EG) on SiC substrates using propane gas as the carbon precursor. The approach proposed by them offers numerous benefits in comparison to S-EG, including the application of well-developed commercial epi-systems for SiC epitaxy. The most critical step in this method, is the protection of the SiC substrate against Si sublimation at conditions of high temperature (T$\simeq$1600^{o}C) and low Ar pressure. While protecting against Si sublimation, C deposition can be performed with a mono-layer resolution (see Fig.1.16) by taking advantage of the high efficiency of kinetic processes at high T and low P [146]. The proposed method permits the growth rate lowered enough to enable the growth of mono-layers, which is extremely difficult to achieve in the case of S-EG. Additionally, multilayer graphene (MLG) can be grown on Si-face SiC(0001), which in comparison to a maximum S-EG thickness of two- and three- multi layers, which open opportunities for the study of graphene formed on the Si-face in a large area.

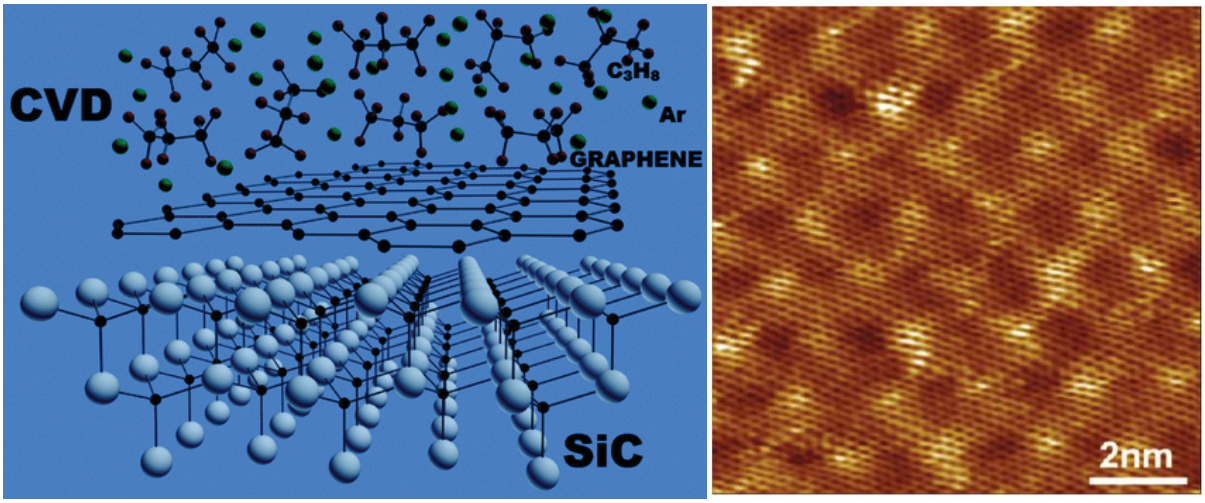

Figure 1.16.: (Left) Schematic representation of graphene growth layers by chemical vapor deposition (CVD) on insulating and conductive SiC substrates. (Right) Atomically resolved STM image of a CVD-EG layer grown on a 4H-SiC(0001) substrate, taken over an area of 10x10 nm^2. Figure adapted from Ref. [146]

1.4.2. Functionalized Graphene

Nowadays many groups have improved the CVD method for growing high quality large-area graphene [136, 147–150]. One of their current goals, as mentioned in the previous section, was not only the understanding of the electronic properties of graphene but also to control and modify them. A way to tailor the electronic properties of graphene is via dopant incorporation for n-type (electron) or p-type (hole) characteristics similar to the electron doping in graphite intercalation compounds. Usually, there are two ways to chemically dope graphene: (1) the adsorption of gas [151], organic molecules [152], or metals [153] to the graphene surface and (2) substitutional doping, which introduces hetero-atoms, such as nitrogen atoms and boron atoms, into the carbon

lattice of graphene. By using any of these two methods, one can modulate the electronic properties of graphene. However, substitutional doping of graphene with different atoms (e.g. B, N, S and Si) results in the disruption of the ideal sp^2 hybridization of the carbon structure in graphene inducing significant changes in the electronic properties and chemical reactivity [154–158].

One of the current research goals is focused on controlling the electronic properties of graphene via dopant incorporation for n-type (electron) or p-type (hole) characteristics. To this end, substitutional doping of nitrogen atoms into the graphene lattice has been achieved using CVD, chemical exfoliation, and other post-synthesis doping methods [151, 152, 155, 159–163]. As shown in Fig. 4.16, the rich chemistry between carbon and nitrogen can result in pyridinic, pirolytic, or graphitic configurations [151, 152, 155, 159–163]. Previously, such bonding environments were reported for doped carbon nanotubes and graphene, and the properties of N-doped graphene were analyzed using x-ray photoelectron spectroscopy (XPS), Raman spectroscopy, scanning tunneling microscopy, and transmission electron microscopy [151, 152, 155, 159–163].

In particular, N-doping is expected to introduce additional n-type carriers in carbon systems, which is crucial for applications in high-frequency semiconductor devices [155] and enhanced catalysis for energy conversion and storage [164–166]. In addition, N-doping could also enhance the bio-compatibility of carbon nanomaterials [167, 168] and therefore is favorable for bio-sensing applications [169] too. However, the correlation between the local bonding environment, doping ratio, and the change in fundamental properties of doped graphene is still lacking, reason why there has been a vast research in systems like nitrogen doped graphene (N-graphene).

Recent studies have already performed substitutional doping of nitrogen atoms into the graphene lattice by using the CVD method, chemical exfoliation, and other post-synthesis doping methods [151, 152, 159–162]. The N-graphene reveals different characteristics compared with pristine graphene. For instance, the spin density and charge distribution of carbon atoms can be governed by the neighbor nitrogen dopant [171, 172] which causes the activation region on the graphene surface. This kind of activated region participate directly the catalytic reaction, most likely in oxygen reduction reactions, or when trying to anchor metal nanoparticles to promote the catalytic reaction grown. Moreover, after doping graphene with nitrogen, the Fermi level used to shift above the Dirac point and the density of states near the Fermi level is suppressed, leading into an opening between the conduction and the valence band gap [173]. Recent experiments performed by Ruitao *et al.* [170] have demonstrated the feasibility to produce large-area of mono-layers nitrogen doped graphene (NG) sheets were synthesized on Cu foils using methane (CH_4) and ammonia (NH_3) as precursors in an atmospheric pressure CVD setup(see Fig. 1.17 a). The subsequent steps in the synthesis of NG and graphene is the de-attachment of the material from the metallic substrate. In this case it has been done by underneath the Cu foil in an aqueous $FeCl_3$/HCl solution and further transferred onto a SiO_2 or SiC_2 wafer as in Fig. 1.17 a). From a high-resolution transmission electron microscopy (HRTEM) study one can obtain a fast Fourier transform (FFT) which reveals the hexagonal feature of the single-layer NG lattice. In order to further study the structural and vibrational properties of NG, Raman spectroscopy studies have been performed where the contribution from the E_{2g} modes (so called G-line) are observed. In Fig. 1.17 b), a representative Raman spectra of N-doped and pristine graphene on SiO_2/Si substrates using 514 nm laser excitation are shown from Ref. [170]. Both kinds of samples were

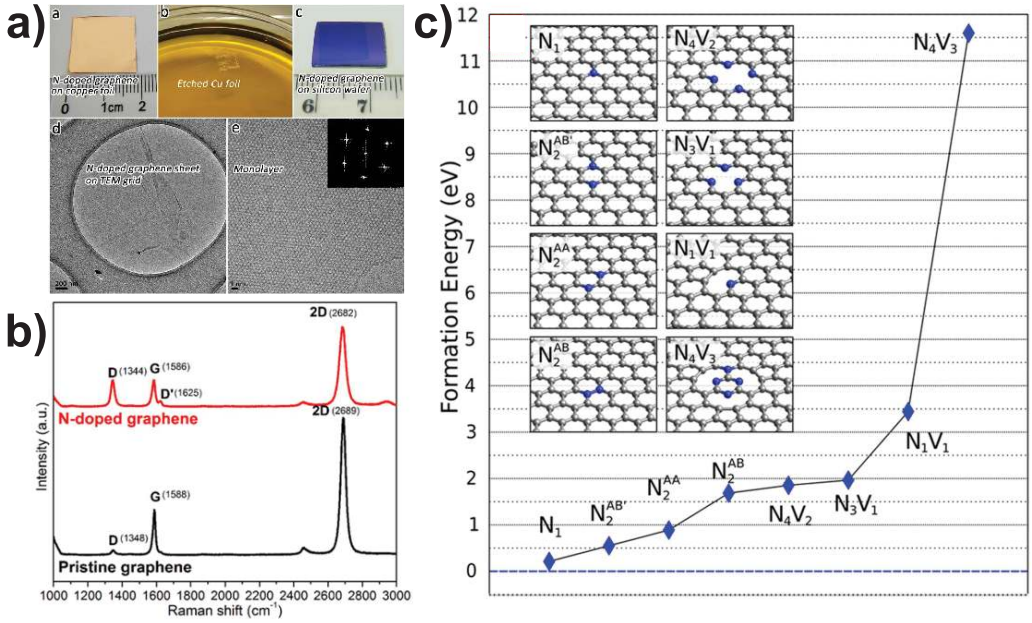

Figure 1.17.: N-graphene sample on Cu foil synthesized by CVD taken and adapted from Ref. [170] a). The PMMA-coated NG with Cu residues floating on $FeCl_3$/HCl aqueous solution used as Cu etchant. Finally, the NG sheet (1 cm x 1 cm) on SiO_2. A typical HRTEM images of as synthesized mono-layers NG with its corresponding fast Fourier transform (FFT) inset depicting the hexagonal pattern characteristic of the graphene framework. b) Raman spectra of N-doped and pristine graphene on SiO_2/Si substrate at 514 nm. c) Formation energies of different N-doping configurations in NG sheets (as illustrated in insets) computed using ab initio calculations.

synthesized under the same experimental conditions except for the introduction of NH_3 used for the N-doping. Compared to that of pristine graphene, the Raman spectrum of NG shows a downshift of the G-line (2 cm^{-1}) and 2D-line (7 cm^{-1}). Based on the empirical relationship between the Fermi energy and the Raman peak position [174], the down shifts suggest that the nitrogen dopant move the Fermi level of graphene up by $\sim$350 meV. This for instance has been confirmed by Usachov *et al.* [162].A doping level of 300 meV, and a charge-carrier concentration of $\sim 8x10^{12}$ electrons per cm^2, induced by 0.4 atom % of graphitic nitrogen, have been detected by angle-resolved photoemission spectroscopy. The *ab-initio* computed formation energies for different types of N-doped graphene (Fig. 1.17 c) confirm the stability of nitrogen atoms under different configurations in the graphene lattice. The different possible configurations in which nitrogen insets in graphene are summarized: (1) substitutional or graphitic N, (2) pyridine-like N, (3) single N pyridinic vacancy, (4) triple N pyridinic vacancy, (5) pyrrole-like, (6) interstitial N or ad-atom, (7) amine, and (8) nitrile [162]. Once the different kind of nitrogen doping configurations had been established, further structural studies are needed in order to clearly assign the vibrational response of nitrogen in the hexagonal structure of graphene.

1.5. Motivation and accomplishments

"I want to build a billion tiny factories, models of each other, which are manufacturing simultaneously... The principles of physics, as far as I can see, do not speak against the possibility of maneuvering things atom by atom. It is not an attempt to violate any laws; it is something, in principle, that can be done; but in practice, it has not been done because we are too big."

–Richard P. Feynman

Since my early years I always wanted to be part of important scientific experiments, and be part of great discoveries. Richard Feynman has been one of my main motors in this scientific route by introducing the idea of medical micro-machines. This idea was incorporated into Feynman's 1959 essay "There's Plenty of Room at the Bottom" under the following passage:

"I want to offer another prize—if I can figure out how to phrase it so that I don't get into a mess of arguments about definitions—of another $ 1,000 to the first guy who makes an operating electric motor—a rotating electric motor which can be controlled from the outside and, not counting the lead-in wires, is only 1/64 inch cube."

For me, as a young mechatronics Engineer in 2008, this idea was not only amazing but also the challenge I was looking for. However, the background of an Engineer is not enough to carry out this idea. Then I realized that a solid background in Materials Sciences, Physics, and Nanotechnology was essential for me to accomplish this goal. In my route for this specialization found Carbon Nanotubes, Fullerenes and Graphene, as tools that could be helpful in order to make possible the "rotating electric motor" in a 1/64 inch cube. However, one of the main thoughts of an Engineer is not only: How could I make it?, or How could I control it?, but also How could I bring energy to this system and make it work? This final question brought my attention to the so-called Graphite Intercalation Compounds, as a futuristic nano-battery. For all these applications, a profound understanding of the properties is indispensable. Thus, I decided to focus my attention in the understanding of this material, how can intercalation be controlled inside graphite and carbon nanotubes with a scope for further nano-applications. I was then pleased to carry out a PhD in which my knowledge and background in physics could reach my desired goals.

Graphite and Graphene are a well-established field being still an outstanding field of study due to their interesting structural and electronic properties. In graphite, however, the use of guest atoms and molecules to intercalate between graphite layers is known to considerably modify the electronic structure of graphite, leading to unique physical properties and technological applications such as superconductivity and rechargeable batteries. The out-scope of this intercalation technology comes with its thinnest limit of GICs as intercalated bilayer graphene, and the investigation of its electronic structure to promote graphene engineering.

Raman spectroscopy has been set as a key tool to identify the number of layers and to probe the physical and electronic properties in graphene based materials. In the same manner, the

double resonant Raman process (2D-line), which arises from the nonequivalent K points in the Brillouin zone (BZ) of graphene offers information related to the number of graphene layers, induced strain in the structure, charge transfer and phonon dispersion. The general mechanism for charge transfer in donor compounds is well known, though uncertainties remain regarding the magnitude of the charge transfer and the electronic and vibrational structure in GIC. GICs are so far the only layered compounds sufficiently ordered to exhibit "staging" in which the number of graphene layers can be varied in a controlled fashion, and for instance brings the possibility to study graphene under different conditions such as charge transfer, strain, and stacking. However, in the majority of the published articles there still some open questions which we found important to answer, i.e.:

In 1980, M. Dresselhaus, and G. Dresselhaus compiled all the information available regarding GICs in a review article, in which the structural, electronic, and magnetic properties of Graphite Intercalation Compounds were presented and an important statement of an "updating in the near future" due to its relevant interest for the scientific community in the disentanglement of the embedded graphic layers in GICs.

In this contribution we will focus on a novel detailed in-situ Micro-Raman study of different KC_8 single crystals paying special attention on different defect modulations and on ultra low laser powers to avoid de-intercalation, in order to unravel the intrinsic fingerprint of the **G-line** Raman response. In agreement with the previous reports, we observe a spread of the Raman response. However, a detailed line shape analysis revealed that all spectra can be simulated by four Fano lines with different relative intensities. Thereby, we find that the intrinsic KC_8 Raman response is at 1510 cm^{-1}, in agreement with previous reports on XC_6 [133].

A detailed study of the D- and G-lines in KC_8, CaC_6, and LiC_6 GIC will be shown in order to unravel their intrinsic phonon components from the superconducting GIC face and its relation to the electron phonon coupling constant responsible for superconductivity. From the analysis of the optical phonons observed, we assign their role in the superconductivity coupling mechanism in comparison with previous results of electron doped GIC. Also, we want to unravel the intrinsic de-intercalation process due to the changes in the graphitic G-line phonon modes between those two systems performing a detailed line-shape analysis. This analysis yields as a convenient reference system to assure a proper determination of the intrinsic *Stage-1* and *Stage-2* compounds, and will further allow the complete picture of superconducting and non-superconducting *Stage-1* faces.

Finally, in order to complete the story in GICs, we wanted to perform an extensive Raman spectroscopy study of potassium GICs, measuring both the G and the 2D lines for different laser energies and for the different intercalation stages up to *stage VI*. The measurements are accompanied by *ab-initio* calculations of the electronic structure, charge transfer, lattice expansion and vibrational properties of these GICs. We present a quantitative refinement of the nearest layer model which takes into account the exact charge transfer, the lattice expansion and the effect of AB-stacking of the inner (uc) layers. By comparing our results with the available experimental data on charged, strained, and multi-stacked graphene layers, we show how to disentangle the different (partially counteracting) effects onto the position of the Raman lines.

Chapter 2

SPECTROSCOPIC AND THEORETICAL TECHNIQUES

In this chapter, the light scattering principle, which is the basic concept to spectroscopic techniques will be introduced. Further more, the use of Raman spectroscopy, Photoemission spectroscopy, and DFT calculations will be explained in detail as the conceptual part of the experimental and theoretical techniques respectively to study, understand and prof the open questions about graphite intercalation compounds and graphene from a top-bottom approach.

Light scattering can be described as the light redirection from an incident electromagnetic (EM) wave ω_i which reaches an obstacle either solid, liquid or gas (see Fig. 2.1). As the EM wave interacts with the sample, its electron orbits are constantly perturbed at a constant frequency different from the incident wave. This induced perturbation which results in a periodic charge separation within the molecules so called induced dipole moment. The induced dipole moment results in a scattered light which is analyzed relative to the spectrum of the incident light. The majority of light scattered is emitted at a frequency (ω_f) resulting from the incident light. However, as explained below, additional light is scattered at different frequencies, a process referred to as inelastic scattering. Raman scattering is one such example of inelastic scattering and will be described in detail in the following.

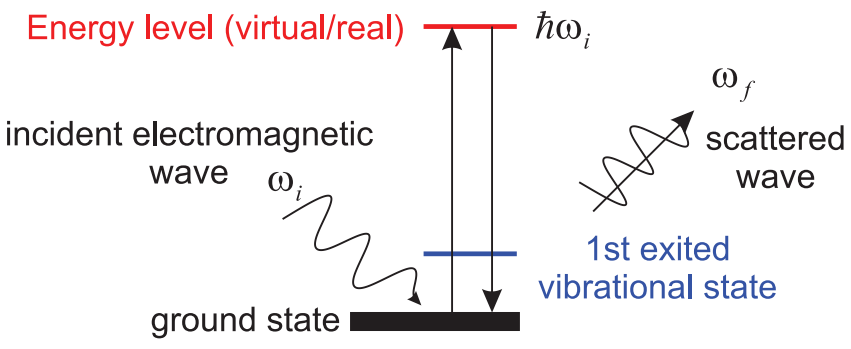

Figure 2.1: Scheme of light scattering by an induced wave length.

2.1. Raman Spectroscopy

A large variety of spectroscopic techniques are available nowadays for the analysis of materials and chemicals. Among these is Raman spectroscopy, named like this in honor to Sir C. V. Raman (Nobel Prize 1930). In this technique, the light is scattered inelastically as opposed to the more prominent elastic Rayleigh scattering [175]. This inelastic scattering causes a shift measured in terms of wavelength, and can be then used to extract information about the material by simply analyzing its resulting spectrum. There exist different scattering processes as depicted in Fig. 2.2, and each of them relates to a different transition observed along the scattering process as it will be explained in the following *:

- The Rayleigh scattering, has been considered as an elastic effect, in which the light scattered from the material does not gain or loose energy along the process staying at the same wavelength (λ). In this Rayleigh scattering process Fig. 2.2 a), a photon is induced into a molecule which exiting and electron into a "virtual" energy state extremely short lived ($\sim 10^{-14}$ seconds) and very close to the excitation line. After that, the molecule tends to get back into its ground state, and release a phonon with exactly the same initial energy and λ.
- Raman scattering, an inelastic process, is an effect in which the light emitted into a molecule loose or gain energy along the scattering process which decreases or increases the final resulting energy. In this scattering process there exist two possibilities: First, the molecule is exited from the ground state into a virtual state, and then goes back into a state with higher energy which results in a phonon scattered with a longer wavelength (see Fig. 2.2 b). On the other hand, if the molecule is already in a vibrational state with high energy than the ground state, after being exited, the resulting phonon will come out with a shorter wavelength as observed in Fig. 2.2 c).
- All these previous processes are considered as non-resonant because the excited electron from the molecule always goes into a virtual state where no eigenstates from the molecule are exited. A resonance Raman process occur when the intermediate state of the excited electron is an eigenstate of the system (see Fig. 2.2 d) leading into a strong enhancement in the resulting spectra, as the final photon energy matches the eigenenergies of the investigated system [176]. For instance this situation occurs in graphite and graphene, and other nanocarbon materials which highlights the importance of resonance Raman spectroscopy studies for this thesis.

The different forms of scattering processes mentioned before require the conservation of both energy and momentum from where the symmetry operations are based in the group theory from the molecule or crystal. In order to have a Raman active mode, it must exhibit a polarizability change known as spectroscopic selection rule (Eq. 2.1) where q is the normal coordinate and e the equilibrium position.

$$\left(\frac{\partial \alpha}{\partial q}\right)_e \neq 0 \tag{2.1}$$

*The description and origin of the different scattering processes is in part taken from Ref. [176, 177].

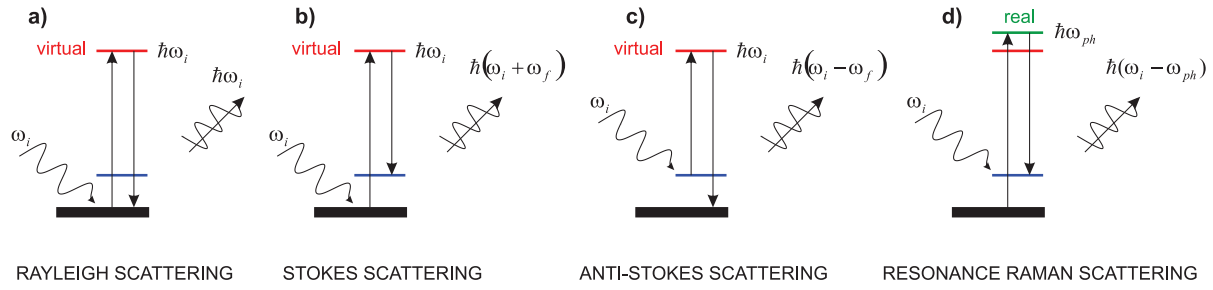

Figure 2.2.: Conceptual scheme of the light scattering processes: a) Rayleigh scattering, b) Stokes scattering c) Anti-stokes scattering, and d) Resonance Raman scattering.

It is important to mention, that this rule applies differently regarding infrared spectroscopy (IR), and Raman spectroscopy resonance processes. Considering IR, the transitions involved between the in-coming/out-going phonon cause a change in the dipole moment allowing different vibrational modes to be accessible. Therefore one could use both, IR and Raman resonance spectroscopy, when analyzing a molecule and make the two techniques complementary. However, when studying the center of symmetry in a molecule, one must be careful as both, Raman and IR modes are inactive, which is called rule of mutual exclusion. The intensity of a resulting band from the out-going phonon in a Raman spectrum is given by the general relationship: $I(\omega) \simeq |M(\omega)|^2 \cdot g(\omega)$ where $M(\omega)$ is the Raman transition matrix as function of the electron-phonon coupling and the phonon density of states $g(\omega)$ [59]. The origin of the different scattered frequencies can be explained in the next way as in Ref. [177]:

1. Lets consider the strength of the induced dipole moment (P_D) due to an applied field E(ω), and polarizability α given by:
$$P_D(\omega) = \alpha E(\omega) \tag{2.2}$$

2. The polarizability of a molecule depends to the atom-atom bond length (i.e. as shorter the bonding weaker the polarization). Therefore, α will depend directly to the molecule frequency oscillation (ω_i Hz), incident EM ($\omega = c/\lambda$), and the electric field may be expressed as:
$$E(\omega) = E_0 \cos(2\pi\omega t) \tag{2.3}$$

3. Therefore, by substituting Eq. 2.3 into Eq. 2.2 we obtain the time-dependent induced dipole moment:
$$P_D(\omega) = \alpha E_0 \cos(2\pi\omega t) \tag{2.4}$$

4. Now, we consider that the molecule is vibrating with a frequency Ω with a periodical change in the distance between the atoms, and a modulated polarization. Thus, the total dipole moment will have the form of:
$$\partial P_D(\omega) = E_0(\alpha_0 + \alpha_1 cos\Omega t) cos\omega t \tag{2.5}$$

   Using trigonometric sum rules, the above relation may finally be recast as:
$$P_D(\omega) = \alpha_0 E_0 \cos(\omega t) + (\alpha_1 E_0/2)[cos(\omega+\Omega)t + cos(\omega-\Omega)t] \tag{2.6}$$

This last equation 2.6 reveals that induced dipole moments are created at three distinct frequencies: ω, $\omega - \omega_{vib}$, and $\omega + \nu_{vib}$, which for instance have scattering radiations at these same three frequencies. The first scattered frequency corresponds to the Rayleigh elastic scattering. The next two frequencies are shifted to lower or higher frequencies ($\pm$) being therefore inelastic processes Raman active. The down-shifted frequency (longer wavelength) will be referred as Stokes scattering, while the up-shifted frequency (shorter wavelength) is the anti-Stokes scattering one. The above is based on single molecules in a gas, and hence not interacting with neighbors. In materials science the Raman (and IR) activity of more complicated molecules can be determined using their symmetry and group theory as it is the case of Graphene and Graphite.

In practice, Raman spectroscopy is generally is a technique performed with a laser as the excitation source as it enables to measure relatively small Raman shifts with improved spatial resolution and signal to noise ratio. Regularly, the Raman signal intensity is orders of magnitude weaker than the elastic scattering intensity, hence stray light can be a considerable issue. Therefore, notch filters or edge filters (sharp cut-off high pass filters, triple monochromators, and single monochromator+filters) are usually used to reject the elastically scattered light prior to entering the spectrometer. Modern spectrometers use multiple monochromators with charge-coupled devices (CCDs) allowing the data to be collected and manipulated electronically. For instance they can be operated in an additive or subtractive mode accordingly to the resolution or suppression of straight light needed. The selection of the excitation wavelength (i.e. laser wavelength) depends on several factors. The Raman differential scattering cross-section (cm^2/sr) varies inversely with the fourth power of the excitation wavelength by the proportionality formula:

$$\sigma' \propto (\tilde{\nu}_0 - \tilde{\nu}_{vib})^4 \tag{2.7}$$

where $\tilde{\nu}_0$ is the wavenumber of the incident radiation ($1/\lambda_0$) and $\tilde{\nu}_{vib}$ is the wavenumber of the vibrational mode (ν_{vib}/c). The common unit for wavenumber (which is considered a unit of energy) is the cm^{-1}, and $\tilde{\nu}_{vib}$ generally ranges from about 200 to 4000 cm^{-1}. An important factor to take into account when resolving Raman features in the resulting spectrum, is the spectral resolution which can be improved by increasing the focal length or by adjusting the grating used. By duplicating the focal length, one can approximately double the spectral resolution. Likewise, by doubling the density of lines on the grating one can get improve twice the spectral resolution, but this is limited by different working ranges e.g. a grating with 2000 lines per mm cannot be used for infrared work. The wave length used for the analysis is highly important, and this one can be ranged from the infrared up-to ultraviolet, with its corresponding appropriate diffraction grating density. In addition, when a material presents fluorescence characteristics, one must select an appropriate wavelength (longer) which minimize this effect, otherwise this would may interfere and weak the Raman response. The use of ultraviolet lasers comes when the sample in question has no fluorescence effects. On the other hand, visible wavelengths are mostly easier to work with. Finally, the possibility to vary these factors to improve the Raman response of a sample has lead into different spectrometers with more than just one laser line which can be switched according to their needs and their corresponding filters to remove the Rayleigh scattered light.

Graphite, graphene, and carbon nanotubes have the specific and common property that their electronic bands locate in the visible region, and they are strongly dispersive. Their dispersion near the Fermi surface is in fact nearly linear, and the schematic in Fig. 1.8 a) describes the possible transitions in the Raman process in graphite and graphene. Basically, these transitions are resonant regardless of the photon induced energy [176, 178]. Moreover, the resonance Raman process has a greater sensitivity compared to its non-resonance counterparts [175]. The use of tunable lasers has been preferable employed in resonance Raman, which for instance is an advantage as one can simply tune the incident wave length over the same or different samples [175]. Then, the characterization procedure reduces to just changing the setting on the tunable laser over one sample. The resonance phenomenon is very sensitive to the energy of excitation wave. Particularly, by tuning the incident wave length, one can select an specific wave vector k which consequently will alter the Raman band frequencies observed for each wave length, making possible to describe phonon-dispersion curves characteristic in the double resonance graphene based materials bands.

The transition matrix $M(\omega)$ diverges for certain values when the energy of the incident wave matches an existing electronic transition in the solid. Then, it is possible to induce a coupling between electrons, and the induced phonons. The modeling of this phenomena involves the inverse of the energy difference between the phonon, and the transition in the electronic continuum. Thus, if the initial scattered level corresponds to an existing electronic level, a resonance effect will occur with a deformation of the absorption or emission band shape with subsequent increase of its intensity being called “Breit-Wigner-Fano effect” [179] characteristic in highly doped graphitic materials. The latter makes the use of a tunable resonance Raman set-up, suitable to conduct this thesis and fully characterize graphene, and graphite intercalation compounds.

2.1.1. Experimental setup used:

For this thesis a multi-frequency Raman micro-spectroscopy was used. In this system, a microscope is coupled to the laser source and we are able to capture the image of the analyzed region. The laboratory is equipped with a Horiba LabRam HR with a solid state 633 nm wave length, and a tunable innova 70C spectrum laser (647 nm, 568 nm, 532 nm, 514 nm, 488 nm, and 452 nm laser lines) in the following configuration:

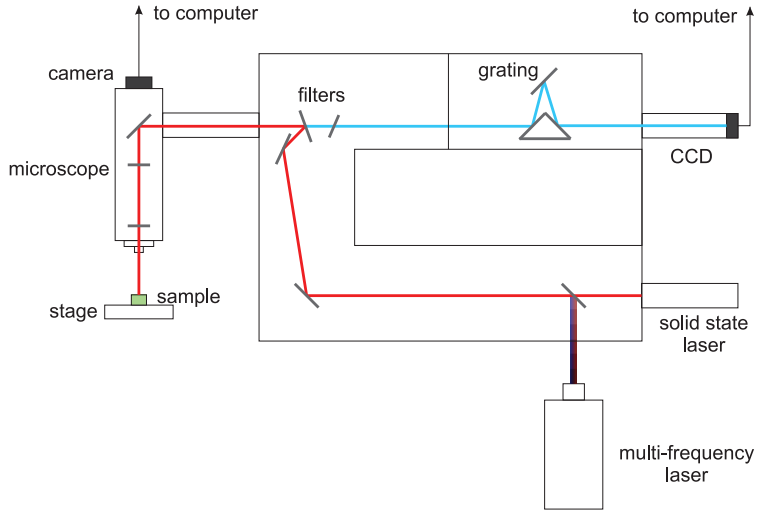

Figure 2.3: Schematic diagram from the Raman micro-spectroscopy equipment used for this thesis. EPM group, University of Vienna.

The LabRAM HR system in Fig. 2.4 provides ultra high spectroscopic and spacial resolution. The high resolution mode is specially design for fine band analyses like in crystalline or amorphous materials, of proteins, hydrogen and weak bonding forces and semiconductor stress measurements in fact most applications where it is important for the precise characterization of position or shape of the Raman spectral features. Band analysis in the order of 0.3 cm^{-1} to 1 cm^{-1} is particularly suited to the HR mode. Its dual capabilities also enable more routine Raman analysis and even broader band laser induced micro-fluorescence or luminescence to be conducted all upon the same bench-top instrument. Its large 1024 pixel CCD chip, gives the possibility to perform studies where the focal analysis region is important when studying highly intercalated graphitic compounds. Finally, the intensity can be modulated in a wide range, which is crucial to avoid laser induced annealing when analyzing a sample. In a more detailed way, in Fig. 2.5, a schematic close-up from the Raman acquisition and preparation region of the experimental setup is shown. Important aspects of this system are the necessity of a flat quartz tube long enough to insert a sample and an intercalant. There must exist two regions as in the two-zone vapor transport method in order to be able to fully control the temperature from the intercalant and the graphite sample (H_1, and H_2). The real setup design can be observed in Fig. 2.6, where the previous conditions were full-filled.

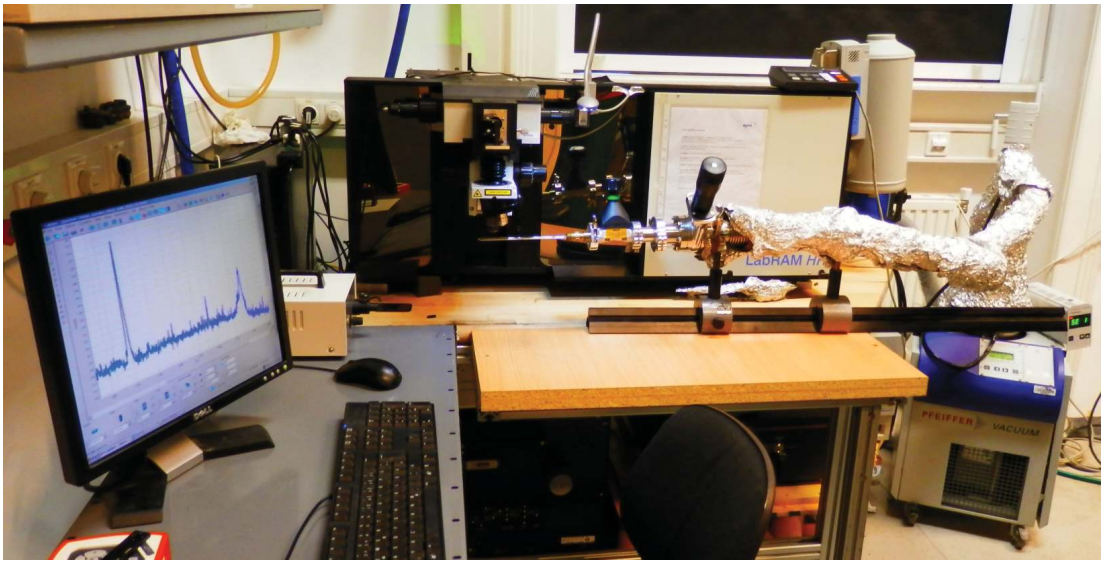

Figure 2.4.: Raman set-up system implemented for in-situ Raman spectrum analyses under High Vacuum conditions ($\sim 10^{-8}$ mbar).

At this point it is clear the importance in the use of Raman Spectroscopy in Graphite Intercalation Compounds, and Graphene. However, it is not the only nondestructive technique which can bring us a clear understanding of their behavior. As mentioned in section one, the electronic band structure in GICs, and graphene is highly sensible to changes in the electron concentration on the sample. This changes can be observed and recorded by examining the photons or electrons scattered by inducing a photon- or electron-beam respectively into the sample surface, which for instance will bring information related to the chemical composition and electronic structure of the material.

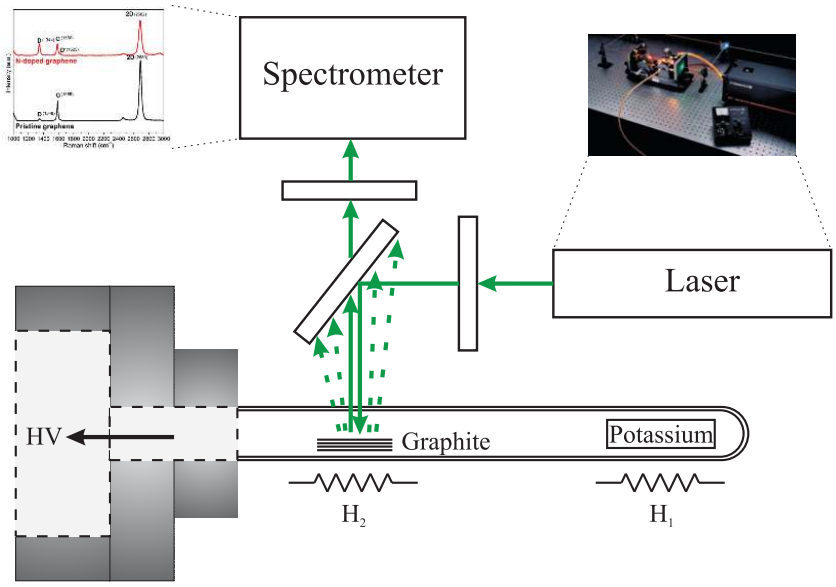

Figure 2.5.: Schematic representation from the experimental "set-up" used to synthesize controlled potassium graphite intercalation compounds. The samples were kept inside the quartz ampoule mean the Raman measurements were performed. The system was always under high-vacuum conditions. The measurements were conducted by using a Horiba LabRam with a tunable innova 70C spectrum laser.

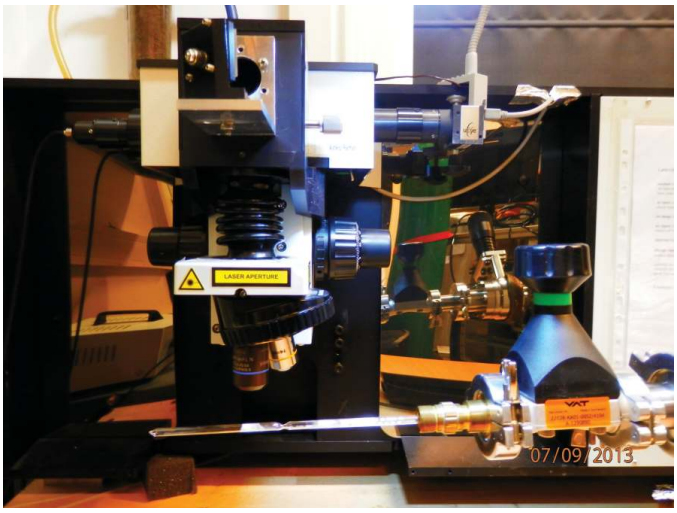

Figure 2.6: Purpose built High vacuum ampule system for controlled intercalation, and in-situ Raman analysis.

2.2. Photoemission Spectroscopy

"Light itself is quantized" – A. Einstein

The principle of photoemission spectroscopy is governed by the law of the Photoelectric Effect, which yield into the Nobel Prize to A. Einstein in 1921. The key to understanding the photoelectric effect comes from considering that all the light of a particular frequency comes in little bullets of the same energy (E), equal to the frequency (v) multiplied by Planck's constant ($\hbar$). Under this concept, Einstein was able to formulate the principle of the photoelectric effect in 1905 [180]. When an incoming light quantum smashes into an electron on the surface of a metal and gives up all of its energy to the electron, a certain amount of energy, called the work function (Φ_e) would be needed to overcome the force of attraction between the electron and the metallic lattice in order to set the electron free; so there can not be any photoelectric effect unless this threshold is reached. In other words, the photoelectron spectroscopy method occurs when energy is induced by a beam of photons ($\hbar\omega$), sufficiently enough to break a chemical bond of Energy (E_1), enter the vacuum with a kinetic energy E_{kin} and a certain momentum k (related to the emission angle Θ) and eject an electron from its orbit (see Fig. 2.7 a). The energy conveyed transcend the barrier of potential, and the electron will leave the solid with a kinetic energy E_c, which is recovered by an energy analyzer according to Eq. 2.8. Any energy left over from the exchange, above and beyond the work function, appears as kinetic energy of the ejected electron, and by increasing the frequency of radiation we would obtain a more energetic photoelectron. Due to the photoelectric effect, the liberation of photoelectrons which possess information on the chemical and the orbital character of the system occurs. This information is gained with respect to emission angle and kinetic energy by an electrostatic analyzer Fig. 2.7 a).

$$\hbar\omega; = E_1 + \Phi_e + E_c \tag{2.8}$$

Photoemision Spectroscopy (PES), also known as photoelectron spectroscopy [76], refers to an energy measurement of electrons emitted from solids, gases or liquids by the photoelectric effect which refers to the minimum work required to extract an electron from its orbit. PES introduces various techniques like: Ultraviolet photoelectron spectroscopy (UPS), X-ray photoelectron spectroscopy (XPS), Angle-resolved photoelectron spectroscopy (ARPES), X-ray Absorption Spectroscopy (XAS) which includes both Extended X-Ray Absorption Fine Structure (EXAFS) and X-ray Absorption Near Edge Structure (XANES), etc. (see Fig. 2.7 b). PES was first developed by K. Siegbahn in 1956, allowing the determination of the electronic environment by measuring chemical shifts and it is called electron spectroscopy for chemical analysis (ESCA)[†] [33]. Within the frame work of this thesis, I will give a compact overview about the two most often used spectroscopic methods (XPS, and UPS) so that the reader may follow the results presented in section 4.5 and 4.6 regarding nitrogen doped graphene, and graphite intercalation compounds. Basically, one distinguishes between ultraviolet photoemission spectroscopy

[†]K. Siegbahn obtained the Nobel Prize in Physics for developing the method of Electron Spectroscopy for Chemical Analysis (ESCA) in 1981.

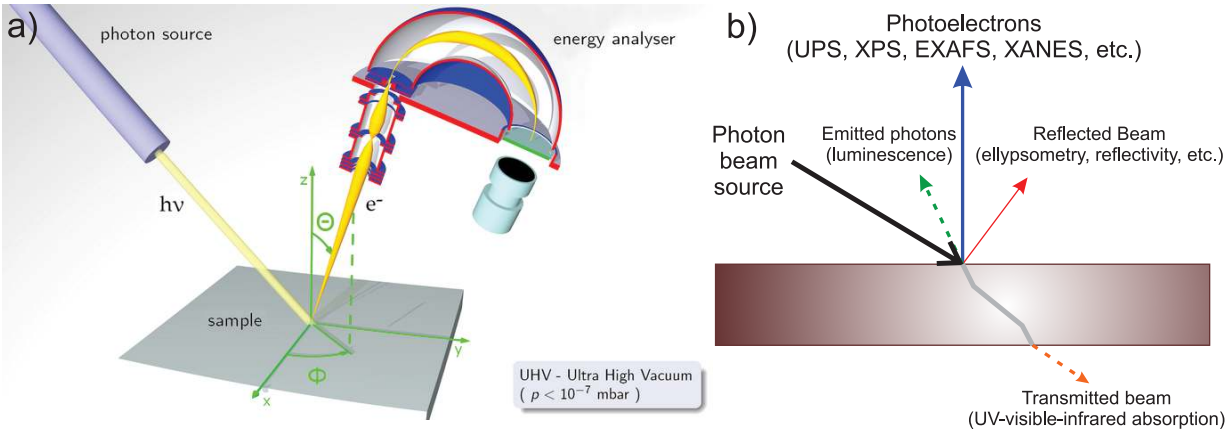

Figure 2.7.: Schematic diagram of the radiation-matter interaction processes with a photon beam.

(UPS), mainly for the investigation of valence band states and X-ray photoemission spectroscopy (XPS), providing the investigation of core-level states at higher binding energies (see Fig. 2.8 a). By XPS, the chemical composition of the sample can be determined since the binding energy of an electron is characteristic of the element, orbital and chemical environment.

The study of solids by XPS or UPS spectroscopy is described as a *Three-Step Model* [181] Fig. 2.8 b). Whereas in a gas-phase experiment an electron is ejected into a simple continuum orbital, in the solid state the photoemission process is more complex leading into a three-step process:

- **Absorption and Excitation:** Electrons are excited with a known photon energy, the energy distribution of these excited electrons will reflect the energy distribution of the initial states from which they came, which in the one-electron approximation, this energy distribution will reflect the density of occupied states of the material. If the energy level of the excited electron is higher than the vacuum level of the sample, then the electron has the possibility to escape the crystal and be detected by an electron energy analyzer.
- **Propagation to the surface:** During this transport process, the electron may be scattered and lose energy, becoming what is known as a secondary electron. These secondaries will give a background to the photoemission spectrum which the primaries will ride upon. The mean free path for these scattering events determines the surface sensitivity for photoemission, as only the primary or unscattered electrons retain the energy information that is needed. The mean free path of an electron in a solid is a strong function of its kinetic energy, and follows what has become known as the universal curve [182].
- **Transition into the vacuum:** The final state is the electron escape from the surface. To do this, the electron must overcome the surface work function, which in the simple picture will simply cause the electron to lose some energy (*i.e.* there will be a rigid shift of the spectrum).

The photoelectrons that actually escaped into the vacuum are collected, energy resolved, slightly retarded and counted, which results in a spectrum of electron intensity as a function

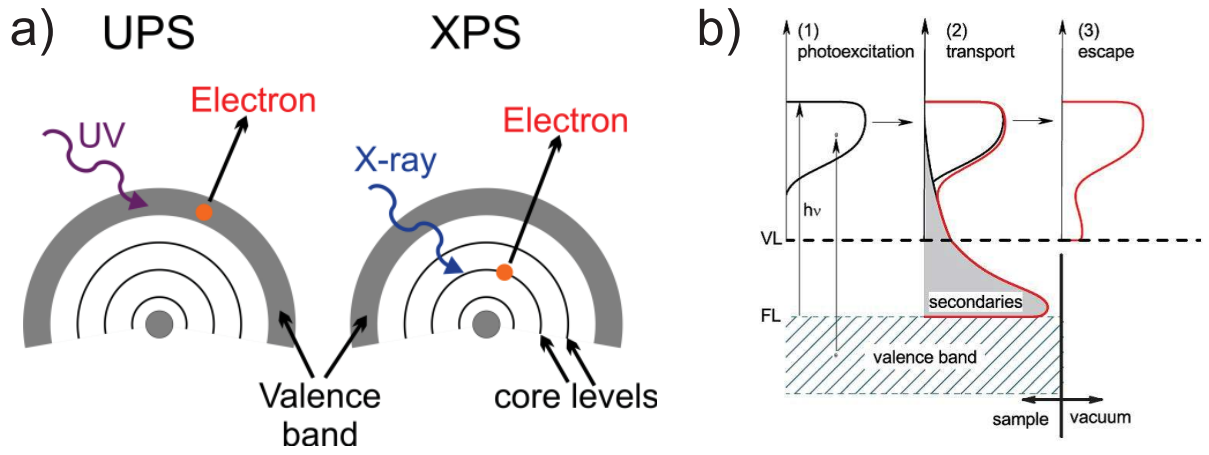

Figure 2.8.: In the left panel a), the schematic XPS and UPS scattering processes are depicted. The spectroscopic study is described as a *Three-Step Model* is shown in b) acording to Ref. [181]

of the measured kinetic energy. Because binding energy values are more readily applied and understood, the kinetic energy values, which are source dependent, are converted into binding energy values, which are source independent by using the following Eq.:

$$E_k = kv - E_B \tag{2.9}$$

The binding energies of the measured electrons are characteristic of the chemical structure and molecular bonding of the material. The final spectra obtained from core levels can be compared with tabulated references from PES-Handbooks to determine the element and the lineshape which gives insights into the effective charge distribution around the specific element. For instance, and example of an spectrum can be seen in Fig. 2.9 from our results [183] in which different nitrogen environments exist in doped graphene and changes regarding line-shape and position of the spectrum are evident with respect to the pristine sample. More details about the application of this technique in doped graphene samples will be presented in section 4.5.

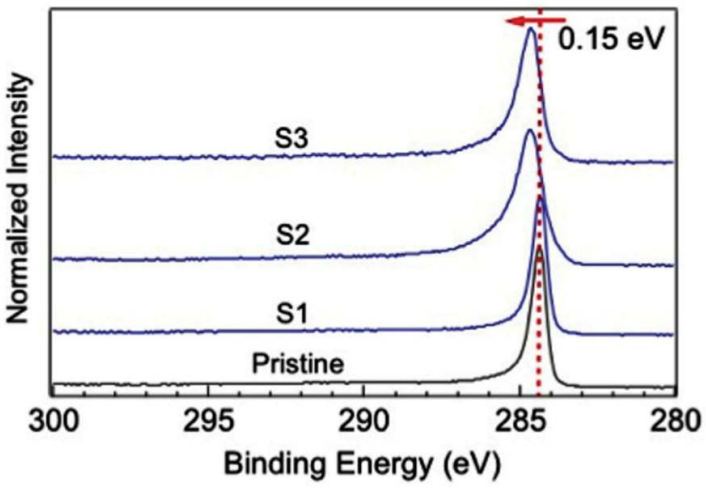

Figure 2.9: XPS spectra recorded for the C 1s line with a photon excitation energy of 1486.6 eV. The bottom most spectrum (shown in black) corresponds to pristine graphene while the spectra in blue are for increasingly N-doped graphene. Clearly, the C 1s line is broadened for samples S2, S3 and is up-shifted in energy with increasing (from S1 to S3) dopant concentration as shown in our results in section 4.5.

In order to visualize band structure of graphene, it has been shown that graphite in its KC_8 potassium intercalation face, can resolve graphene's electronic band structure along the high symmetry points **H** and **K** [62, 124]. At the **H** point of graphite the band dispersion is close to linear and has been interpreted as Dirac-fermion-like. Furthermore, it is important to know the exact k_z dispersion, because it is responsible for the conductivity perpendicular to the graphene layers as it is the case of CaC_6, and KC_8. By a combination of Angle-resolved photoemission (ARPES) studies, local density approximation (LDA), ab initio calculations, the experimental band structure of few-layer graphene and graphite can be For instance, Grüeneis et al. [124] synthesized KC_8 in-situ and performed high-resolution ARPES measurements. By using this technique, they were able to find an almost complete charge transfer of potassium to graphene and the complete absence of interlayer interaction. By measuring the conical band dispersion of KC_8 they had access to the valence and conduction Dirac Fermions of graphene (see Fig. 1.14) unraveling the full experimental Dirac cone of graphene and evaluated the anisotropy of the momentum dependent v_F in the valence and conduction band resolved as reported in the work from Grüeneis et al. [62, 124].

2.2.1. Experimental setup used in photoemission spectroscopy

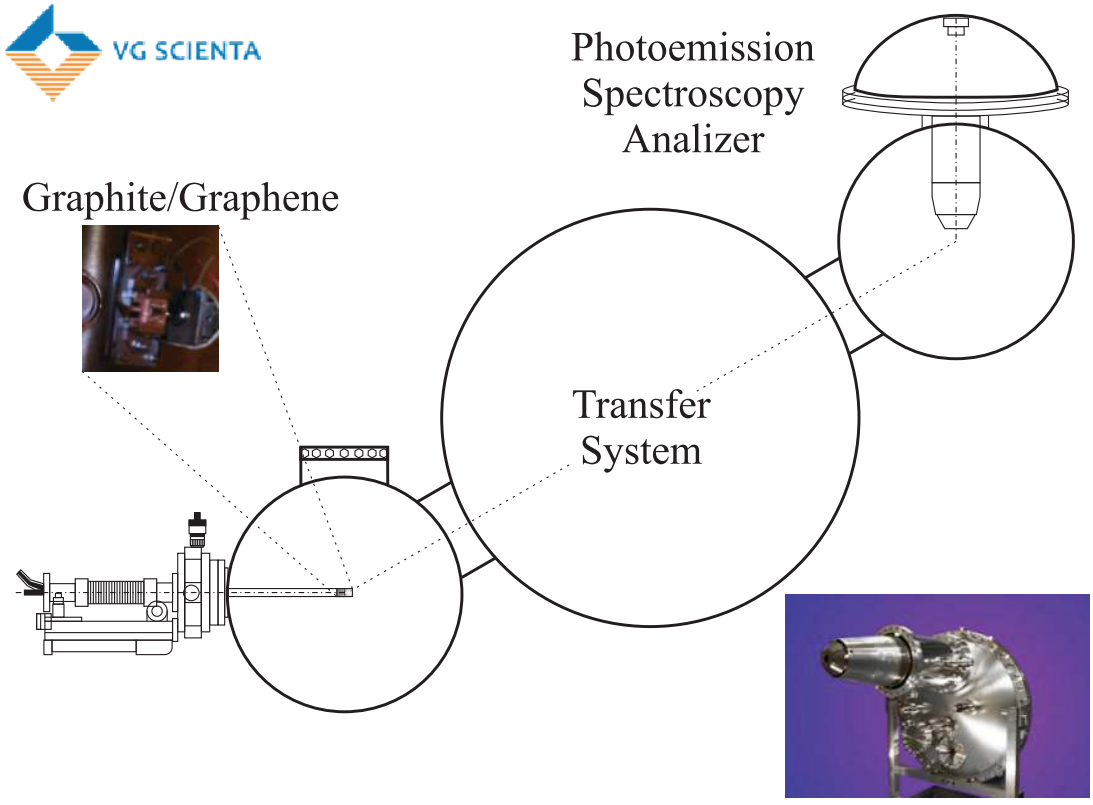

Figure 2.10.: Schematic photoemission spectroscopy setup used to characterize samples by XPS, UPS or ARPES at the our group from Prof. Pichler, University of Vienna.

2.3. Density Functional Theory

The Density Functional Theory (DFT) is a quantum mechanical method commonly used in physics to investigate the electronic structure of many-body systems. With this theory, the properties of a many-electron system can be driven by using functionals (functions of another function), which in this case is the spatially dependent electron density. Therefore, the name of "Density Functional Theory" (DFT) comes from the fact of using functionals of the electronic density. In the majority of the cases the results of DFT calculations for solid-state systems bring suitable results compared with experimental data, and strongly depends on the functional used. One of the main advantages of using this method is its low computational costs when compared to traditional methods, such as HartreeFock theory and its descendants based on the complex many-electron wave function. The later is highly important when analyzing molecules as GICs as they structural properties can only be studied by constructing super cells with several atoms, which for instance has a high computational cost. DFT is among one of the most common-versatile methods when studying condensed-matter physics, computational physics, and computational chemistry. Different computational programs had been developed based in this DFT method, i.e. Vienna Ab initio Simulation Package (VASP), QUANTUM-ESPRESSO, ABINIT, GPAW, Gaussian, etc. In order to further study and confirm the experimental Raman results obtained in GICs we have chosen QUANTUM-ESPRESSO (a DFT software) to calculate the electronic properties, charge transfer and phonon dispersion in or system as will be described in the following.

2.3.1. QUANTUM ESPRESSO

An *opEn Source Package for Research in Electronic Structure, Simulation, and Optimization* (ESPRESSO) is an integration of a diverse computer codes for electronic-structure calculations and materials modeling, based on density-functional theory, plane waves, and pseudopotentials (norm-conserving, ultra soft, and projector-augmented wave) to represent the electronion interactions [184]. The input codes in QUANTUM ESPRESSO are constructed by using periodic boundary conditions, which permits the direct analysis of infinite crystalline systems, with an efficient convergence at the thermodynamic limit in aperiodic extended systems like liquids or amorphous materials. Finite systems can be modeled as super cells wit or without open boundary conditions. This, QUANTUM ESPRESSO can be used for any kind of crystal or super cell, and for metals as well as insulators.

In our case, we have periodic supercell systems in which carbon and potassium atoms must be represented. Many different exchangecorrelation functionals are available in the framework of the local-density (LDA) or generalized-gradient approximation (GGA) [189] which have been used to model GICs electronic properties [62, 124]. However, the use of these functional can lead into a not entirely correct results with respect to the phonon frequency response in graphitic systems. This has been demonstrated by Lazzeri *et al.* [185] when analyzing the phonon dispersion of graphite and graphene as shown in Fig. 2.11. This analysis is based in the electron phonon coupling (EPC) of graphite/graphene. The EPC is a fundamental quantity parameter in condensed matter as it It determines phonon dispersions and Kohn anomalies, phonon-mediated

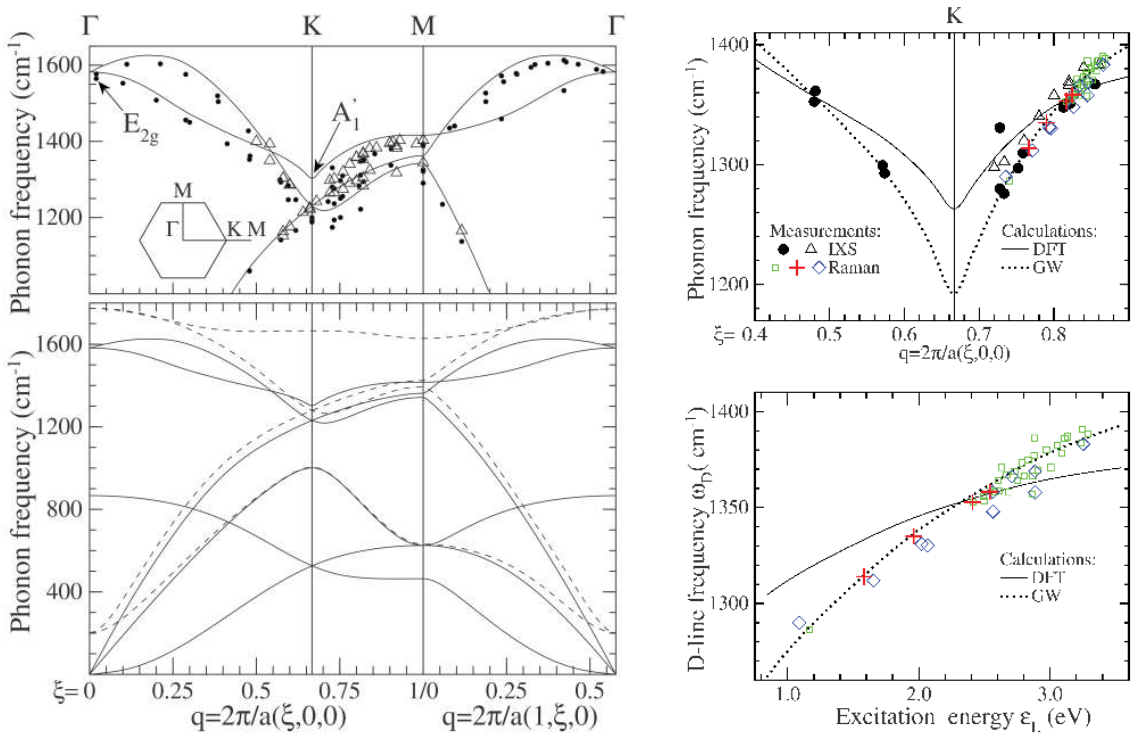

Figure 2.11.: Failure of LDA and GGA DFT functionals in graphene and graphite adapted from Ref. [185]. Left upper panel: Phonon dispersion of graphite. Lines are DFT calculations, dots and triangles are IXS measurements from Refs. [64] and [65], respectively. Left lower panel: Phonon dispersion of graphene from DFT calculations. Dashed lines are obtained by subtracting, from the dynamical matrix, the phonon self-energy between the π bands. Right upper panel: Dispersion of the highest optical phonon in graphite near K. Calculations are from DFT or corrected to include GW renormalization of the EPC. Here, the DFT dispersion is vertically shifted by -40 cm^{-1} to fit measurements. Dots and triangles are IXS data from Refs. [64] and [65], respectively. Squares, plus, and diamonds are obtained from Raman data of Refs. [63, 186, 187], respectively, using the double-resonance model (Refs. [63] and [188]). Right lower panel: Dispersion of the Raman D line.

superconductivity, electrical resistivity, Jahn-Teller distortions, etc. In the case of GICs, the coupling between electrons and phonons (lattice vibrations) drives to the formation of electron pairs responsible for conventional superconductivity. It also determines the Raman spectrum, which is the characterization technique used in this thesis for graphene and graphite. As mentioned, the ability of DFT calculations based in LDA and GGA functionals to accurate describe the EPC (see Fig. 1.7 a) of graphene has been questioned [190]. In Ref. [185] it is proof this failure in the next way: (i) the GW approach, which provides the most accurate *ab-initio* treatment of electron correlation, can be used to compute the electron-phonon interaction and the phonon dispersion; (ii) in graphite and graphene, DFT (LDA and GGA) underestimates, by a factor of 2, the slope of the phonon dispersion of the highest optical branch at the zone boundary and the square of its EPC by almost 80%; (iii) GW reproduces the experimental phonon dispersion near the K-point,

the value of the EPC, and the electronic band dispersion; (iv) by applying a hybrid functional (B3LYP) a brings better agreement of the phonons close to the GW but but overestimates the EPC at K by about 30%; and (v) within Hartree-Fock the graphite structure is unstable.

In order to solve these previous uncertainties, we chose to use QUANTUM ESPRESSO in its modality to work with norm-conserving Pseudo Potentials, which is a more simple procedure to extract pseudopotentials from *ab-initio* atomic calculations [191]. Pseudopotentials were originally introduced to simplify electronic structure calculations by eliminating the need to include atomic core states and the strong potentials responsible for binding them. Moreover, these pseudopotentials yield exact eigenvalues and nonetheless eigenfunctions which agree with atomic wave functions beyond a chosen radius r_c and thus could bring an accurate representation from the atomic displacements in a vibrating Raman system. As it was already explained in section 2.1, the spectroscopic selection rule is based directly on the position of the atoms with respect to their equilibrium position. One of the main differences between different theoretical approaches is the way in which the electronic wave functions and the atomic displacements are considered. By using QUANTUM ESPRESSO one can extract the KohnSham (KS) orbitals and energies for isolated or extended/periodic systems, and of their ground-state energies. Also complete structural optimizations, ground state of magnetic or spin-polarized systems, *ab-initio* molecular dynamics, and density-functional perturbation theory to calculate the total energy at any arbitrary wavelength, providing phonon dispersions, electronphonon and phononphonon interactions, and static response functions (dielectric tensors, Born effective charges, infrared spectra, Raman tensors) which we are interested on.

For this thesis the PHonon package from QUANTUM ESPRESSO is the one which includes all the characteristics previously mentioned. This package implements density-functional perturbation theory (DFPT) for the calculations of second- and third-order derivatives of the energy with respect to atomic displacements and to electric fields. Recently, Profeta *et al.* [192] have shown a pretty nice agreement in their calculations regarding intercalation compounds of graphite (CaC_6, and LiC_6) which highlights the use of this technique to proof our results.

In that paper, Profeta *et al.* had proof the possibility to simulate an electron doped graphene system by introducing Li add atoms in to the structure which for instance gives information on the charge carrier density of these system. Moreover, the interlayer distance in Ca and Li intercalation compounds seems to play a crucial roll in the superconducting behavior of GICs. The later is (as mentioned in the motivation of this thesis) a highlight in using phonon calculations to further understand the behavior in graphite intercalation compounds as will be shown in section 4.4.

Chapter 3

SAMPLE PREPARATION

During the time this PhD was conducted, four main samples were used: (S01) p-doped Graphite intercalated with potassium, from University of Liverpool, (S02) Graphite intercalated with calcium and lithium, and (S03) Nitrogen-doped graphene.

3.1. S01 – Potassium graphite intercalated compounds

The preparation of GICs has never been trivial as it is not easy to control the proportions of intercalant and keep them constant along the measurements. The majority of the experiments have been performed using the *two-zone vapor transport method* (see Fig. 3.1 a) [27]. In this method, the intercalant is typically heated to some temperature T_i, while the graphite (some distance away) is heated to a higher temperature T_g as can be seen in Fig. 3.1. The stage of the compound is then controlled by the temperature difference $T_g - T_i$ as depicted in the graph of Fig. 3.1 b). The region of stability for the formation of a given stage compound decreases with increasing temperature difference $T_g - T_i$ (or equivalently with increasing stage index) as can be denoted from Fig. 3.1 b). Therefore, one of the main problems when synthesizing their low-stages compounds is their stability. As one can see in Fig. 3.1 b), for a $\Delta T < 100^o$C, one can reach a stable *stage I* face. For values of ΔT between 100 and 200^{o}C *stage II* can be obtained in a stable face. By enlarging the temperature difference, one can reach higher stages going from III to *n* in principle. However, the previous is a pretty difficult step as there exist no plateau ΔT region to further stabilize the compound. The stability formation of this compounds, plus the difficulty of an homogeneous intercalated region in the crystal, are key factors for a successful experiment in GICs. The evident change of color when intercalation is induced in graphite, has been used as a visual inspection which gives qualitative information on the stage: for example, for the alkali metal compounds a yellow, gold or red color is characteristic of *stage I* compounds, steel blue for *stage II*, dark blue for *stage III* and graphite-metallic for higher stages [82]. For acceptor compounds, *stage I* is often blue and higher stage compounds graphite-metallic. However, if we observe Fig. 3.3 there are six optical images from the same region at different intercalation

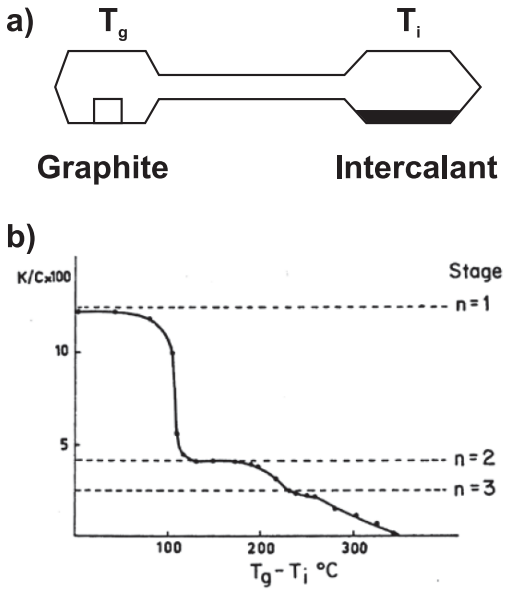

Figure 3.1: *The two-zone vapor transport method* a)Schematic diagram of an ampoule depicting the location of the two-zones, where T_g, and T_i indicate the temperatures of graphite and intercalant respectively. b) Isobar graph for growing conditions in graphite-K compounds (intercalant uptake versus temperature difference). Image taken and adapted from [27].

steps acquired with a 100x microscope objective during intercalation. In panel a) the highest intercalation obtained called *stage I* (KC_8) is shown. However, one can clearly observe that the sample is not homogeneously intercalated which means that it is polycrystalline and may lie due to the presence of different intercalation regions. As we move forward in b) to f), we can see how does the sample change in color from a semi yellow to red, then green and further brown-green. The previous is an indication about the stability of the sample in the isobaric growth graphite-K stage. The effect of color change is related to the fact that a particular color is absorbed from the sample, and our eye detects by mixing up all the other wavelengths of light is its complementary color. For the case of Fig. 3.3, a yellow light was used during the micrographies where acquired, and my be reason why *stage II* is not blue, however when observing it by eye (Fig. 3.4 b) it looks blue due to the white light from the surroundings. For instance, this color change behavior is directly related with increasing of intercalant concentration, which induces a change in the band structure of graphite going from a two-carrier semi-metal (pure graphite), through one-carrier free-electron-like metal in the dilute regime (KC_{24}), to a band-overlap metal at high concentration (KC_8). The later had been proven by reflectivity studies [89] as can be seen in Fig.3.2 a) and c) where the Drude-like free-electron spectra for light polarized, parallel (blue) and perpendicular (black) to the c-axes in GICs where recorded. The reflectance spectra of KC_8, and KC_{24} are depicted in Fig.3.2 a, b and c, d) respectively. In the right panels, the spectrum as function of frequency ($\hbar\omega$) are characteristic of metals exhibiting a sharp Drude edge in the visible region with values around 4.51 eV for KC_8, and 4.20 eV for KC_24. These edge positions are located near the screened plasma frequency ω_p are largely responsible for the characteristic color in highly intercalated graphite intercalated donor compounds.

The previous observations, bring an insight in the precisely confirmation of the stage by a combined visual image, and spectroscopic analysis. Although each intercalant requires a special set of grown conditions, these conditions are closely related for intercalants with similar chemical

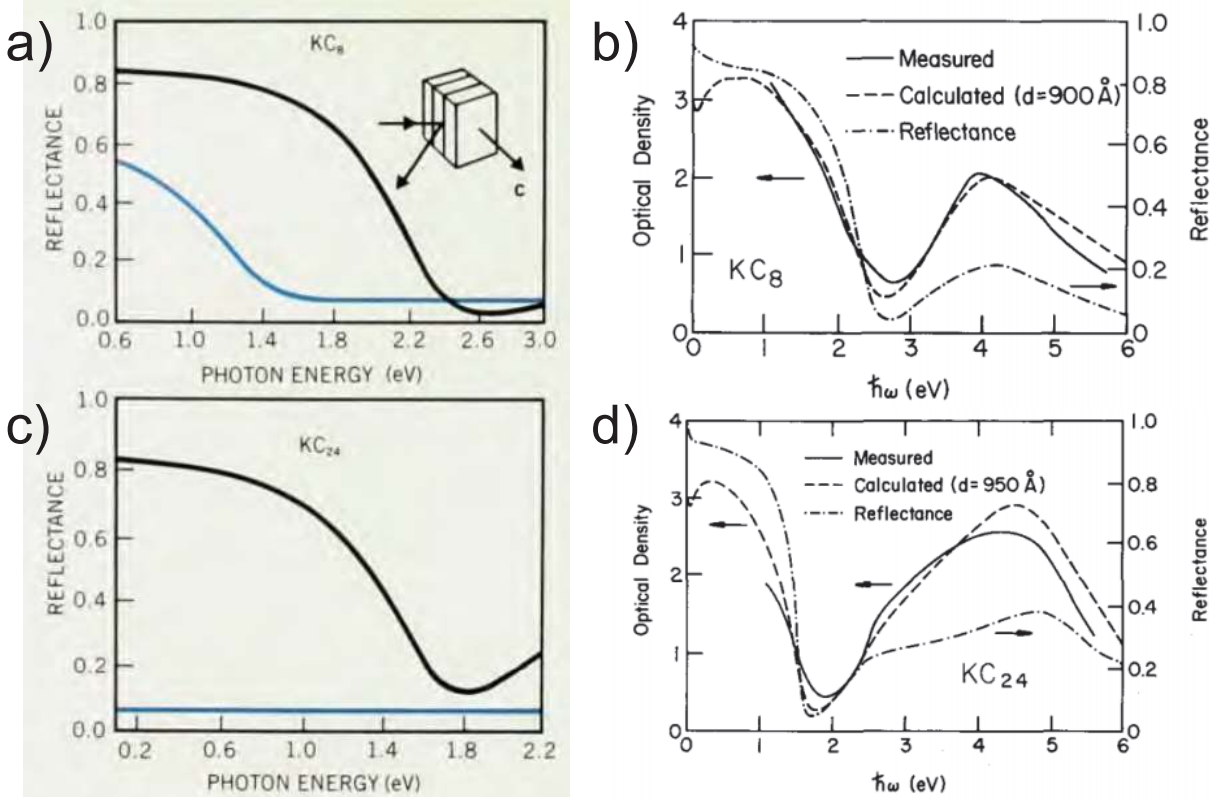

Figure 3.2.: Reflectivity spectra obtained from references [89] and [193]. In the left panels, curves with the polarization perpendicular to the c axis (black) and parallel (blue) are shown. a) textitStage I KC_8 exhibits metallic behavior for both polarizations, indicating strong interlayer coupling. The spectrum for the *stage 2* compound KC_{24} c) is metallic parallel to the layers but insulating across them, indicating greater anisotropy in the electronic structure of KC_{24}. In the right panels, a comparison of experimental (solid line) and calculated (dashed line) optical density D(ω)/Reflectance versus photon energy $\hbar\omega$ for KC_8 b), and KC_{24} d) are depicted.

properties. For instance, alkali metal donor compounds as K, Rb, and Cs are all prepared by using the same *two-zone vapor transport method* varying the T_g to control the stage, and keeping constant T_i, thereby giving raise to a fixed pressure grown conditions [97]. The preparation of acceptor compounds with graphite has also been carried out using the *two-zone vapor* technique, however, the grown conditions are different. In comparison to a donor compound, the intercalant is in a molecular form, and therefore a larger *c-axis* expansion of graphite is needed to contain the intercalant [27]. Under this conditions, the temperature of the intercalant (T_i) must be varied while the T_g of graphite remains constant. After understanding the *two-zone vapor* technique, one of the remaining open questions was: How to control the stage in potassium GICs increasing their stability time, long enough to be measured and studied in an in-situ experiment.

For this purpose, a unique purpose built in-situ Raman doping cell was developed, which has been adapted from a previous set-up design for fullerene intercalation [194].

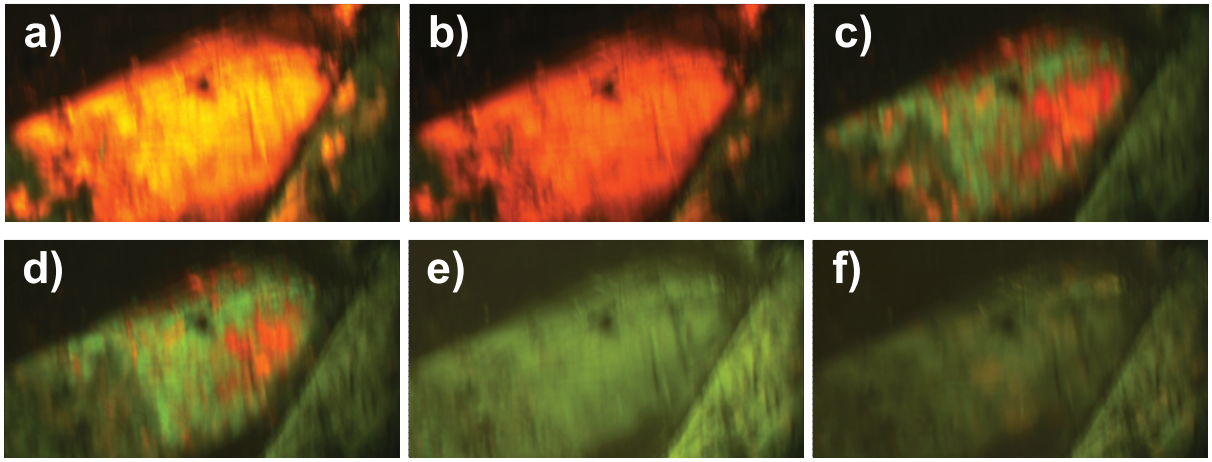

Figure 3.3.: Micrographies of the change in the crystal color according to the content of potassium. Multi-crystalline highly oriented pirolytic graphite (HOPG). a) Mixed KC_{24} and KC_8 regions, b) Defective KC_8, c)-d) Mixed KC_{24} and defective KC_8. e) Homogeneous KC_{24}, and f) Mixed KC_{24} and defective KC_{36} faces.

In order to resolve this query, we considered two main important factors which should be introduced for our purpose built "set-up" in-situ experiment:

1. The sample (GIC) must be kept under high vacuum conditions or an inert atmosphere in order to elongate its stability.

2. One must be able to intercalate or de-intercalate potassium at will

The intercalation experiments were carried out on natural graphite single crystals *in-situ* in a vacuum better than $\sim$4x10^{-8} mbar keeping the graphite sample inside a quartz ampoule with a flat surface. Potassium with a 99.95% purity (Aldrich) was evaporated until bright golden graphite crystals which are assigned to stage I KC_8 were obtained (Fig. 3.4 a). Subsequently, the sample was resistively heated to 200°C until it turned homogeneously blue characteristic color of stage II KC_{24} (Fig. 3.4 b). A controlled *in-situ* high vacuum high temperature de-intercalation process was performed by increasing the temperature in steps of 50°C [27]. Six potassium GIC *stage I* to *VI* (KC_8, KC_{24}, KC_{36}, KC_{48}, KC_{60}, and KC_{72}) by using a 568 nm wave length. Once each stage was identified we followed a protocol acquiring multi-frequency Raman spectra keeping constant the acquisition region, and maintaining the lowest possible exposure time to avoid laser induced de-intercalation as for instance reported by [60] and later on by us [57]. The Raman measurements have been performed using 458, 488, 514, 568, and 647 nm excitation wavelengths at 0.257 mW and 1.2 mW respectively for stage I and further stages (II to VI). The acquisition region was defined between 300 cm^{-1} and 3000 cm^{-1}, and the line positions were corrected by employing calibration lamps.

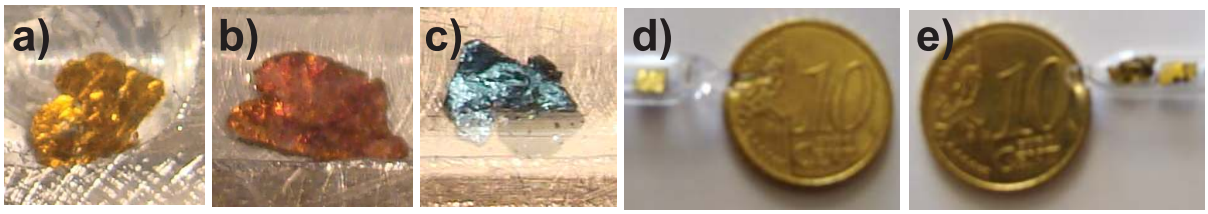

Figure 3.4.: Graphite intercalation compounds synthesized in-situ by using the set-up explained in Fig. 2.5 (a-c), and using method of Ref. [28] (d-e). a) Stage I KC_8 (Golden bright color), b) Partial intercalated stage I, c) Stage II KC_{24} (Blue). d) Stage I CaC_6, and e) Stage I LiC_6 compounds (Golden bright).

3.2. S02 – CaC_6 and LiC_6 graphite intercalation compounds

CaC_6, and LiC_6 samples were prepared at the Department of Chemistry from the University of Liverpool by Dr. A. Y. Ganin following a procedure described in Ref. [28]. Thus, highly oriented pirolytic graphite (HOPG) flakes were degassed and used for lithium and calcium intercalation. The reaction was carried out for ten days between HOPG platelet and a molten lithium-calcium alloy at around 350°C, under argon atmosphere (ca. 0.5 atm). The ampoule was then opened in the glove box and gold colored product was extracted from the melt, and kept into a sealed ampoule (see Fig. 3.4 d and e). Powder x-ray diffraction measurements were carried out using a Stadi-P diffractometer (CuK_a) to confirm the intercalation stage in CaC_6 and LiC_6. For the Raman analysis every GIC was kept in vacuum ($\sim$4x10^{-8} mbar) in order to avoid de-intercalation due to exposure to air. The Raman analysis, was performed with a HORIBA LabRam at room temperature, with a 568 nm wave length, and 0.25 mW of laser power. Every spectrum were acquired under the same conditions in a range from 500 cm^{-1} up to 2500 cm^{-1} and the line positions were calibrated by gauge lamps.

3.3. S03 – Nitrogen-doped graphene

The graphene samples used in this study were grown on Cu substrates using the thermal CVD technique [136, 147–150]. Briefly, Cu foils ($\sim$5 mm x 20 mm) were placed in a 1 in.quartz tube furnace and heated to 1000°C in the presence of 50 sccm of H_2 and 450 sccm of Ar. Next, 2 sccm of methane were bubbled through a mixture of benzylamine and acetonitrile into the furnace for 30 min, and the samples were finally cooled at room temperature under flowing H_2, Ar, and CH_4 (see Fig. 3.5). The volume percent of benzylamine and acetonitrile was varied as 1:1, 0:1, and 3:1, and the resulting graphene are referred as samples S1, S2, and S3. A Dilor XY triple grating monochromator was used for collecting the micro-Raman spectra (50x-100x) of all samples with the 514.5 nm excitation from an Ar^+ ion laser. XPS studies were performed in a Phi spectrometer equipped with a monochromatic Al Kα source (1486.6 eV), which has an overall resolution of 0.5 eV. Using a small spot size of ca. 0.5 mm, it has been possible to analyze the pristine and doped graphene in identifiable regions.

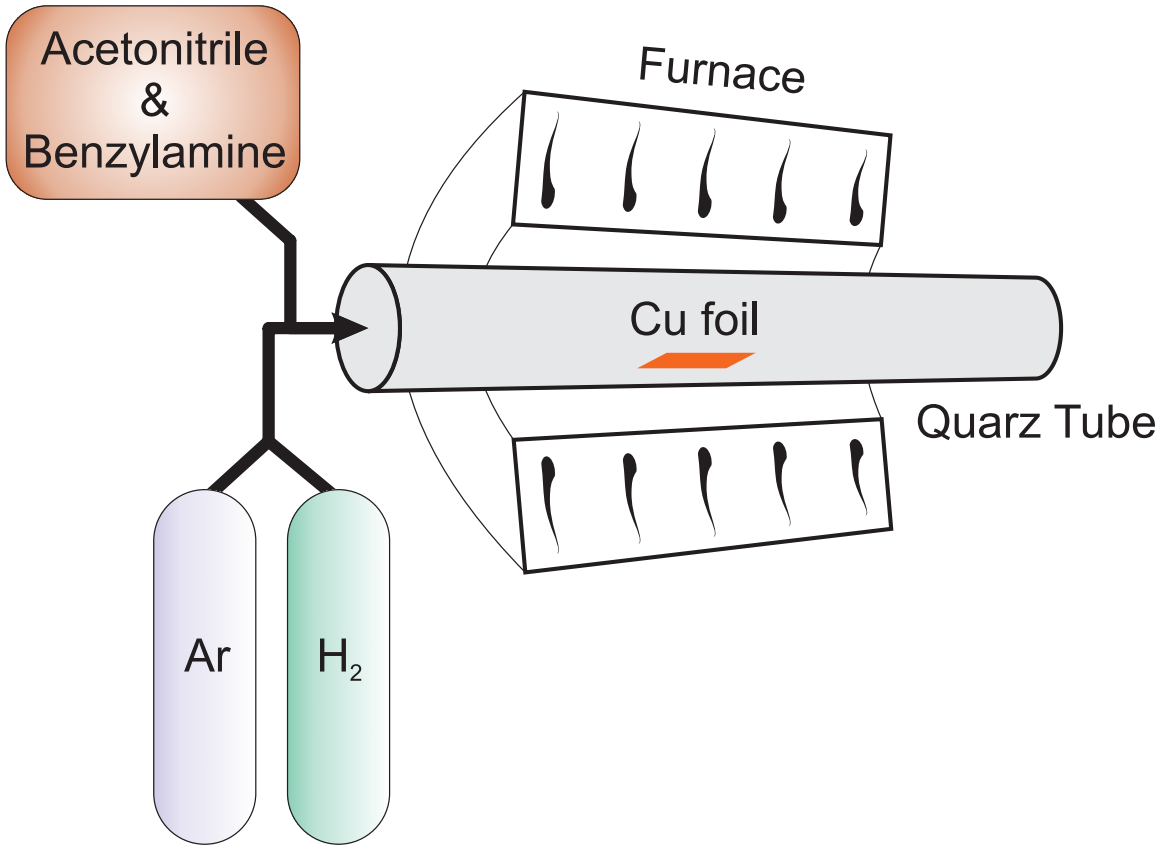

Figure 3.5.: Schematic CVD setup used to grow N-doped graphene on cooper foils. The elaboration of this samples was done at the Department of Physics and Astronomy in Clemson University, South Carolina, USA.

Chapter 4

RESULTS AND DISCUSSION

This chapter is mainly the essential part of this thesis as it contains a compilation of papers in which the results obtained are summarized. This part of the thesis has been organized according to the chronological way in which the samples were studied and the results revealed. The introduction and experimental parts have been mostly summarized along the introduction chapter, and just a short introduction paragraph is presented when needed.

In section 4.1 we present the first publication which mainly explain how to identify a stage I potassium graphite intercalation compound. By only using Raman spectroscopy we prove that the intrinsic **G-line** of KC_8 is at 1510 cm^{-1}, and it is strongly dependent on the actual defect content in the sample, which has important implications for the electron phonon coupling responsible of superconductivity in this system. [135].

Section 4.2 gives a wider panorama in superconducting stage I GICs. From a detailed line-shape Raman analysis of KC_8, CaC_6, and LiC_6 crystals we were able to disentangle the contribution from each vibrational mode in GICs. Going beyond in this analysis, the comparison to the theoretical calculated line width and position of each component allow us to extract the electron-phonon coupling constant of these compounds. A coupling constant $\lambda_{ph} < 0.06$ was obtained, which highlights that Raman active modes "alone" are not sufficient to explain the superconductivity within the electron-phonon coupling mechanism in CaC_6 and KC_8. [57]

One of the main problems when studying stage I GICs by Raman spectroscopy is laser induced de-intercalation [60, 85, 119, 133]. Thus, we decided to induce local heating of the samples by using a high laser power (8.5 mW) in order to study the de-intercalation process from *Stage-1* to *Stage-2* GICs [195]. In section 4.3, a detailed Raman line-shape analysis was performed from the recorded spectra to determine the changes from the G-line response of the KC_8, CaC_6, and LiC_6 samples. We confirmed the assignment of the broad E_{2g} Fano mode at $\sim$1510 cm^{-1} to the intrinsic *Stage-1* Raman response in GICs. Additionally, the most evident change from *Stage-1* to *Stage-2* was observed in an asymmetric Fano mode in the range of 1565-1610 cm^{-1}. This mode is linked to the first-order stretching Raman mode of Graphite, which tends to increase in frequency and decrease in width as function of de-intercalation. Finally, the response of the *Stage-2* phase after de-intercalation was confirmed to be a useful benchmark for the identification of the intercalation stage in highly doped GICs.

Once the process of intercalation, and de-intercalation were fully understood, our next task was to prepare lower intercalation compounds with potassium. As we mention in the introduction and motivation, from the well known nearest layer model, one can in principle study semi-free standing mono and multi-layer graphene by studying the inner graphene layer from stages $\geq$ III. Therefore, in section 4.4 we were able to proof this previous statement by extracting the charged and strained graphene layers contribution within the Raman response of potassium graphite intercalation compounds. This section compiles the whole bunch of experiments, Raman analysis, theoretical *ab-initio* calculations, and discussions carried during the three years of PhD work as reported in Ref. [196].

Last but not least, section 4.5 brings a confirmation of the Raman modes observable in N-doped graphene [183]. Here several Raman features vary depending upon both dopant concentration and its bonding environment were found and described. For instance, only pyridinic/pyrrolic dopants were observed to result in intense D/D$'$-bands with a concomitant downshift in the G$'$-band. Here, we correlate X-ray photoelectron measurements with Raman spectra to elucidate effects of dopant bonding configuration on vibrational properties of graphene.

4.1. Defect modulated Raman response of KC_8 single crystals

Published in: Physica Status Solidi B, **248**, 2744 (2011) doi: 10.1002/pssb.201100135 [135]

In this section, From a Breit-Wigner-Fano lineshape analysis of the Raman response in *stage I* KC_8 we disentangle contribution, and origin of each vibrational mode observed. We prove that the intrinsic **G-line** of KC_8 locates at 1510 cm^{-1}, and it is strongly dependent on the actual defect content in the sample, which has important implications for the electron phonon coupling responsible of superconductivity in this system. Moreover, the intensity of the *z-axis* mode (C_Z) around $\sim$560 cm^{-1} was analyzed, and reveals variations depending on the defect modulated nominal KC_8 crystal chosen.

The experiments were performed in-situ under high vacuum (HV) $\sim 4x10^{-8}$ mbar conditions in a quartz tube with natural graphite flake crystals from different sources, and a potassium ingot with 99.95% purity (Aldrich) for the intercalation. Evaporation of potassium was made until we obtained highly bright golden crystals, as it can be observed in Fig. 4.1. At the end of this process we observed differences in brightness and color on each sample, with the peculiarity that one of them never turned golden. During the whole experiment the system was kept under HV conditions, as well as during the Raman acquisition, which was performed at room temperature with a HORIBA LabRam spectrometer using a 568 nm excitation wavelength, and 0.257 mW of laser power. It is important to mention that once the sample is highly intercalated, the spectra acquisition was performed with very low exposure time to avoid laser induced de-intercalation. The spectra was obtained in a range from 300 cm^{-1} up to 3000 cm^{-1} with the line positions calibrated by gauge lamps.

Results and discussion

On the right side of Fig. 4.1 the four micrographs obtained with an optical microscope (10X resolution), correspond to different defect modulated KC_8 single crystals illustrative for our case of study. The corresponding Raman response is depicted in the left panel of the figure. Four different peaks are observed for the different KC_8 crystals. The first mode is at $\sim$560 cm^{-1}, which has been called $\mathbf{C}_Z$, and involves an out-of-plane motion of the carbon atoms [133]. This mode corresponds to the **M** point of the graphene Brillouin zone, and it becomes Raman active when high intercalation levels are achieved. The next mode is observed around 1140 and 1260 cm^{-1}. This mode appears only in imperfect graphitic structures or at the edge of the sample. Therefore this mode might be related to intrinsic disorder present on the sample, rather than from pristine KC_8. In analogy to the defect modulated double resonance K point phonons, it is tempting to assign it to the **D-line** [74]. This assignment **D** mode is similar to the one in CaC_6 [119, 134], and XC_6 [133] and in doped graphene [132]. However, in our case there is no dispersion of this mode and no peaks were observed in the region of the 2D line for any of our samples. This means that this mode is neither related to the presence of defective non-intercalant graphene layers [132, 197], nor to the D-line in KC_8. Although, these modes are related to defects in the sample, and their exact origin still remains elusive. Finally, we turn to the response of the graphitic **G** mode of KC_8 which we are interested in. It is observed between 1510 and 1566 cm^{-1} and is related to the E_{2g} irreducible representation.

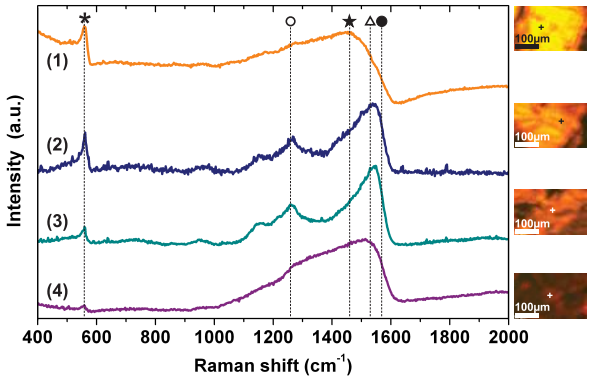

Figure 4.1: Raman spectra of four different defect modulated KC_8 single crystals (labeled 1 to 4 and assigned by their color): (1) highly bright and golden crystal, (2) low bright golden crystal, (3) red crystal, and (4) red to black crystal. The symbols denote: $*$ **C**$_Z$ mode, $\circ$ **D** mode, $\triangle$ E_{2g_1} mode, $\star$ E_{2g_2} mode, and the $\bullet$ **GD** mode explained in the text.

A spectral shape similar to the one depicted in the lower spectrum of Fig. 4.1 was reported in 1979 by Eklund and Subbaswamy [130], which was attributed to the graphite Γ point stage one in XC_8 (X = K, Rb or Cs) with E_{2g} symmetry (at around 1547 cm^{-1} for KC_8). As clearly observed, this mode has a broad Breit-Wigner-Fano lineshape. However, as mentioned above, other literature on potassium intercalated HOPG and graphite single crystals have reported significant differences in spectra of the intrinsic **G-line** of KC_8 within a broad range of positions between 1400 cm^{-1} and 1600 cm^{-1} [27, 60, 99, 103]. Additionally, at this point it is worth mentioning that spectra like 2 and 3 in Fig. 4.1, are in turn similar to data reported for CaC_6 by Dean et al. [133], and Mialitsin et al. [134]. These two middle spectra exhibit a **G** peak, which splits into two peaks: at around 1602 cm^{-1} (up-shifted) and 1571 cm^{-1} (down-shifted). On the other hand, looking closer at the topmost and bottom spectra, at first they look somehow similar but shifted compared to each other. In order to extract the position and line width as well as EPC of KC_8 in these previous studies, a line shape analysis using a Breit Wigner Fano (BWF) line (Eq. 4.3) was performed, because it considers coupling and interference between the phonon mode and an electronic continuum [179].

$$I(w) = I_0 \frac{(1+\frac{w-w_{ph}}{q\Gamma/2})^2}{1+(\frac{w-w_{ph}}{\Gamma/2})^2} + A \tag{4.1}$$

Using this equation the asymmetry of the Raman response is given as (1/q), the center frequency is ω_{ph} and the full width at half maximum (FWHM) is Γ. This fit of nominal KC_8 phases lead to peak positions at 1522 cm^{-1}, 1547 cm^{-1}, or 1510 cm^{-1}; line widths of 157 cm^{-1}, 78.7 cm^{-1}, or 45 cm^{-1}; and asymmetry parameters between -0.8 and -1.8, respectively [60, 103, 130]. A similar fit on our spectra was performed, and the topmost and lowest curve can be simulated with the same parameter sets. However, we observe an additional fine structure in the **G-line** response which is not reproduced using only one BWF line. Previously, the presence of a fine structure and correspondingly more than one component has been reported only for CaC_6 by Dean at al. [133], and Mialitsin et al. [134]. They attributed the different spectral features observed, to surface de-intercalation and to defect modulation within the different positions on their samples.

Therefore, more than one component are also present in our different defect modulated KC_8 single crystals and their relative intensity gives rise to the different line shapes. In the following, we describe how our fit using four components allow us to unravel the real finger print of KC_8. The fit was performed in a region between 1200 cm^{-1} and 1800 cm^{-1} using the same values in position (ω_{ph}), FWHM (Γ), and **q** but different relative intensities in every KC_8 single crystal analyzed. The results for the four different defect modulated KC_8 single crystals are shown in Fig. 4.2 together with the individual components of the fit. The results are also summarized in Table 1.

The first two components labeled **D** and **GD** (blue lines in the figure) are Lorentzian (limit in the BWF equation of $1/q = 0$). Both share the same width (Γ), and are attributed to disorder induced bands, respectively [134]. The other two modes are related to Raman active from the GIC ($\mathbf{E}_{2g_1}$ and $\mathbf{E}_{2g_2}$) with a strong Fano behavior. The Raman spectrum of the "highly bright golden" crystal in Fig. 4.2 a), shows a high and broad Breit Wigner Fano peak around 1510 cm^{-1} ($\mathbf{E}_{2g_2}$), as the biggest contribution to the **G-line** response. The $\mathbf{E}_{2g_1}$ mode at $\sim$1547 cm^{-1} is only present as small contribution, and the two defect modulated **D** and **GD** components are observed as very weak Lorentzian around $\sim$1260 cm^{-1}, and $\sim$1563 cm^{-1}. Analyzing the "red" and "low bright golden" crystals Fig. 4.2 b) and c), we clearly observe an increase of the **GD** and **D** components, with again almost the same intensity each. Likewise, the E_{2g_1} at $\sim$1547 cm^{-1} mode increases, yielding the highest relative intensity, as the E_{2g_2} component at $\sim$ 1510 cm^{-1} decreases and almost vanishes in Fig.4.2 c). Regarding the last curve in Fig.4.2 d), which corresponds to the "red to black" crystal, we notice the complete disappearance of the $\sim$1510 cm^{-1} $\mathbf{E}_{2g_2}$ mode, and the E_{2g_1} at $\sim$1547 cm^{-1} remains as the as the strongest component. Consistently, the defective modes where conserved, and an extra $\sim$1420 cm^{-1} mode appear, which we attribute to additional intrinsic defects on the sample, as it has a Lorentzian shape.

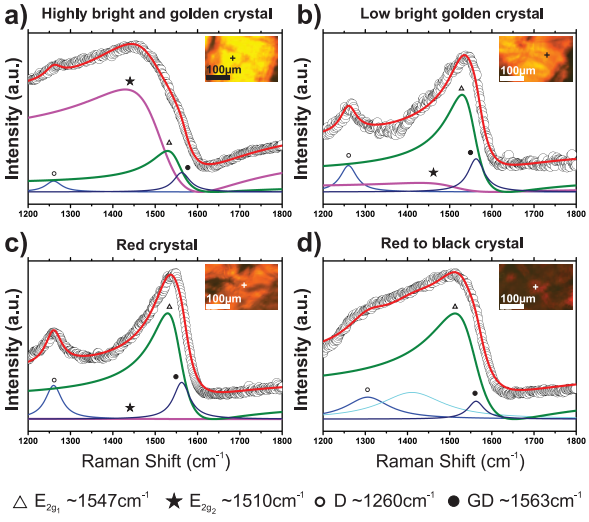

Figure 4.2: Detailed line shape analysis of the Raman spectra in the range of the graphitic mode for the four different defect modulated KC_8 single crystals shown in Fig. 1 (crystal 1 panel a), crystal 2, panel b), crystal 3, panel c), crystal 4, panel d)). The solid lines represent fits with Breit Wigner Fano lines corresponding to the **D** and **GD** modes (blue curve), the $\mathbf{E}_{2g_1}$ mode (green curve) and $\mathbf{E}_{2g_2}$ mode (pink curve), explained in the text.

In order to correlate the presence of disorder and/or incomplete intercalation with respect to the most prominent Raman mode, and determine the finger print of KC_8, we compared our results of the individual components to the intensity of the C_Z mode which is only allowed for

KC_8. Interestingly, this correlation is in agreement to what is recently reported for doping in graphene [132] where the intensity of the $\mathbf{C}_Z$ mode increases with increasing the potassium content. Therefore, one way to correlate the crystal quality and intrinsic doping level to the intrinsic **G-line** Raman response of KC_8 is comparing the relative intensity (RI) of the individual components to the intensity of the $\mathbf{C}_Z$ mode using a BWF lineshape. The results are summarized in Table 1 and regarding the relative intensities in Fig. 4.3.

Table 4.1.: Breit-Wigner-Fano fit parameters to Raman KC_8

Peak	Γ	q	ω_{ph}	RI(1)	RI(2)	RI(3)	RI(4)
C_Z	19.91	-2.31	561	0.705	0.543	0.185	0.096
D	47.06	$1E^{+5}$	1260	0.194	0.326	0.383	0.276
G	47.06	$1E^{+5}$	1562	0.345	0.410	0.417	0.225
E_{2g_2}	176.7	-1.09	1510	1.000	0.060	0.001	-
E_{2g_1}	82.56	-2.21	1547	0.609	1.000	1.000	1.000

The results for all four crystals are fully consistent. The appearance of a **D** and **GD** mode is the result of a defective crystal, and it increases as the sample has more defects [119, 134]. Therefore the **D** to **GD** ratio is roughly constant as expected since they have the same origin. On the other hand, as depicted in Fig. 4.3 the relative intensity of $\mathbf{C}_Z$ mode shows a monotonic decrease as the sample quality gets worse (Fig. 4.3 a) upper panel). The same holds for the $\mathbf{C}_Z$ over E_{2g_1} ratio (Fig. 4.3 a) lower panel). This highlights that these two components belong to the same intrinsic phase. In addition, when analyzing the area percentage per component shown in Fig. 4.3 b) there is a decrement in the area of the E_{2g_2} mode as the sample get worse (higher **D** and **GD** modes), and the opposite with respect to the E_{2g_1} one. Hence, we have a sound evidence that the 560 cm^{-1} component is correlated with the highly intercalation stage on KC_8, and its highest contribution appear when the zone of study is the brightest, the crystal is golden, and the defect related modes are vanishingly small. Consequently, we can safely assign the intrinsic **G-line** of KC_8 to a BWF line with a position around 1510 cm^{-1}. Interestingly this is similar to the position observed for BaC_6, SrC_6, YbC_6, CaC_6 in [133], and close to those RbC_8 [103] and CsC_8 [60]. This indicates a common trend in the **G-line** positions in stage one n-type GIC, and highlights that the spread of frequencies between the different GIC is much less than previously reported and estimated.

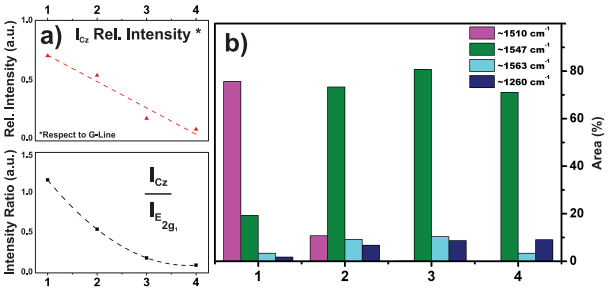

Figure 4.3: Statistical data analysis of the 4 different defect modulated KC_8 single crystals. a) Relative Intensity of the $\mathbf{C}_Z$ mode respect to the quality of the sample with a monotonic decrease. This also counts for the ratio of $I_{C_Z}/I_{E_{2g_1}}$. b) corresponding relative area (%) from each component.

Once the intrinsic **G-line** of KC_8 has been assigned to the E_{2g_2} mode with a position ω_{ph} and

a FWHM Γ, it is interesting to analyze it with respect to the EPC constant responsible for the superconductivity within the BCS theory. In a recent paper, Saitta et al. [103] have analyzed the EPC in many different stage one GIC. They evaluated the EPC from a difference in the experimental phonon frequency to the calculated phonon frequency in the adiabatic and non-adiabatic limit ω_A, ω_{NA}. For KC_8 they were calculated as ω_A= 1223 cm^{-1}, ω_{NA}= 1534 cm^{-1}, respectively [103]. In order to determine the electron phonon scattering renormalized line-width γ^{EPC} we used Dean et al. [133] rearrangement of the formalism of Saitta et al. yielding:

$$\frac{\gamma^{EPC}}{2} = \sqrt{(\omega_{ph} - \omega_A)(\omega_{NA} - \omega_{ph})} \tag{4.2}$$

We get a $\gamma^{EPC} \simeq 166$ cm^{-1} which is in very good agreement to our experimental value of $\Gamma = 176.7$ cm^{-1} obtained from our BWF fit. In comparison to the calculated $\gamma^{EPC} = 120$ cm^{-1} reported for KC_8 by Saitta et al. [103], this is in better agreement to the experimental value. This highlights that similar to MgB_2 also for KC_8 the phonon decay channel into dressed electron -hole pairs is the dominant one [103].

4.2. Raman response of stage-1 graphite intercalation compounds revisited

Published in: Physical Review B, **86**, 075406 (2012) doi: 10.1103/PhysRevB.86.075406 [57]

An in-situ Raman analysis of *stage-1* KC_8, CaC_6, and LiC_6 graphite intercalation compounds (GIC) to unravel intrinsic finger print, and the relation of the optical allowed vibrations to the superconductivity coupling in GICs was performed. Four main components were found between 1200 cm^{-1} and 1700 cm^{-1}, and each of them were assigned to a corresponding vibrational mode. From a detailed line shape analysis of the intrinsic Fano-lines of the G- and D-line response we precisely determine the position (ω_{ph}), line width (Γ_{ph}) and asymmetry (q) from each component. The comparison to the theoretical calculated line width and position of each component allow us to extract the electron-phonon coupling constant of these compounds, which highlighted that Raman active modes alone are not sufficient to explain the superconductivity within the electron-phonon coupling mechanism in CaC_6 and KC_8.

The synthesis of KC_8 was performed in-situ under high vacuum ($\sim$4x10^{-8} mbar) conditions in a quartz tube with natural graphite flake single crystals from different sources, and a potassium ingot with 99.95% purity (Aldrich) for the intercalation. Potassium was evaporated until golden crystals were obtained. This phase can be directly assigned to *stage-1* KC_8 phase from a comparison of the Raman response with previous combined Raman and XRD results [99, 135]. CaC_6, and LiC_6 were prepared in a sealed ampoule by using a procedure described elsewhere [28]. Highly oriented pirolytic graphite (HOPG) flakes were degassed and used for lithium and calcium intercalation for 10 days under He atmosphere (ca. 0.5 atm). The ampoule was then opened in the glove box and gold colored product was extracted from the melt. Powder x-ray diffraction measurements were carried out using a Stadi-P diffractometer (CuK_a) to confirm the intercalation stage in CaC_6 and LiC_6. For the Raman analysis every GIC was kept in vacuum ($\sim$4x10^{-8} mbar) in order to avoid de-intercalation due to exposure to air. The Raman analysis, was performed with a HORIBA LabRam at room temperature, with a 568 nm wave length, and 0.25 mW of laser power. Every spectrum were acquired under the same conditions in a range from 500 cm^{-1} up to 2500 cm^{-1} and the line positions were calibrated by gauge lamps.

Results and discussion

In the Raman response of *stage-1* GIC eight optical vibrational modes are present [99] in the following irreducible representation:

$$\Gamma = 2A_{2u} + 2B_{2g} + 2E_{1u} + 2E_{2g}$$

The $E_{2_{g_1}}$, and the $E_{2_{g_2}}$ vibrational modes are Raman active, and the A_{2u}, and E_{1u} belong to infra-red active modes [27, 60]. There are some other modes in graphite which are forbidden in perfect graphite and only become active in the presence of disorder like the mode with A_{1g} symmetry. In Fig. 4.4 a), the optical modes of graphite are depicted. Previous Raman studies in GIC have confirmed the presence of the E_{2g} mode around 1600 cm^{-1}, the A_{2u} (*c-axis* mode) around 500 cm^{-1}, and the absence of the A_{1g} [27, 99]. The *c-axis* mode has being attributed to an

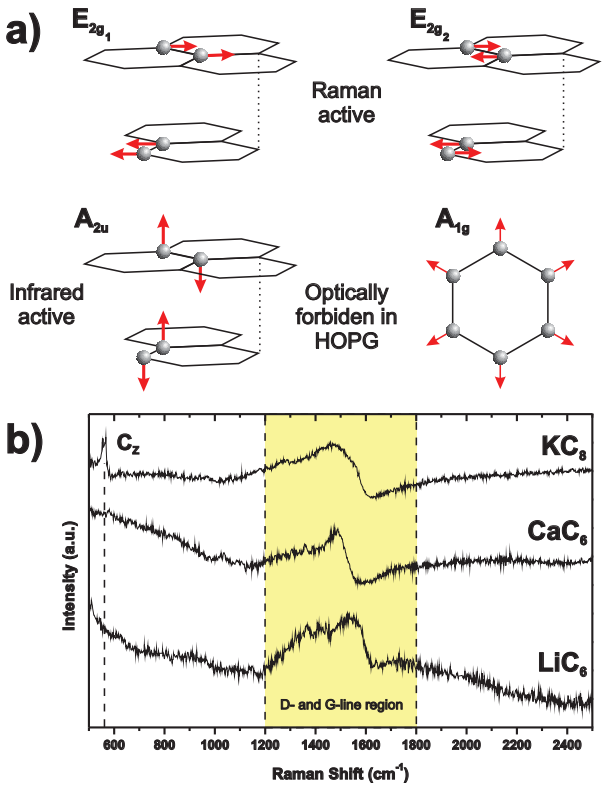

Figure 4.4: a) Optical modes of graphite. b) Raman spectra from KC_8, CaC_6, and LiC_6 taken with 568 nm laser at room temperature and low laser power of 0.25 mW.

out-of-plane C motion in graphite [133]. This mode correspond to the **M** point of the graphene Brillouin zone, and it becomes Raman active when high intercalation levels are achieved. In agreement with the literature, we observe (as shown in in Fig. 4.4 b), that the *c-axis* mode is present solely in KC_8 around $\sim$560 cm^{-1}. Surprisingly and in agreement with previous studies neither in CaC_6, nor in LiC_6 this mode is observed [119, 198].

Regarding the G-line response all these previous studies reported one G-line which has a strong Fano line shape due to the coupling and the interference with the conduction electrons. Taking a closer look on the lineshape of the G-line response in Fig. 4.4 b), one can easily see that more than one component is present, and a detailed line shape analysis is needed in order to unravel their intrinsic response and related electron phonon coupling of these *stage-1* GIC. The line-shape analysis of the G-line is discussed in detail below.

Analysis of the intrinsic G-line response of *Stage-1* GIC

The structure of the intercalation stages in graphitic compounds, has been studied and it is well understood from x-ray diffraction [99]. However, the intrinsic Raman response of *stage-1* GIC is still complicated by laser induced de-intercalation from a local heating of the sample with different laser power densities [60]. In addition, other factors such as 3D intrinsic disorder of the crystal also strongly affect the Raman response in GIC. For example, a graphite single crystal doped to *stage-1* will remain polycrystalline due to a non-homogeneous intercalation. This will limit the achievable doping in these GIC [85, 133].

Hence, the previous experimental and theoretical results on the Raman response of KC_8 and

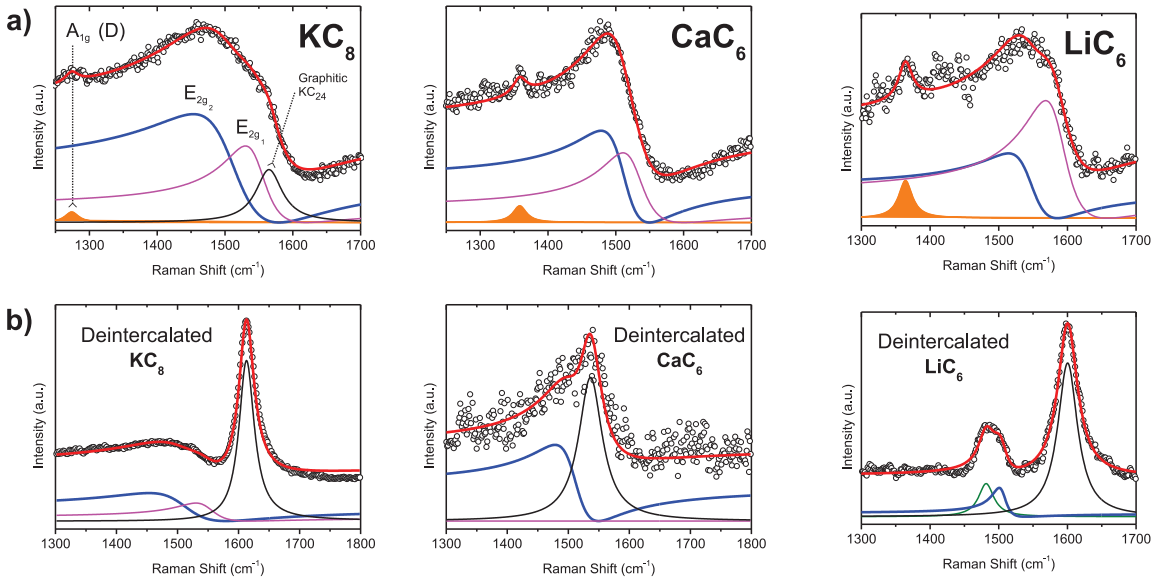

Figure 4.5.: D- and G-line analysis for *stage-1* GIC, and Raman response of their laser induced deintercalated phases. The four components which can be identified in the G-line shape are: $\mathbf{A}_{1g}$ mode between 1250 and 1350 cm^{-1}, $\mathbf{E}_{2g_2}$ mode ∼1510 cm^{-1}, $\mathbf{E}_{2g_1}$ mode at ∼1547 cm^{-1} , and *stage-2* G-mode ∼1560 cm^{-1}. In the upper panel **a)** we can observe that KC_8 exhibit a strong contribution from the $\mathbf{E}_{2g_2}$ with a broad Fano behavior, which is the finger print for the intrinsic line of *stage-1* compound [135]. In the lower panel **b)** we present the same crystals analyzed in the upper panel but de-intercalated. We can clearly observe the decrease of the $\mathbf{E}_{2g_2}$ mode, concomitant to a strong increase of the G-mode assigned to the XC_{24} graphitic face ∼1600 cm^{-1}.

CaC_6 reported in the literature are not conclusive with respect to the G-line shape and position. In different studies a wide range of different G-line positions between ∼1400 cm^{-1} and ∼1600 cm^{-1} are reported: i.e. at ∼1500 cm^{-1} [27], between 1400 cm^{-1} and 1550 cm^{-1} [99], 1534 cm^{-1} [103], 1547 cm^{-1} [60], 1420 cm^{-1} and 1582 cm^{-1} [130]. In more recent experiments for calcium GIC [133, 134], potassium doped graphene and graphite [85, 135], and later in Li-graphite [198], the strongest G-line phonon response is observed around 1510 cm^{-1} when the sample has the best quality (lowest defect content) and highest intercalation.

In Fig. 4.5 a) the D- to G-band region of pristine *stage-1* intercalation compounds with K, Ca, and Li is depicted and clearly shows the presence of shoulders in the response, which indicate different components. Nevertheless, in order to compare with the previous studies [60, 103, 130] we first conducted a line-shape analysis of the G-line by using a single Breit Wigner Fano (BWF) function. This yields parameters which are in good agreement to those results, and confirms that our samples have the same high quality of a true *stage-1* compound. This is further supported by the fact that the G-line assigned to *stage-2* compounds around 1600 cm^{-1} is only increased upon e.g. laser induced de-intercalation (see Fig. 4.5 b).

In a second step a detailed and accurate analysis of the line-shape in the D- to G-band region of these GIC was conducted using four components. The assignment of each component to the

A_{1g}(D), E_{2g_2}, E_{2g_1} modes, and the G-line of the *stage-2* compound is explained in the following.

Regarding the line-shape, all components have been fitted using BWF functions of the form:

$$I(w) = I_0 \frac{(1+\frac{w-w_{ph}}{q\,\Gamma/2})^2}{1+(\frac{w-w_{ph}}{\Gamma/2})^2} + A$$

where ω_{ph} is the phonon frequency, Γ the line width or damping, **q** the asymmetry parameter and A an offset. For the first and fourth peak (D, and G), the asymmetry was **q**=10^5 approaching a Lorentzian function, while the second and third (splitted G-line) have a pronounced Fano interference. In the analysis, in order to get comparable results for each GIC, the same values of Γ, and **q** were used to fit each respective component. The parameters are summarized in Table I together with the calculated values from the adiabatic and non-adiabatic phonons from Ref. [103].

The first mode observed in Fig. 4.5 a) between 1260 and 1360 cm^{-1} has been previously attributed to particle size effects and/or the presence of disorder [199, 200]. It has been assigned to the A_{1g} vibration, which is forbidden in perfect graphite. Therefore, this mode is called D-line (intrinsic "defect mediated"), and it involves the contribution from the phonons near the *K* zone boundary with a Lorentzian line-shape.

The second and third modes observed are assigned to the E_{2g} graphitic mode of heavily doped graphene layers (Fig. 4.5 a). Both components have a pronounced asymmetry and they are well described by a BWF line-shape. We label the two modes as E_{2g_1} and E_{2g_2}. The E_{2g_1} mode is located between 1528 cm^{-1} and 1585 cm^{-1} and it is attributed to not homogeneous or incomplete intercalation in *stage-1* compounds [135]. The E_{2g_2} mode locates at 1510 cm^{-1} for KC_8 and CaC_6, and 1546 cm^{-1} for LiC_6. It has a clear and strong Fano behavior which is characteristic to the finger print of *stage-1* graphite intercalation compounds [133, 135]. When de-intercalation was induced in the samples, a decrease of these E_{2g} modes was remarkably observed (see Fig. 4.5 b).

The fourth mode related to the G-line of their respective *stage-2* compound is observed at 1612 cm^{-1} for KC_8, 1600 cm^{-1} for LiC_6 and at 1560 cm^{-1} for CaC_6. The surprising low frequency in the case of CaC_6 was also found in Ref. [134] and explained as a de-intercalated phase in CaC_6. As mentioned above, the increase of this fourth component is highlighted in the partly de-intercalated *stage-1* compounds in Fig. 4.5 b), and points towards a phase separation upon de-intercalation.

Analysis of the Electron-Phonon Coupling

The previous results are very important for the correct determination of the stage, and electron-phonon coupling constant λ_{ph} responsible for superconductivity within the BCS theory [103, 133, 201]. This constant is directly related to the intrinsic G-line phonon frequency, and to the adiabatic (ω_A) and non-adiabatic (ω_{NA}) phonon frequencies. Saitta et al. [103] have analyzed the EPC in many different *stage-1* GIC from a difference in the experimental phonon frequency to

Table 4.2.: Fit parameters to the four components of the D- and G-line in the Raman spectra of KC_8, CaC_6, and LiC_6.

KC_8	$\omega_{ph}(cm^{-1})$	$\Gamma_{ph}(cm^{-1})$	q	$\omega_A{}^{(1)}$	$\omega_{NA}{}^{(2)}$
D	1274	24.3	10^5	-	-
E_{2g_2}	1510	125.6	-1.09	1223	1534
E_{2g_1}	1547	70.9	-2.02	1223	1534
$\mathbf{G}^{(3)}$	1565	47.0	10^5	-	-

CaC_6	$\omega_{ph}(cm^{-1})$	$\Gamma_{ph}(cm^{-1})$	q	$\omega_A{}^{(1)}$	$\omega_{NA}{}^{(2)}$
D	1358	24.3	10^5	-	-
E_{2g_2}	1510	71.0	-1.09	1446	1529
E_{2g_1}	1528	70.9	-2.02	1446	1529

LiC_6	$\omega_{ph}(cm^{-1})$	$\Gamma_{ph}(cm^{-1})$	q	$\omega_A{}^{(1)}$	$\omega_{NA}{}^{(2)}$
D	1364	24.3	10^5	-	-
E_{2g_2}	1546	71.0	-1.09	1362	1580
E_{2g_1}	1585	70.9	-2.02	1362	1580

[1] Calculated Adiabatic E_{2g} phonon frequencies Ref. [103] in cm^{-1}.
[2] Calculated Non-adiabatic E_{2g} phonon frequencies Ref. [103] in cm^{-1}.
[3] G-line contribution from KC_{24} *stage-2* compound.

the calculated phonon frequency in the adiabatic and non-adiabatic limit. In order to determine the electron phonon scattering renormalized line width γ^{EPC} [103, 133] we used:

$$\frac{\gamma^{EPC}}{2} = \sqrt{(\omega_{ph} - \omega_A)(\omega_{NA} - \omega_{ph})} \tag{4.3}$$

We obtain γ^{EPC} values for KC_8, CaC_6, and LiC_6 which are in very good agreement to our experimental Γ_{ph} value obtained from our BWF fit, Table II. In Fig. 4.6 we show the location of our γ^{EPC} with respect to the expected linear tendency to Γ_{ph} as predicted by Saitta et al. [103]. It is important to notice that some components of the G-line in KC_8, CaC_6, and LiC_6 bring a $\gamma^{EPC} = 0$, which means that they do not show the non-adiabatic effects for layered metals and therefore they do not contribute to the electron-phonon coupling constant λ_{ph}. In comparison to the experimental Γ^{exp} and γ^{EPC} from Ref. [83, 119, 202] (Fig. 4.6 $\star$), our results using the E_{2g_2} mode are in better agreement to the linear trend expected for $\Gamma \approx \gamma^{EPC}$. This confirms the importance of every optical mode in the range between the adiabatic and non-adiabatic frequency range (ω_A-ω_{NA}), and confirms that the E_{2g_2} component is the intrinsic *stage-1* vibrational mode with the strongest non-adiabatic effect on the EPC.

We now turn to a detailed analysis of the EPC constant λ_{ph}. Different values have been already reported and used to calculate the critical temperature of KC_8, CaC_6, and LiC_6 with values

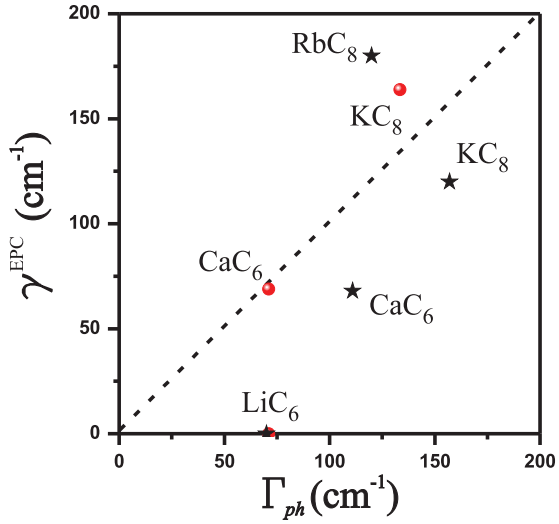

Figure 4.6: Calculated γ^{EPC} (Eq. 4.3) for different GIC as function of their width Γ_{ph}. Black stars ($\star$) correspond to experimental values from Ref. [83, 119, 202]. The dashed line represents the approximation of $\Gamma_{ph} \approx \gamma^{EPC}$. The red dots show our calculated EPC, which are in better agreement to the expected approximation to the Γ_{ph} values.

around 5 K, 11.5 K, and 0.9 K, respectively, in agreement with some experimental and theoretical studies [62, 192]. In order to extract λ_{ph} from the phonon line-width (Γ) and position (ω_{ph}) from our Raman data we used [203]:

$$\lambda_{\Gamma,K} = \frac{A_{uc}\, F^2_{\Gamma,K}}{2\, M\, \omega_{\Gamma,K}\, v_F^2} \tag{4.4}$$

where the electron-phonon coupling strength is given by D_{exp} :

$$\Delta\Gamma_G = \frac{A_{uc}\, D^2_{exp}}{8\, M\, v_F^2} \tag{4.5}$$

and A_{uc} is defined as the area of the graphene unit cell, M is the carbon atom mass, v_F is the Fermi velocity, $\Delta\Gamma_G$ is the Landau damping phonon decay rate given by $\Delta\Gamma_G = \Gamma_{ph} - \Gamma_{Graphite}$, and $F^2_{\Gamma,K}$ has dimensionality of a force taking in consideration the lattice displacement along the corresponding optical phonon mode. By using Eq. 4.4 and the definition of $F^2_{\Gamma} = 4\langle D^2_{\Gamma}\rangle_F$, and $F^2_{K} = 2\langle D^2_{K}\rangle_F$ from Ref. [185, 203] we calculate the values for $\lambda_{\Gamma,K}$ for each phonon in the Γ-K branch observed in the G-line region as summarized in the right column of Table II. $\langle D^2_{\Gamma,K}\rangle_F$ were taken from the DFT$_{GGA}$ calculations in Graphite [185] as they are closer to our electron-phonon coupling strength (D_{exp}).

By using the averaged electron-phonon coupling constant $\lambda_{ph} = \lambda_{\Gamma} + \lambda_{K}$, and the position ω_{ph} from the strongest optical mode in KC_8, CaC_6, and LiC_6 one can estimate the critical temperature T_c using McMillan's formula [204]. Taking our ω_{ph} values converted in to phonon temperature Θ, $\mu^* \approx 0.14$ from [205], and λ_{ph} from the Raman analysis, we obtain $\lambda_{ph} < 0.06$ values, which are too low to explain superconductivity within EPC mechanism using these high-frequency Raman active modes.

However, this is not a general behavior in intercalation compounds. Electron-phonon studies in alkali-intercalated fullerenes showed the possibility to attribute the strongest λ_{ph} contribution for superconductivity to the Hg(1) mode in A_3C_{60} fullerides [115, 116]. More over, in agreement to the analysis reported by Yao et al. in Ref. [116] our D_{exp} presented the same trend as the one observed in fullerides intercalation compounds. Therefore, we can confirm that the larger the value of $1/\mathbf{q}$, the weaker the coupling strength D_{exp} in GIC and fullerides.

On the other hand, in comparison to the EPC constant λ_{ARPES} reported using an analysis of the self energy results in ARPES [62, 206], our λ_{ph} values are about a factor of 10-15 lower. Since, in the case of CaC_6 superconductivity was confirmed at T_c=11.5 K, only the λ_{ARPES} [206] would be sufficient to explain this high superconducting transition temperature. Hence, the low λ_{ph} proves that optical modes from the G-line in *stage-1* GIC are not sufficient to explain T_c in the electron-phonon driven superconducting coupling mechanism and additional not optically active modes might play an important role.

Table 4.3.: Electron-phonon coupling parameters from the G-line Raman analysis. The values of ω_{ph}, Γ_{ph}, γ^{EPC} are in cm^{-1} and they were extracted from the BWF analysis of the Raman spectrum. D_{exp} is the electron-phonon coupling strength from Eq. 4.5 in (eV/Å).

KC_8	ω_{ph}	Γ_{ph}	γ^{EPC}	$\gamma^{EPC(1)}$	D_{exp}	$OB^{(2)}$	$\lambda_{K,\Gamma}{}^{(3)}$
D	1274	24.3	230	-	14	K	0.024
E_{2g_2}	1510	125.6	163	157	51	Γ	0.020
E_{2g_1}	1547	70.9	0	-	36	Γ	-
λ_{ph}							0.044

CaC_6	ω_{ph}	Γ_{ph}	γ^{EPC}	$\gamma^{EPC(1)}$	D_{exp}	$OB^{(2)}$	$\lambda_{K,\Gamma}{}^{(3)}$
D	1358	24.3	0	-	14	K	0.022
E_{2g_2}	1510	71.0	68	68	36	Γ	0.020
E_{2g_1}	1525	70.9	34	36	36	Γ	0.019
λ_{ph}							0.061

LiC_6	ω_{ph}	Γ_{ph}	γ^{EPC}	$\gamma^{EPC(1)}$	D_{exp}	$OB^{(2)}$	$\lambda_{K,\Gamma}{}^{(3)}$
D	1364	24.3	43	-	14	K	0.022
E_{2g_2}	1546	71.0	157	-	36	Γ	0.019
E_{2g_1}	1585	70.9	0	0	36	Γ	-
λ_{ph}							0.041

[1] Calculated phonon full line width at half maximum due to phonon decay in dressed electron-hole pairs γ_{σ}^{EPC} Ref. [103].
[2] Optical branch assignment based in [62, 185].
[3] Electron-phonon coupling constant from Eq. 4.4

4.3. De-intercalation process from Stage-1 to Stage-2 graphite intercalation compounds revisited

Published in: Physica Status Solidi B, **249**, 2640 (2012) doi: 10.1002/pssb.201200174 [195]

In-situ laser induced de-intercalation was performed obtaining their corresponding *Stage-2* GIC system. Our main focus is to unravel the intrinsic de-intercalation process due to the changes in the graphitic G-line phonon modes between those two systems performing a detailed line-shape analysis. This analysis yields as a convenient reference system to assure a proper determination of the intrinsic *Stage-1* and *Stage-2* compounds.

Three main GIC were synthesized for this study. CaC_6, and LiC_6 where prepared in a sealed ampule by using a modified procedure described elsewhere [28]. Degassed highly oriented pirolytic graphite (HOPG) flakes were used for lithium and calcium intercalation for 10 days under He atmosphere (ca. 0.5 atm). The ampoule was then opened in the glove box and the gold colored product was extracted from the melt. Powder x-ray diffraction measurements were carried out using a Stadi-P diffractometer (CuK_a) to confirm the intercalation stage in CaC_6 and LiC_6. KC_8 compound was synthesized in-situ under high vacuum ($4x10^{-8}$ mbar) in a quartz tube. Natural graphite single crystal flakes from different sources were used. Golden graphite crystals were obtained from the evaporation of potassium (99.95% Aldrich), which depicts the intrinsic KC_8 phase in potassium compounds [135]. For the Raman analysis every GIC was kept in vacuum (ca. 10^{-8} mbar) in order to avoid de-intercalation due to exposure to air. The spectrum acquisition was performed with a HORIBA LabRam at room temperature by using a 568 nm wave length in a range from 300 cm^{-1} up to 2800 cm^{-1}, and the line positions were calibrated by calibration lamps. Laser powers of 0.25 mW and 8.5 mW were used for spectrum acquisition and de-intercalation, respectively.

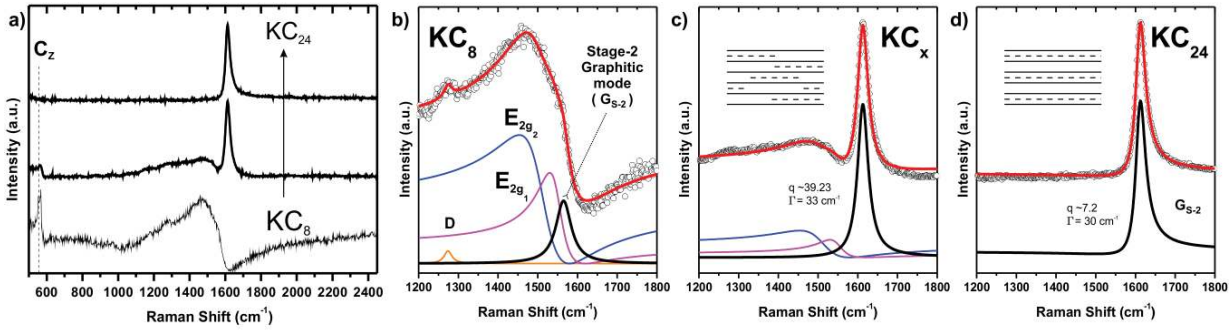

Figure 4.7.: a) Raman spectra of the de-intercalation process from *Stage-1* KC_8 to *Stage-2* KC_{24} is presented. A clear vanishing of the C_z mode at 500 cm^{-1} and change in the G-line shape as function of de-intercalation is observed. The detailed line-shape analysis of the three phases KC_8 b), KC_x c), and KC_{24} d) revealed the strongest components of the G-line at 1510 cm^{-1}, and 1610 cm^{-1} as well as intermediate components. The intermediate phase between KC_8 and KC_{24} in c) is a superposition of *Stage-1* and *Stage-2* components.

Results and discussion

In Fig. 4.7 a) the process of de-intercalation from KC_8 to KC_{24} is shown. Two parameters are important to consider in this process, the presence of the C_z mode around 500 cm^{-1}, which confirms the *Stage-1* assignment, and the frequency of the strongest G-line mode. When analyzing the C_z mode from the Raman spectra in Fig. 4.7 a), we clearly observe the presence of this mode in KC_8 as well as in the de-intercalated middle phase between KC_8 and KC_{24}. This indicates that this mode alone is not enough to determine the correct staging assignment. The G-line Raman response from the different intercalation phases observed was then studied in a range from 1200 cm^{-1} to 1800 cm^{-1} Fig. 4.7 (b-d). For comparison with previous studies, we first perform a line-shape analysis of the G-line by using a single Breit-Wigner-Fano (BWF) function. The parameters from this first analysis are in good agreement to those reported in different publications concerning the electronic continuum states in KC_8, and KC_{24} [60, 103, 130]. However, this is not sufficient to yield complete information on the intrinsic line-shape of KC_8 [135], and and for the Response at intermediate de-intercalation (see Fig. 4.7 b,c). Therefore, we conducted a detailed and accurate analysis of the line-shape by introducing four components named as: **D**, E_{2g_2}, E_{2g_1}, and $\mathbf{G}_{S-2}$. Each individual component was fitted by using a BWF function, and the parameters used will be explained below and summarized in Table 4.4.

Table 4.4.: Fit parameters used in the D- to G-line Raman region for KC_8, CaC_6, and LiC_6 and their de-intercalated phases. The values of position (ω_{ph}), and FWHM (Γ_{ph}) are in units of cm^{-1}.

	KC_8			**KC_x**			**KC_{24}**			**CaC_6**			**CaC_x**			**LiC_6**			**LiC_x**		
	ω_{ph}	Γ_{ph}	**q**	ω_{ph}	Γ_{ph}	**q**	ω_{ph}	Γ_{ph}	**q**	ω_{ph}	Γ_{ph}	**q**	ω_{ph}	Γ_{ph}	**q**	ω_{ph}	Γ_{ph}	**q**	ω_{ph}	Γ_{ph}	**q**
D	1274	24	10^5	-	-	-	-	-	-	1358	24	10^5	-	-	-	1364	24	10^5	1481	27	10^5
E_{2g_2}	1510	125	-1.09	1510	125	-1.09	-	-	-	1510	71	-1.09	-	-	-	1546	71	-1.09	-	-	-
E_{2g_1}	1547	70	-2.02	1547	70	-2.02	-	-	-	1528	70	-2.02	-	-	-	1585	70	-2.02	1505	24	-2.77
$\mathbf{G}_{S-2}$	1565	47	10^5	1612	33	39.23	1610	30	7.28	-	-	-	1600	49.5	10^5	-	-	-	1600	35	10^5

In the case of heavily doped GIC, the intrinsic G-line is assigned to the E_{2g} mode with a broad BWF line-shape and strong asymmetry. In the case of KC_8 (Fig.4.7 b) we observed the E_{2g_1} mode at $\sim$1547 cm^{-1}, which is attributed to not homogeneous, de-intercalated or not complete intercalation in *Stage-1* compounds [135] with asymmetry **q**=-2.02. The E_{2g_2} mode locates at 1510 cm^{-1} with clear and strong Fano behavior (**q**=-1.09 and Γ=125 cm^{-1} see Table 4.4) characteristic to the finger print of *Stage-1* graphite intercalation compounds [85, 133, 135]. The **D** mode at 1274 cm^{-1} is attributed to intrinsic defects on the edges and/or the presence of disorder due to high intercalation [199, 200]. The last mode $\mathbf{G}_{S-2}$ in Fig.4.7 b) places at 1565 cm^{-1}. The importance of this mode shows up when analyzing its behavior as function of de-intercalation. In Fig.4.7 c) an intermediate phase between KC_8 and KC_{24} is shown. This intermediate phase reveals a clear superposition of the intrinsic KC_8 and KC_{24} modes, which confirms the contribution of each component to their corresponding phase. The position of the $\mathbf{G}_{S-2}$ mode in Fig.4.7 d) remains constant at 1610 cm^{-1} with FWHM $\Gamma \simeq 30$ cm^{-1}, which depicts the intrinsic *Stage-2* compound line-shape in agreement to experimental results previously reported [57, 99, 103]. The asymmetry observed **q**=7.2 of this $\mathbf{G}_{S-2}$ mode, reveals the interaction between the intercalant and the graphitic layers in KC_{24}.

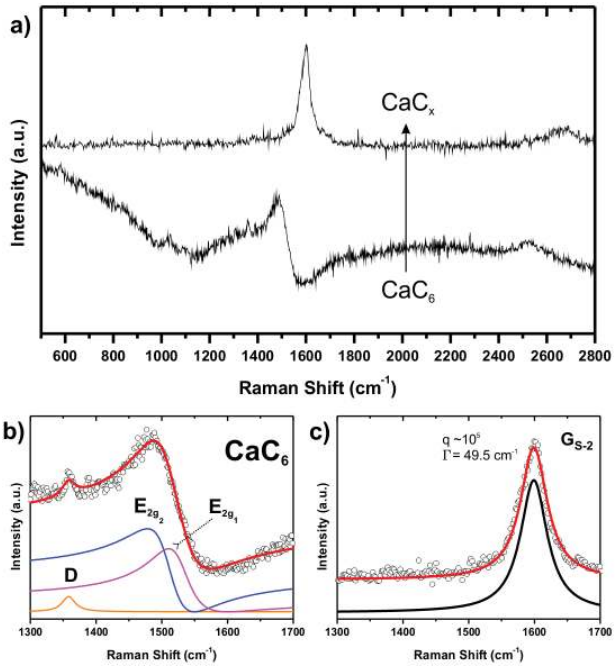

Figure 4.8: The upper panel a) shows a wide range Raman spectrum of CaC_6 and its de-intercalated *Stage-2* phase. In panel b), a detailed G-line analysis revealed the strongest $\mathbf{E}_{2g_2}$ Fano mode at 1510 cm^{-1}. The right panel c) presents the intrinsic *Stage-2* mode ($\mathbf{G}_{S-2}$) at 1600 cm^{-1}, which confirms de-intercalation.

Turning to the analysis of graphitic calcium compounds depicted in Fig. 4.8. In Fig. 4.8 a) we show the change in the Raman response from *Stage-1* CaC_6 to a de-intercalated calcium phase, which matches the line-position of *Stage-2* in potassium GICs. Again we performed a detailed line-shape analysis which revealed the strongest Fano mode at 1510 cm^{-1}, labeled as E_{2g_2}, with FWHM Γ=70.9 cm^{-1} and complete absence of the graphitic *Stage-2* phase in CaC_6 (Fig. 4.8 b and Table 4.4). The origin of the E_{2g} mode in CaC_6 compounds was studied by Hlinka et al. in Ref. [119], and attributed to the bond-stretching mode in this GIC. In addition, they observed a weak second order Raman mode around 2500 cm^{-1} for CaC_6 which is associated to high doping in calcium compounds. This mode is also in good agreement with our results depicted in Fig. 4.8 a). When de-intercalation was induced, the Fano E_{2g} components of CaC_6 vanished and a G-line around 1600 cm^{-1} shows up. The fitting parameters of this mode are in close agreement to the ones of KC_{24} with ω_{ph}=1600 cm^{-1}, and Γ=49.5cm^{-1}. The structure and electron concentration of KC_{24} is not the same as the one of this CaC_x compounds, but as their line-shape and position closely resemble each other we assign this stage as *Stage-2* in calcium GICs.

In comparison, the de-intercalation analysis made for LiC_6 depicted in Fig. 4.9, revealed similarities in the shape but differences especially in the phonon frequencies respective to potassium and calcium intercalation. The *Stage-1* LiC_6 shows in agreement with Ref. [207] two E_{2g} components with the strongest mode with a the most pronounced Fano character at 1585 cm^{-1} (see Fig. 4.9 b and Table 4.4). As function of de-intercalation, these Fano modes tends to decrease in intensity and the $\mathbf{G}_{S-2}$ component show up at 1600 cm^{-1} (Fig. 4.9 c) with a line-width of 35 cm^{-1}. This is in agreement with results regarding to Li intercalation induced by gate voltage [207], and Li-graphite stage dependence [198], where $\omega_{ph} \simeq$1600 cm^{-1} and $\Gamma \simeq$33 cm^{-1} were reported for LiC_{17} *Stage-2*. Since these results are close to the position and

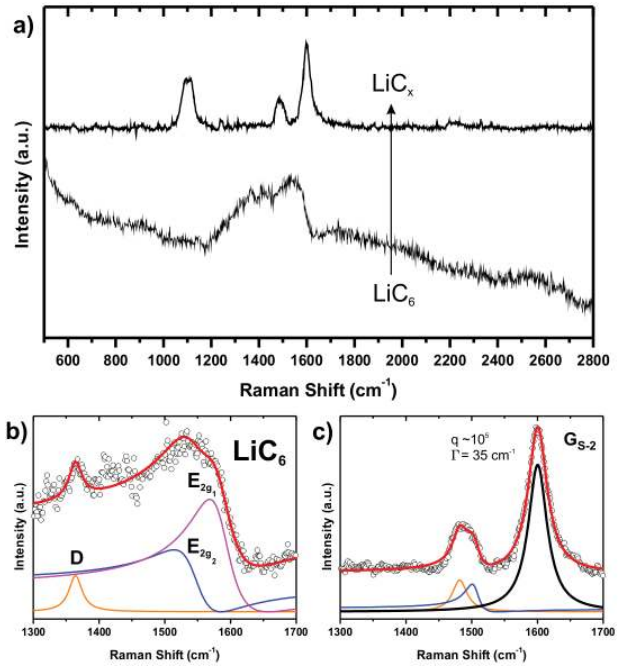

Figure 4.9: Panel a) presents a wide range Raman spectrum of LiC_6 and its de-intercalated *Stage-2* phase. Panel b) revealed the strongest $\mathbf{E}_{2g_1}$ Fano mode at 1585 cm^{-1} depicting *Stage-1* phase. Panel c) shows the intrinsic *Stage-2* mode at 1600 cm^{-1} with some reminiscent *Stage-1* contribution at around 1500 cm^{-1}. The line-shape of the 1600 cm^{-1} component is in accordance to the potassium and calcium de-intercalation $\mathbf{G}_{S-2}$ mode.

FWHM of the $\mathbf{G}_{S-2}$ mode in KC_{24} and CaC_x (Fig. 4.8 c), we lead into a correct assignment of the 1600 cm^{-1} mode to the *Stage-2* compounds.

4.4. Manifestation of charged and strained graphene layers in graphite intercalation compounds

Published in: ACS Nano, 2013 doi: 10.1021/nn403885k [196]

From a well controlled and consecutive *in situ* intercalation and high temperature de-intercalation approach the response of each stage up to *stage VI* is identified. The positions of the G and 2D lines as a function of staging depend on the charge transfer from K to the graphite layers and on the lattice expansion. Ab-initio calculations of the density and the electronic band-structure demonstrate that most (but not all) of the transferred charge remains on the graphene sheets adjacent to the intercalant layers. This leads to an electronic decoupling of these "outer" layers from the ones sandwiched between carbon layers and consequently to a decoupling of the corresponding Raman spectra. Thus higher stage GICs offer the possibility to measure the vibrations of single, double, and multi-layer graphene under conditions of biaxial strain. This strain can additionally be correlated to the in-plane lattice constants of GICs determined by x-ray diffraction. The outcome of this study demonstrates that Raman spectroscopy is a very powerful tool to identify local internal strain in pristine and weakly charged single and few-layer graphene and their composites, yielding even absolute lattice constants.

Raman response of stage II to stage VI GICs

We consider KC_8 as our starting potassium-graphite intercalation phase. Then we performed controlled temperature-driven de-intercalation experiments to synthesize the higher intercalation stages: *stage II* (KC_{24}), *stage III* (KC_{36}), *stage IV* (KC_{48}), *stage V* (KC_{60}), and *stage VI* (KC_{72}). The corresponding Raman spectra recorded with a 568 nm laser excitation are depicted in Fig. 4.10 a). The G-line always displays a high frequency component G_c between 1600 and 1610 cm^{-1}. This mode has a slight asymmetry due to the Fano interference of the conduction electrons in the electron doped charged layers and it is related to the charged graphene layers next to an intercalant layer. This assignment is also confirmed by comparison to *stage II* KC_{24}, where each graphene layer is in contact with potassium atoms and just charged graphene layers exist. Hence KC_{24} exhibits only one G-line as G_c at 1610 cm^{-1}. In addition, for stages higher than KC_{24} a second line G_{uc} appears around 1580 cm^{-1}. The position of the G_{uc} is close to the G-line in pristine graphite (1583 cm^{-1}) and of graphene [208] (1580 cm^{-1}). Therefore G_{uc} is assigned to the response of basically uncharged graphene layers surrounded by charged graphene layers. A detailed line shape analysis of the two G-line components using an asymmetric Fano line for the charged layers (G_c) next to an intercalant layer and a Lorentzian line for the uncharged carbon layers (G_{uc}) was performed. The results are closely matching the experimental spectra and are depicted as solid lines in Fig. 4.10 a). As shown in Fig.4.10 b), the positions of these two components are not constant and have a linear dependence on the intercalation stage. This shift is not predicted by the NL model. We will explain the shift below in an analysis that takes into account the small fractional charging even of the inner layers and the lattice expansion due to intercalation.

We find this linear relation between the intensity ratio R of the the two G-line components (G_{uc} and G_c), in agreement with the NL model as depicted by the relation $R = I_{uc}/I_c$ in Fig. 4.11

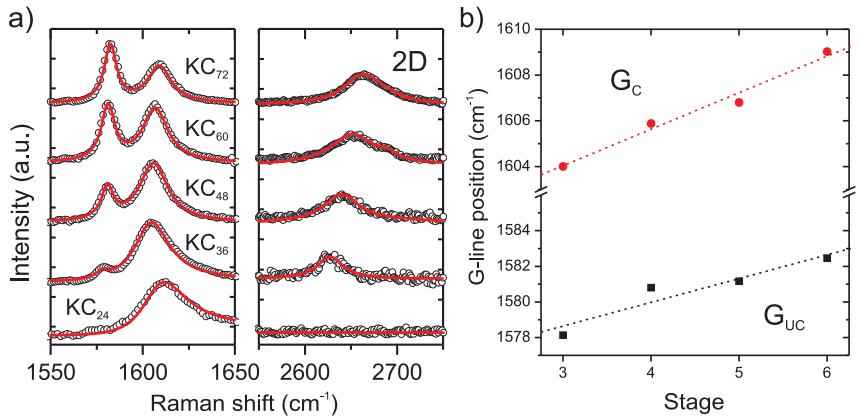

Figure 4.10: Raman spectra of *stage II* to *VI* GIC measured with a laser wavelength of 568 nm. In panel a) the spectra (black dots) together with the results of a line shape analysis (red line) in the region of the G and 2D line are depicted. Panel b) shows the positions of the two G-line components (G_c and G_{uc} as a function of stage n.

a) for *stages III* to *VI*. Our results using the 568 nm laser excitation agree very well with the results of Solin et al. Ref. [99]. R is also independent from the type of alkali metal intercalant for the case of K, Rb, and Cs GICs [99]. In order to analyze these highly staged GICs in more detail we performed a complete multi-frequency analysis as depicted in Fig. 4.11 b), and 4.12 for five different laser wavelengths.

A clear photon energy dependence of the intensity ratio between the charged and uncharged G-line components is obvious (see Fig. 4.12), but the linear dependence of R is universal (see

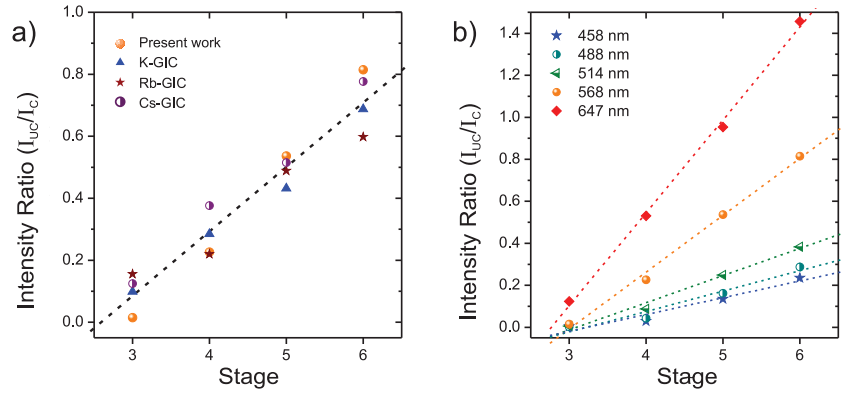

Figure 4.11: Panel a) and panel b) shows the intensity ratio (R) of the two components as function of n. In panel c) R was calculated from the Raman intensity of the low (G_{uc}) and high frequency (G_c) modes in the G-line and compared to the literature values of Ref. [17] for K, Rb and Cs intercalation measured with a 514 nm wave length. Panel d) shows the photon energy dependence of R together with a linear fit of $R=I_{uc}/I_c$ (dashed line).

Fig. 4.11 b) and can be safely used for the identification of the different stages (following the protocol explained below in the methods). This shows that in all cases the predominant charge transfer from the intercalant to the neighboring graphene layer is a valid approximation. The different slopes for different photon energies can be tentatively explained by a different frequency dependent resonance Raman cross section of G_c and G_{uc} and by different charge carrier absorption of the charged layers at high photon energies. This means that, in agreement with previous results, Raman spectroscopy can be used to unambiguously identify the different stages and correlate them to structural assignments by XRD. For the potassium intercalation stages *III* to *VI*, the 2D line displays a clear dispersion with respect to the laser energy (right panels in Fig. 4.12) and will be analyzed in the following.

We now turn to a detailed analysis of the double resonant 2D line. The NL model lets us expect that c and uc graphene layers give rise to separate 2D lines. We observe experimentally that the 2D-line is absent for *stage I* and *stage II* potassium GICs but present for the higher order stages and for pure graphene and graphite. This means that the 2D response is only due to the inner (uc) layers. The double resonance is suppressed for the outer (c) layers due to the strong charging. Therefore in *stage I* and *stage II* GICs where all graphene layers are adjacent to an intercalant, the 2D line is suppressed altogether. Interestingly this is not the case for p-type intercalation as recent results on $FeCl_3$ doped multilayer graphene, owing a doping level similar to Stage I GIC [77]. This different behavior might be due to a different localization of the charges transferred to the $FeCl_3$ ions upon p-type doping which should be investigated in future studies. For the stages *III* to *VI*, the 2D line displays a fine structure that depends on the number of uc layers as can be seen in Fig. 4.13 b). Therefore, considering that the double resonant Raman peak arises from the inner graphene layers only, we can regard a the inner layer of KC_{36} as a graphene mono-layer, the inner two layers of KC_{48} as a bi-layer, the inner three layers of KC_{60} as a tri-layer. In the analysis, we can thus draw an analogy with the splitting of the 2D-line in double- and few-layer graphene[210, 213]. A closer inspection of the 2D-line of the different GIC stages and fitting with two Voigtian functions, demonstrates indeed a splitting of this line

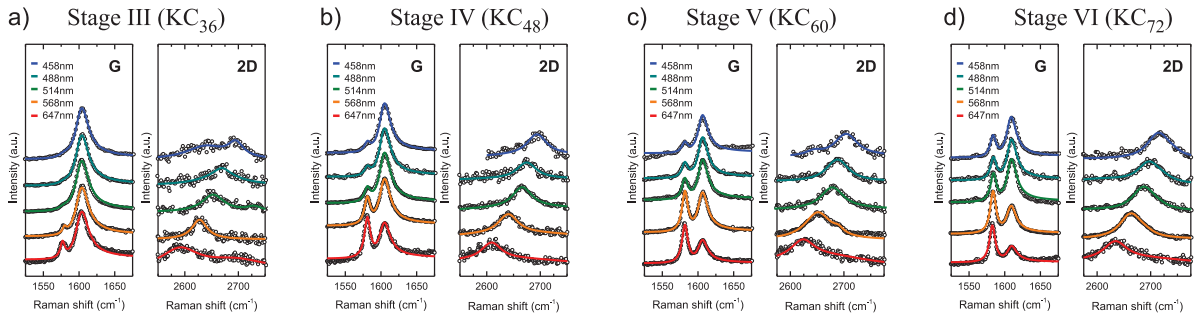

Figure 4.12.: Raman spectra from *stage III* to *stage VI* potassium GIC. The different spectra were acquired using laser-excitation wavelengths in the range of (458 nm and 647 nm). In the left panel of a), b), c) and d) the G-line of each intercalation compound is shown; in the right panels of each stage the 2D-line is depicted. The solid lines in the figure are fits using Voigthian and Fano line shapes (see text), respectively.

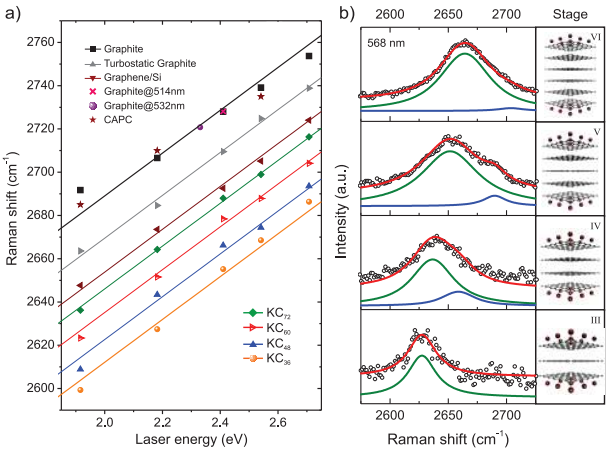

Figure 4.13: a) Dispersion of the most intense double-resonant 2D Raman mode in GIC, graphite and graphenes as function of laser energy. The different symbols depict the experimental 2D-line position measured. The values of graphene/Si, Turbostatic-graphite, and pristine graphite were extracted from Ref. [209], and [198, 210, 211] respectively. For comparison the 2D-line position of graphite at 514, and 532 nm (Ref. [72, 208]) are depicted as well as Compression Annealed Pyrolytic Carbon (CAPC) which falls into the same graphitic slope [212]. b) Detailed line-shape analysis of the 2D-line in *stage III to VI* is shown using up to two Voigthians (green and blue lines). The result of the analysis is shown as red line.

starting with *stage IV* (see Fig. 4.13 b). We observe a splitting of 25.71, 38.34, and 39.48 cm^{-1} between the two Voigtian functions of *stage IV*, *stage V*, and *stage VI* respectively, while *stage III* presents a 2D-line with one component only. In Fig. 4.13 a), we display the dispersion of the 2D line as a function of the laser energy. (For the stages where the 2D-line is split, we use the position of the lower peak which is much more intense than the upper peak as it can be seen in panel (b) and as it is explained in Ref. [214].) The slope of the 2D dispersion as a function of the laser energy is about 99 cm^{-1}/eV for all the different stages. This agrees with the dispersion of the 2D line of natural graphite, turbostatic-graphite [209] and graphene/Si [209] which are also shown in Fig. 4.13 a.

However, the actual position of the 2D line depends on the stage of the GIC. E.g., the 2D line of the inner layer in KC_{36} is down-shifted by about $\sim$36 cm^{-1} as compared to the 2D line of pristine graphene. Similarly, the 2D lines of KC_{48}, KC_{60}, KC_{72} are downshifted with respect to the ones of bi-, tri- and quad-layer graphene, respectively. The amount of the downshift decreases with higher stage number. In order to explore all possible reasons for this very pronounced downshift, we have performed a detailed theoretical analysis based on *ab-initio* calculations of charge density, electronic dispersion, and phonon frequencies.

Theoretical discussion of the Raman spectra

We discuss first the amount of charge transfer from the potassium intercalant layer to the different graphene layers. For this purpose, we have calculated the total charge density $\rho_{GIC}(z)$ as a function of the direction perpendicular to the layers, averaged over the in-plane directions (x-y-plane). From this, we subtract the "reference charge density", $\rho_{ref}(z) = \rho_C(z) + \rho_K$ which is the sum of the charge densities of the graphene layers and potassium layers calculated separately (in the geometry of the compound system). This method follows the earlier calculations by Hartwigsen et al. [215] on *stage I* intercalation compounds and by Ancilotto

and Toigo [216] on potassium adsorbed on a graphite surface. The charge density difference, $\Delta\rho(z) = \rho_{GIC}(z) - \rho_{ref}(z)$, is thus a convenient quantity to visualize charge transfer: it is negative around the position of the K atoms which tend to donate their electrons and it is positive where those electrons are accumulated. Fig. 4.14 a) demonstrates this for *stage III* KC_{36} under ABA-Stacking, and *stage VI* KC_{72} under AAA-Stacking in Fig. 4.14 c) (approximated model). Obviously, the electrons donated by the potassium atoms accumulate mainly on the potassium boundary carbon layers. In order to calculate a value for the charge transfer, we define (somewhat arbitrarily), the limit between the potassium and the carbon layer (marked i' in Fig. 4.14 a and c) as the value of z where $\Delta\rho(z)$ changes sign. Integrating the density-difference curve between those limits, one obtains a charge transfer of 0.39 electrons from each potassium atom to the graphene layers. Table 4.5 contains detailed information on the charge accumulation per layer. Most of the transferred electrons accumulate on the outer graphene layer. The charge concentration on this layer is almost independent of the staging. In contrast, the charge concentration on the inner layers remains (relatively) low and varies with the stage number. This explains why both the G_c and G_{uc} components depend only weakly on the stage number. The splitting which was already observed by Solin and Caswell [99] can now be understood on the basis of the high (and constant) charge density of the charged graphene layers. Due to the breakdown of the Born-Oppenheimer expansion, charging of graphene leads to a strong stiffening of the G-mode [102]. By electrochemical top-gating, electron concentrations of up to $5x10^{13}/cm^2$ have been achieved, [174] leading to a G-line position at about 1605 cm^{-1}. In GICs, the charge density on the G_c component reaches similar values (see Table 4.5) which explains its high frequency. On the other hand the low frequency observed for the uncharged component G_{uc} is also slightly affected by this charge transfer beyond the nearest neighbor. We obtained the G-line up-shift due to the charge density by using σ from Table 4.5, and Eq.3 from Ref. [217] as it gives the response of the system under adiabatic+expanded lattice conditions. This yields a calculated G_{uc} of between 1584 cm^{-1} and 1586 cm^{-1} for all different GICs. This is strongly overestimating the observed values and even yields the wrong trend, which highlights that there is some important ingredient missing in our explanation.

In order to address this point we first turn to the discussion of the 2D-line as a function of staging, making use of the double-resonance Raman model of Thomsen and Reich [188]. The model successfully describes the D and 2D dispersion as a function of laser energy as well as the splitting of the 2D line for double, triple, and multi-layer graphene [210, 213], provided that renormalization of the highest optical-phonon branch (HOB) due to electron-correlation effects is properly taken into account [185]. The different intercalation stages (2nd, 3rd, 4th, etc.) can be viewed, respectively, as bi-, tri-, and quadri-layer graphene, separated by K intercalant layers. One might thus expect a similar splitting and shifting of the 2D line as observed in Refs. [210, 213]. Instead, the experiments show an absence of the 2D-line for the *stage II* GIC, a single 2D-line for the *stage III* compound and an up-shift of the 2D line with increasing staging order (see Fig. 4.13). This difference can be understood as due to the charging of the graphene layers adjacent to the K atoms. In order to demonstrate this, we show in Fig. 4.14 b) the electronic band-structure (DFT-LDA) of *stage III* GIC KC_{36} (in ABA-Stacking configuration). The unit-cell contains 24 atoms per carbon layer, thus the band-structure is plotted in a $2\sqrt{3}$ x $2\sqrt{3}$ supercell

(compared to the primitive cell of graphene that contains only 2 atoms). In this supercell, the high-symmetry point K of the Brillouin zone of graphene is folded back onto Γ.

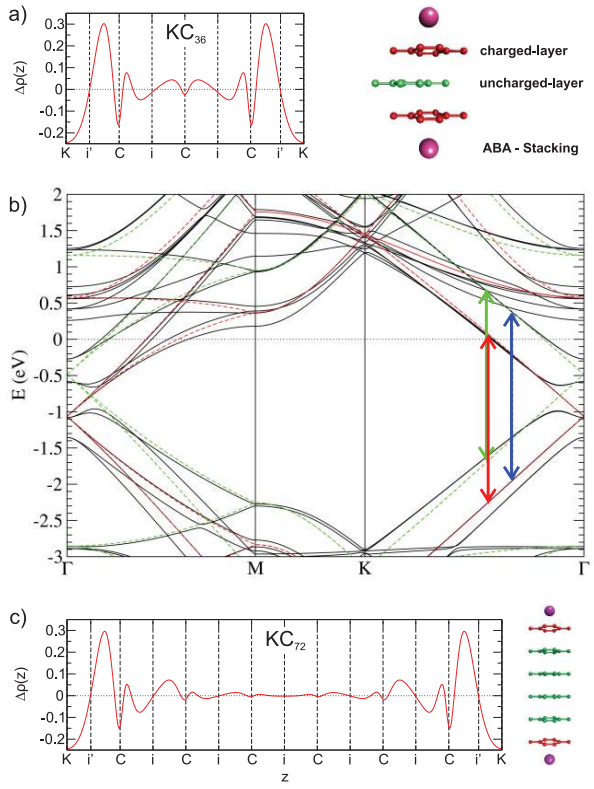

Figure 4.14: Charge density and Bad structure analysis. a) Charge density distribution for KC_{36} with a sketch of the charged and uncharged layers. In the charge density analysis, the position of planes consisting of carbon/potassium atoms is marked by C/K, respectively. Mid-points between graphene planes are marked by i and separation of the K and C planes, defined as the position where the density difference crosses 0, is marked by i'. In panel b), the band-structure of KC_{36} (black solid lines) and of pure graphene from our *ab-initio* is shown. The pristine graphene bands are shifted in energy to match the bands of the charged layer (red-dashed lines) and of the uncharged layer (green dashed lines). The red, green and blue vertical arrows mark the transition between the π-bands of the charged-charged, uncharged-uncharged and charged-uncharged layers at 2.3 eV laser energy. In panel c) the same analysis of the charge distribution as in a) is depicted for KC_{72}.

KC_{36} displays notable exceptions from the linear crossing of the π-bands due to the inter-layer interaction. Along with the band-structure of GIC, we plot the band-structure of pure graphene, displaying the linear crossing of the π-bands at Γ (K in the primitive cell). We shift the graphene bands in energy such that they match the corresponding bands of KC_{36}. The red-dashed lines correspond to the electronic bands of the charged graphene layers. The Dirac point is shifted to ΔE_1 = 1.07 eV below the Fermi level, corresponding to a strong charging. The green-dashed lines correspond to the electronic states of the weakly charged layer. Correspondingly, the Dirac point is shifted downwards only by ΔE_2 = 0.49 eV. This shift of the Dirac point gives us an additional measure for the charge density of the layers: From the density of states of graphene, $n(E) = |E|/(\pi\hbar^2 v^2)$, where v is the Fermi velocity of graphene, one obtains the charge density by integration over the energy from the Dirac point to the Fermi level: $\sigma(E_F) = ((E_F)^2 e)/(2\pi\hbar^2 v^2)$ This connection of Fermi-level shift and electron density was also used in Ref. [218] for the determination of the average doping level based on work-function measurements.

With the DFT-LDA value of the Fermi velocity of v = 0.85x10^6 m/s [219], we obtain σ_1 = 5.9x10^{13} cm^{-2} for the charged layer and σ_2 = 1.2x10^{13} cm^{-2} for the uncharged layer in KC_{36} (4.14 a).The value of σ_1 is 13% larger than the corresponding value in Table 1, while the

value off σ_2 is 47% smaller than the value in Table 4.51. These differences give an indication of the uncertainties of different charge transfer assignments (the electrons localized in between layers cannot be unambiguously assigned as belonging to one or the other layer). We note that our band-structure calculation is in qualitative agreement with the early ab-initio band-structure calculations of Ohno and Kimamura[220]. The difference is that in the present work, the fractional charge transfer from the intercalant layer to the graphene layers is calculated self-consistently while in Ref. [220] is was introduced as a parameter.

Concerning the 2D-line results of KC_{36}, we need to answer two questions: (i) why is the 2D-line not split into two peaks like the G-line? (ii) Why is the 2D line down-shifted by about 40 cm^{-1} compared to pure graphene?

In Fig. 4.14 b), vertical arrows mark dipole-allowed electron-hole pair transitions corresponding to a laser energy of 2.3 eV. Since in this energy range, the π-bands of KC_{36} almost exactly match the (shifted) π-bands of pure graphene, the transitions take place at the same electronic wave-vector. In the double-resonance Raman model the electron/hole performs a quasi-horizontal transition to a state in the vicinity of the neighboring point K'. This means that phonons with equal wave-vector $\mathbf{q}$ are excited in graphene and KC_{36}. The red vertical arrow marks a transition where the excited electron is barely above the Fermi level. This transition (in the charged layer) is therefore strongly suppressed with respect to the one marked by the green vertical arrow which is an electronic excitation in the uncharged layer. Thus, contrary to the G-line, only one component of the 2D-line is present in the spectrum of KC_{36} (and no 2D-line is visible for *stage II* GIC KC_{24} where only the strongly charged layers exist).

We have also considered the blue vertical transition from the π-band of the charged layer to the π^* band of the uncharged layer. However, since it is an inter-layer transition, its oscillator strength is negligible compared to the one of the intra-layer excitations. Since the electronic structure of the uncharged layer is decoupled from the one of the charged layer (as manifested by the almost rigid band shift in Fig. 4.14 b), one might expect little or no difference in frequency between the 2D line of isolated graphene and the one of KC_{36}. Indeed, several reasons could be found (related to the strong Kohn anomaly of the highest-optical branch at K [70]) that could even explain a slight up-shift of the 2D-line: (i) The residual charging of the inner layer leads to a reduction of the electron-phonon coupling around K [221] and might increase the 2D position by 10 cm^{-1} (extrapolated from Fig. 2d of Ref. [222]). (ii) The opening of a gap between the π bands at Γ (K) could lead to a partial suppression of the Kohn-Anomaly in analogy to what happens for graphene in close contact to a Ni(111) surface [51]. (iii) The dielectric screening by the quasi-metalic environment could reduce the Kohn-Anomaly as recently observed for graphene on dielectric substrates. In order to check if any of the above three arguments holds, we performed a phonon calculation [223] of the HOB at K, comparing the mode of the single layer with the mode of the inner layer of *stage III* potassium GIC. The mode of the uncharged layer has a frequency of 1269.6 cm^{-1} while the mode of the single layer has 1271.9 cm^{-1}. We conclude that the phonons of the HOB around K remain essentially unchanged if the lattice constant of KC_{36} is the same as the one of graphene. However, there are subtle changes for the lattice constant as a function of staging. Nixon and Parry have measured the expansion of the carbon-carbon bond length in potassium GIC (see Table 4 in Ref. [97]). The lattice constant of KC_{36} is 0.20% larger

Table 4.5.: Calculated charge transfer (e^- per K atoms) from the intercalated K atoms to the graphene-layers for *stage III* to *VI* potassium GIC. The last column gives the bi-axial strain of the graphene layers [97].

	el. per K atom				σ (10^{13}/cm^2) *			Bi-axial strain (%)
	K	1st	2nd	3rd	1st	2nd	3rd	
KC_{36}	-0.39	0.33	0.12	-	5.2	1.9	-	0.20
KC_{48}	-0.39	0.28	0.11	-	4.5	1.7	-	0.13
KC_{60}	-0.39	0.26	0.11	0.04	4.1	1.7	0.6	0.10
KC_{72}	-0.39	0.26	0.10	0.03	4.1	1.6	0.5	0.06

* The corresponding electron density is given in electrons/cm^2.

than the one of graphite. In order to verify this experimental result, we have performed a full cell-optimization of KC_{36} and of pure graphite: we obtain a theoretical bond-length expansion of $\sim$0.22% in very good agreement with the experiments.

Therefore we can use the experimental lattice expansion from the XRD measurements in Ref. [97] of different GICs (whose values are also given as last column in Table 4.5) to evaluate the redshift of the Raman response. This is equivalent to putting strain on the individual graphene layers. This strain induced lattice expansion in graphene has previously been related to the phonon frequency of the G and 2D line using the Grüneisen parameter [72, 224] in experiments applying uni-axial [210, 225, 226] and bi-axial strain[224]. In our experiments, the regular incorporation of potassium atoms in between the layered structure of graphite, results in bi-axial strained graphene layers. The shift of Raman frequency as function of strain was calculated by using the relation $\gamma = -1/\omega_0 \cdot \partial\omega/\partial\varepsilon$ where ω_0 is the Raman frequency without strain, $\partial\varepsilon$ is our calculated bi-axial strain in GIC, and γ= 2.2, and 3.3 is the Grüneisen parameter for the G and 2D band phonons respectively [224].

For KC_{36} we have calculated the phonon-frequency shift of pristine graphene, and lattice expanded graphene. For the HOB between K and M the frequency down-shift is about 18 cm^{-1}. This corresponds to a 2D-line redshift by 36 cm^{-1}. Thus, we can conclude that the redshift of the 2D-line (with respect to graphene) is almost entirely due to the small (but non-negligible) lattice expansion of the GIC. This lattice expansion also has a profound influence on the G-line position. This latter is, however, also influenced by the charge transfer as will be described in detail below.

Charge transfer and bi-axially strained graphene layers in GIC

These two factors had been linked by Pietronero and Strässler [227] considering the well established C-C bond length in GIC as a main tool to determine the charge transfer in those systems. Hitherto, these two main factors directly affect the Raman response in GIC by: (i) the induced charge transferred from the K atoms into the carbon layers, and (ii) the in-plane strain coming from the change in the C-C bond length. However, no detailed quantitative information about this strain nor about its origin in the case of donor compounds is known to date. Our analysis about the charge transfer and bi-axial strain, have revealed not only the fractional charge transfer per intercalant atom (Table 1), but also, a solid understanding of its relationship with the

electronic band structures of the GICs (4.14b) and their corresponding Raman spectrum as it will explained in the following, and depicted in Fig. 4.15.

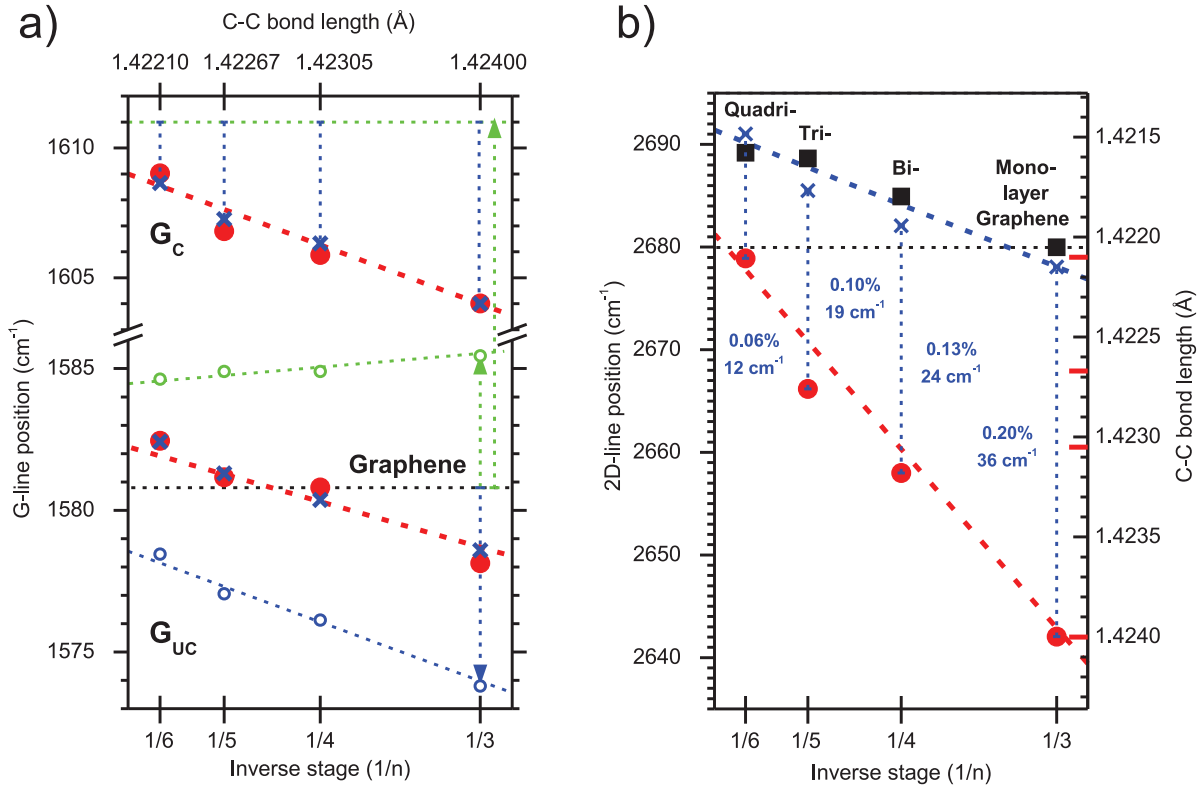

Figure 4.15.: In panel a) the G-lines of the potassium GIC is depicted as function of the inverse stage. The upper x-scale depicts the C-C bond length of the XRD results of Ref. [97]. The dashed green lines and the green open circles show the G-line upshift due to the high charge transfer to the charged G_c component and the remaining small charge transfer to the G_{uc} component. The blue dashed line and blue open circles come from the bi-axial strain induced softening of the G-line of graphene (black dashed line). The blue crosses depict the positions after adding the charge transfer and subtracting the internal strain. In panel b) the 2D-line position of the high-frequency-mode of GIC (red circles) and of unstrained (multi-layer)graphenes from Ref. [210] (black squares) is plotted as function of inverse stage. The dashed blue lines values in the figure depict the frequency softening by biaxial strain. The blue crosses depict the positions after subtracting this internal strain. The second y-scale depicts the C-C bond length owing a linear relation to the 2D line. The short red line are the experimental XRD bond length of the upper x-axes in panel a).

In the left panel (4.15 a) we show the frequency dependence of the G-line components as a function of inverse stage. Experimentally, for both the G_{uc} and the G_c component (red circles), we observe a linear decrease in frequency from *stage VI* to *III*. The slope as function of inverse stage (red dashed line) is slightly lower for G_{uc}. In addition, the C-C bond length of the different GIC from XRD studies of the in-plane lattice expansion of Ref. [97] are shown on the top axis.

In order to understand the staging dependence of both G-line components, we have to add the effect of lattice expansion and of charge transfer. Starting from the G-line position of pristine graphene [208, 213] (black dashed line) we have to add the upshift from the increased charge density on the layers and the down shift from the bi-axial strain on the graphene layers and the corresponding change in the C-C bond length. We show these two contributions to the G-line as vertical green arrows (for the charge transfer related stiffening including the corresponding lattice expansion [217]) and vertical blue arrows (for the additional effective bi-axial strain), respectively. For the G_{uc} component we can evaluate the upshift due to the increased charge density using our calculated charge transfer to the G_{uc} summarized in Table 4.5 (green open circles in Fig. 4.15 a). The resulting charge transfer to the G_{uc} is lowest for KC_{72} and has an approximately linear increase with inverse stage. Concomitantly, the downshift due to the effective biaxial strain (blue open circles) are also shown. The resulting frequencies of the G_{uc} component in GIC (blue crosses) perfectly match the values of the experimental G_{uc}. In order to confirm the additivity of the effects of charge transfer and lattice expansion, we also performed non-adiabatic calculations of the phonon frequency of charged layers a fixed lattice constant. For this purpose we use the method for the non-adiabatic phonon calculation of Ref. [228] which yields values very close to the method of Ref. [217]. For KC_{36} this yields a nominal upshift of 13.8 cm^{-1} for the G_{uc}, which together with the downshift of 15 cm^{-1} (determined from the experimental total lattice expansion determined by XRD using the Grüneisen parameter for the G phonons of Ref. [224]), yields a position of 1579.6 cm^{-1}. This is in excellent agreement with the results using an effective strain. We also verified computationally (by variation of the lattice constant for neutral and charged graphene) that the Grüneisen parameter remains constant for the charge values observed in GICs. This means that both effects are truly additive. For the G_{uc}, about 50% of the observed experimental average lattice expansion measured by XRD are related to the charge transfer from the intercalants.

For the highly doped G_c component the story is more complex. Experimentally the Raman response of highly doped graphene has been achieved by polymer electrolyte gating [174, 229] and by alkali metal vapor dosing [85, 230]. Interestingly for a broad range of electron concentrations between $4{\cdot}10^{13}/cm^{-2}$ and $10{\cdot}10^{13}/cm^{-2}$ a position of 1611 cm^{-1}, very similar to the 1610 cm^{-1} mode in highly charged KC_{24}, is observed [230]. This saturation in the Raman frequency at high doping is also reported theoretically [217], also the absolute frequency is not correctly addressed in the theoretical description at high charge transfer. Therefore, in a broad doping range the charge transfer induced strain compensates the non-adiabatic effects. For this reason, we used the experimental position of the "pristine" G_c since we observe for all intercalation compounds a charge transfer to the charged layers above $4{\cdot}10^{13}/cm^{-2}$ (see Table 1). Interestingly, although one would expect a higher contribution of the charge transfer to the effective strain, adding the the same effective bi-axial strain as for the G_{uc} we find a nearly perfect match of the resulting frequency (blue crosses) with the experimental G_c. This confirms that the G-line response in GIC is related to charged and strained graphene layers. We point out that this model cannot be directly applied for *stage I* and *stage II* GIC because there are no uncharged graphene layers, the charge transfer is much stronger and the line position is influenced by the Fano interference with the conduction electrons. [57, 99]

The same analysis performed to the second order 2D line (strongest component related to the main second order Raman process) is shown in Fig. 4.15 b. We observe a linear decrease in position of the main 2D line as function of the inverse stage (red circles). The vertical dashed blue lines again correspond to the strain induced downshift of pristine graphene. The blue labels in the figure correspond to the relative percentage of bi-axial strain from [97] and the evaluated downshift using the Grüneisen parameter for the 2D-line [224]. Due to the higher frequency of the 2D line a much bigger shift between 10 and 40 cm^{-1} is observed. The upshift due to the residual weak charging can be estimated to be less than 2 cm^{-1} [210] and can be neglected. Therefore, we are able to artificially "release" the biaxial strain and compare the 2D-line in "unstrained" KC_{36}, KC_{48}, KC_{60}, and KC_{72} (blue crosses in Fig. 4.15 b) to the experimental position of unstrained mono-, bi-, tri-, and quad-layer graphene from Ref. [210] (black squares in Fig. 4.15 b). We find a very good agreement. This confirms that the 2D-line in GIC comes from strained multi-layer graphene.

In addition we can go one step further and compare the 2D line position to absolute in-plane lattice constants of the graphene layers based on the XRD results. This relies on the fact that Nixon and Perry [97] observed a linear relation of the in plane lattice constant *versus* inverse stage of the GIC. This allows to use the measured lattice constants to accurately correlate the 2D frequency to the C-C bond length shown as the right y-axes of Fig. 4.15 b). Thus, one can use the 2D Raman response directly to determine the in-plane lattice constant of mono- and multi-layer graphene as a function of their internal strain even on an absolute scale. This demonstrates that Raman spectroscopy is a very powerful tool to identify local internal strain in single and few-layer graphene and their nanoelectronic devices and composites, yielding even absolute in plane lattice constants.

Materials and Methods The intercalation experiments on natural graphite single crystals have been conducted *in situ* in a vacuum better than $\sim$4x10^{-8} mbar keeping the graphite sample inside a quartz ampoule with a flat surface. The Raman measurements have been performed using 458, 488, 514, 568, and 647 nm excitation wavelengths at 1.2 mW between 1400 cm^{-1} to 3000 cm^{-1}. Potassium with a 99.95% purity (Aldrich) was evaporated until bright golden graphite crystals which are assigned to stage I KC_8 were obtained [57]. Subsequently, the sample was resistively heated to 200°C until it turned homogeneously blue (characteristic color of *stage II* KC_{24}). A controlled *in situ* high vacuum high temperature de-intercalation process was performed by increasing the temperature in steps of 50°C [82]. The line positions were corrected by employing calibration lamps. Six potassium GIC *stage I* to *VI* (KC_8, KC_{24}, KC_{36}, KC_{48}, KC_{60}, and KC_{72}) were identified for all laser lines used. Once each stage was identified we followed a protocol acquiring multi-frequency Raman spectra keeping constant the acquisition region, and maintaining the lowest possible exposure time to avoid laser induced de-intercalation as for instance reported by [60] and later on by us [57].

The calculations were performed using density-functional theory in the local density approximation. We have used the code **quantum-espresso** [184]. For the values of the K-C and C-C inter-plane distances as well as for the in-plane lattice constants, we used the experimental values given in Table 4 of Ref. [82], *i.e.*, $a = 1.42\AA$ for the bond-length, $d = 3.35\AA$ for the inter-plane distance in graphite, and $d_M = 5.41\AA$ for the distance between the intercalated layers. For sim-

plicity, in order to keep super-cell size low, we used AA-stacking in adjacent graphene-layers, except for KC_{36} where we used ABA-stacking. K atoms were placed between the centers of carbon hexagons. No geometry relaxation was undertaken. The reciprocal unit-cell was sampled by a $6\times6\times2$ Monckhorst-Pack grid. Norm-conserving pseudopotentials (with nonlinear core correction for K) and an energy cutoff at 60Ry were used.

4.5. Spectroscopic investigation of nitrogen doped graphene

Published in: Applied Physics Letters, **101**, 123108 (2012) doi: 10.1063/1.4752736 [183]

Current research efforts are aimed at controlling the electronic properties via doping graphene. Previously, dopant-induced changes in the Fermi velocity were observed to result in an effectively downshifted Raman peak below the G'-band for n-doped carbon nanotubes. However, in the case of N-doped graphene, we find that several Raman features vary depending upon both dopant concentration and its bonding environment. For instance, only pyridinic/pyrrolic dopants were observed to result in intense D/D'-bands with a concomitant downshift in the G'-band. Here, we correlate x-ray photoelectron measurements with Raman spectra to elucidate effects of dopant bonding configuration on vibrational properties of graphene.

The presence of a strong coupling between the electronic and vibrational properties in graphene makes it possible to probe the dopant environment and the associated changes in the electronic properties using Raman spectroscopy. Maciel *et al.* [151, 152, 155, 160–163] have used Raman spectroscopy as a tool to probe the electron and phonon energy renormalization in doped single-walled carbon nanotubes (SWNTs). The electron velocity was found to increase near a negatively charged defect, which in turn influenced the lattice vibrations locally and resulted in the observation of a charged defect induced Raman peak (G'_D) that was found downshifted in energy relative to the G′ peak in n-doped SWNTs. In this letter, we present unique Raman signatures for CVD grown N-doped graphene, which depend on the dopant concentration, and the nature of local bonding environment in graphene. For instance, we observe that the nitrogen atoms bonded in the non-graphitic configurations (pyridinic, pyrrolic) result in intense

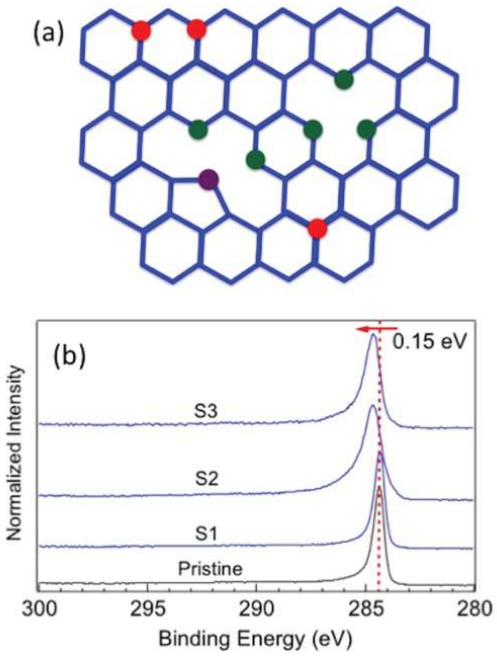

Figure 4.16: (a) A schematic of the bonding geometries of N in graphene. The green (pyridinic) and purple (pyrrolic) circles represent N atoms bonded in a non-graphitic configuration which result in holes in the graphene sheet with arm-chair like edges. On the other hand, the red circles represent N atoms that are bonded in a graphitic configuration and do not alter the honeycomb lattice structure. (b) XPS spectra recorded for the C 1s line with a photon excitation energy of 1486.6 eV. The bottom most spectrum (shown in black) corresponds to pristine graphene while the spectra in blue are for increasingly N-doped graphene. Clearly, the C 1s line is broadened for samples S2, S3 and is up-shifted in energy with increasing (from S1 to S3) dopant concentration.

D and D′ bands unlike the N atoms bonded in the graphitic configuration. Moreover, as in the case of N-doped SWNTs, the G′ band was found downshifted only in the case of pyridinic and pyrrolic graphene, but not in graphene with N in the graphitic bonding configuration. Finally, we correlate our detailed XPS measurements with Raman spectroscopy to elucidate the effects of dopant bonding configuration on the electronic and vibrational properties of graphene.

Figure 4.16 (b) shows the C 1s line obtained for both pristine and the N-doped graphene samples. The C 1s line for graphene exhibits a peak maximum at the binding energy of 284.45 eV and a full width at half-maximum intensity of 0.53 eV. This indicates that the graphene layers are effectively decoupled from the underlying Cu substrates. Further, the C 1s line was observed to broaden and upshift (∼0.1-0.16 eV) upon N-doping [231, 232]. As shown later, the shift and broadening of C 1s peak for sample S1 is significantly smaller compared to S2 and S3, due to lowest dopant concentration in S1. The gradual shift of C 1s line can be attributed either to differences in the N bonding environments or to the amount of N incorporated in the graphene layers.

From the N 1s lineshape analysis (see Fig. 4.17), we find different doping configurations present in our samples. It is important to note that in the case of graphene, armchair or zigzag edges can result due to different doping configurations [151]. For example, in pyridinic or pyrrolic graphene one of the carbon atoms is removed (vacancy) from the honeycomb lattice to form armchair like edges (see Fig. 4.16 (a)). As shown in Fig. 4.17, we observe three different doping configurations, viz., graphitic, pyrrolic, and pyridine-like N in our samples. The N 1s line was deconvoluted using Voigtian components, and the peak located at 400.5 eV (blue colored in Fig. 4.17) is identified with substitutionally doped nitrogen in the graphitic bonding configuration. The second peak located at ∼401.5 eV (orange colored in Fig. 4.17) has also been previously observed in doped nanotubes and is ascribed to different nitrogenated adsor-

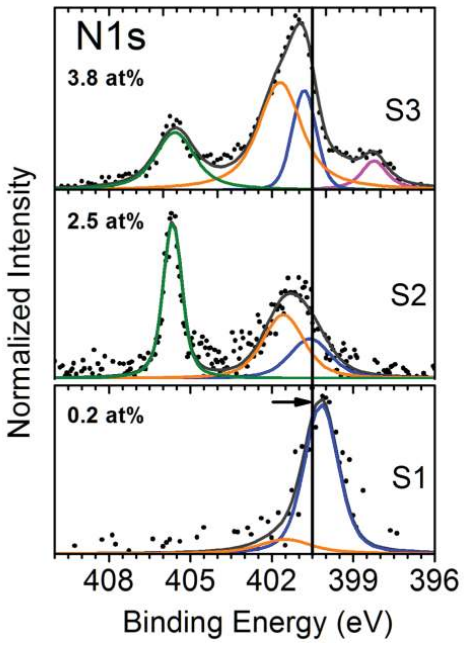

Figure 4.17: XPS spectra recorded for the N 1s line with a photon excitation energy of 1486 eV. The N 1s line was deconvoluted with symmetric Voigtian components considering the experimental conditions and the resolution (0.5 eV) employed in our measurements. The peak at 400.5 eV corresponds to graphitic or direct substitution of N atoms while the peaks at 398 and 400 eV arise due to non-graphitic doping configurations.

bants [233, 234].17,18 The origin of the peak present at ∼406 eV (green colored in Fig. 4.17) is attributed to adsorbed N species. Importantly, the peaks present at 398 (in S3) and 400 eV (in S1) arise from nitrogen bonded in the non-graphitic configuration.17,18 Previously, in case of CVD grown N-doped graphene, Wei *et al.* have attributed these peaks to pyridinic and pyrrolic doping environments, respectively [151]. In order to understand the correlation of N incorporation in graphene with its spectrally identifiable features in Raman and XPS, we have broadly classified the doping configurations in our samples as graphitic (as in S2) and non-graphitic configurations (as in S1 and S3). In other words, we find that sample S2 exhibits graphitic doping environment while the samples S1 and S3 show additional defects such as vacancy in the honeycomb lattice appearing due to pyridinic/pyrrolic substitution. Specifically, the peak at 398 eV in S3 corresponds to the pyridinic configuration while the substitutional configuration is slightly shifted to ∼400 eV in S1, as shown by the red arrow in Fig. 4.17. Furthermore, we quantify the substitutionally doped N by taking into account the relative photoemission cross-sections for the C 1s and the corresponding N 1s (substitutional doping) peaks. We find that S1, S2, and S3 contain 0.2, 2.5, and 3.8 at. % nitrogen, respectively. In the following section, we correlate these bonding environments to changes in the Raman spectra of S1, S2, and S3.

Raman spectrum of graphene exhibits several sharp features such as the disorder band (D band), graphitic band (G band), and the G′ band. Typically, the D band is present at ∼1350 cm^{-1}, and its origin is due to the presence of structural disorder in the graphene lattice. For example, presence of vacancies, impurities, or dopants, edges, and finite size effects that break the translational symmetry may activate the D band. Previously, the intensity of D band (relative to the G band) was observed to increase concomitantly with increasing nominal doping concentration of nitrogen in N-doped SWNTs [235]. On the contrary, as shown in Fig. 4.18, our samples do not exhibit such a concomitant increase in the D band feature. In fact, the D band intensity is found to be highest for samples with non-graphitic dopant configuration (S1 and S3). In addition, these samples also exhibit an additional peak at ∼1620 cm^{-1} (known as the D′ band). The origin of the D and D′ band is well understood within the framework of the inter-valley and intra-valley double resonance process in SWNTs and graphene.20 Previously, Cancado *et al.* [236] argued that the defect wave vector associated with armchair edges can connect two inequivalent K and K′ points (or support inter-valley scattering) in the Brillioun zone unlike the zig-zag edges. Thus, the D band for armchair edges is more intense compared to the zig-zag edges [236]. In our samples, non-graphitic doping configuration (sample S1 and S3) leads to holes in the graphene sheets which contain arm-chair like edges (cf., Fig. 4.16 (a)), and consequently the D band intensity (relative to the G band intensity) is higher for samples S1 and S3 (cf., Fig. 4.18 (a)). In addition, the D band also broadens more in samples S1 and S3 compared to S2 due to the lattice disruption by non-graphitic dopants. It is important to note that the above Raman features were prevalent on millimeter scale in all our samples.

The differences in the electronic band structure of single-layer (SLG), bi-layer (BL), and few layer graphene (FLG) are clearly reflected in their Raman spectra. Depending on the number of layers, the G′ band present at ∼2700 cm^{-1} in the Raman spectrum of graphene exhibits a characteristic lineshape. For example, the G′ band in SLG can be fit to a single Lorentzian peak while it can be deconvoluted into four Raman peaks (processes $P_{ij}; i, j = 1, 2$) for the BLG [237].

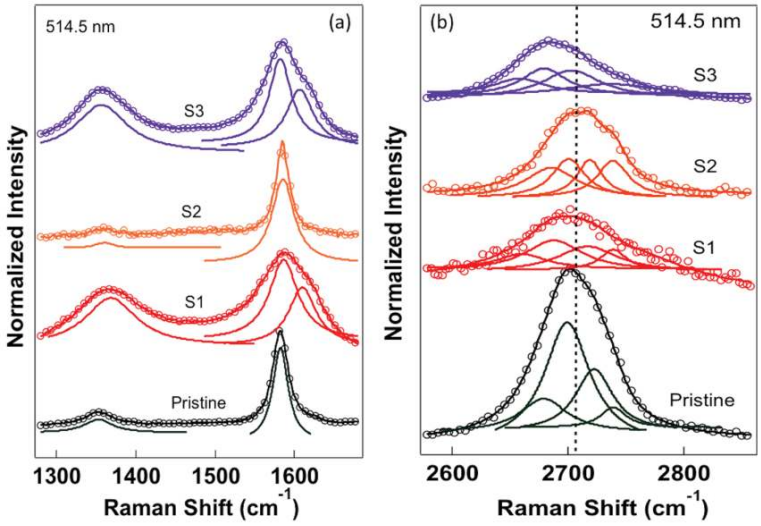

Figure 4.18: Raman spectra of pristine and N doped graphene. As seen in panel (a), the D and D′ bands are intense for samples S1 and S3 (non-graphitic doping configuration). The D- and G-bands for S2 (graphitic doping configuration) are very similar to pristine samples except for the defect-induced broadening. The electron-phonon renormalization upon doping leads to a net down-shift in the G′-band peak position for samples with a non-graphitic doping configuration.

Our CVD grown samples clearly exhibit a four peaked structure in the G′ band confirming that the samples are indeed bilayer graphene (Fig. 4.18 (b)). The G′ band is also a double resonance process similar to the D and D′ bands. In the double resonance process for the G′ band, an excited electron with a wave vector k resonantly couples to (two) *iTO* phonons with $q = -2k$. The resonant condition (for $q = -2k$) may be written in terms of laser energy (E_{laser}), electron and phonon wave vectors (k and q), Fermi and phonon velocity (v_f and v_{iTO}) as follows:

$$E_{laser} = 2\hbar\, v_f\, k, E_{phonon} = \hbar\, v_{iTO}\, q, E_{G'} = 2\, E_{phonon}, \frac{\partial E_{G'}}{\partial E_{laser}} = 2\frac{v_{iTO}}{v_f}. \tag{4.6}$$

Previously, Maciel *et al.* [238] showed that the defect-induced renormalization of electron and phonon energies can influence the double-resonance scattering process for the G′ band intensity in SWNTs. The electron phonon energy renormalization near a charged defect site resulted in the appearance of an additional $G_{D'}$ peak which was downshifted (up-shifted) in energy relative to the G′ peak in n-doped (p-doped) SWNTs [238]. Although the renormalized phonon energy was higher when compared to that in the unperturbed state, the $G_{D'}$ feature appeared below the G′ band frequency in the Raman spectrum of n-doped SWNTs. Such an observation was attributed to the relatively weaker dispersion of $G_{D'}$ band [238]. In other words, the defect increases the *iTO* phonon energy by reducing its velocity (v_{iTO}) near the K point with a concomitant increase in the electronic Fermi velocity (v_f). This causes the double-resonance process to select a lower frequency phonon and exhibit a smaller dispersion with E_{laser} [238]. In the case of graphene, we observe the following differences in Raman signature compared to doped SWNTs: (i) The

downshift in G′ band is strongly dependent upon the dopant configuration and (ii) the interlayer interaction overwhelms the dopant induced changes. As shown in Fig. 4.18, the G′ band for pristine sample exhibits four peaks characteristic of BLG. Clearly, the maximum downshift in G′ band is observed for sample S3 ($\sim$25 cm^{-1}) which contains relatively large amounts of dopant ($\sim$3.5 at. %). Interestingly, sample S2 shows little or no downshift albeit 2.5 at. % of dopant is present in the sample, whereas sample S1 shows a discernible downshift ($\sim$10-15 cm^{-1}) even in the presence of only 0.2 at. % dopant concentration. We attribute the varying downshifts in the G′ band frequency to differences in the local bonding environment of nitrogen in S1, S2, and S3. In the non-graphitic bonding configuration the electronic structure is strongly perturbed when compared to that in graphitic bonding configuration due to the change in crystal symmetry upon removal of carbon atoms. The presence of edges in the non-graphitic bonding configuration may renormalize the electron and phonon energies more strongly, leading to a discernible downshift in the G′ band frequency even at low dopant concentrations. Previously, the $G_{D'}$ peak and the electron-phonon renormalization were explained for doped SWNTs using SLGs Dirac-cone like structure near the K-point (cf., Eq. 4.6)). However, the interlayer interaction in BLG is known to result in hyperbolic band structure. Further, as described above, the hyperbolic band structure in BLG leads to 4 distinguishable Raman features (P_{ij}) in the 2D band region (see Fig. 4.18 (b)). In order to describe the dispersion of phonon energy (w.r.t E_{laser}) for BLG, the first relation in Eq. 4.6 needs to be replaced by:

$$E_{laser} = \gamma_1 \left(\sqrt{\frac{1 + 4\hbar^2 v_f^2 k^2}{\gamma^2 - 1}} \right) \tag{4.7}$$

where, γ_1 is the inter-layer hopping energy. The renormalized phonon energies in BLG are more complex unlike SLG or SWNTs due to the hyperbolic $E - k$ relation. Therefore, the defect-induced $G_{D'}$ feature is not well resolved in BLG due to the hyperbolic band structure. Further, the G′ band is broader ($\sim$100 cm^{-1} in BLG compared to 30 cm^{-1} in SLG) due to P_{ij} which makes it difficult to clearly identify the $G_{D'}$ peak.

Chapter 5

SUMMARY AND OUTLOOK

In conclusion, along this thesis six different studies were performed including functionalized graphene, and n- and p-type doped graphite intercalation compounds. We have performed a detailed Raman study of several defect modulated KC_8 single crystals. We identified several different Raman responses for different nominal KC_8 phases which can be distinctly assigned by their color and brightness. All these Raman responses match the spread of different line shapes reported in the literature so far. From an evaluation of the fine structure in the **G-line** response and a comparison to the intensity of the *z-axis* out of plane motion at 560 cm^{-1}, which is only observed in KC_8, we derive a unique way to identify the response of the intrinsic KC_8 phase and distinguish it from the defect modulated and partly de-intercalated phases. We find this intrinsic E_{2g_2} mode at 1510 cm^{-1} with a line-width of 176.7 cm^{-1}. The position is similar to many other stage one intercalation compounds. The calculated electron phonon coupling renormalized line-width is closely matching our experimental values, which highlights that in KC_8 the phonon decay channel into dressed electron -hole pairs is the dominant one.

From a detailed in-situ Raman study of *stage I* GIC (KC_8, CaC_6, and LiC_6) we identify four main peaks in the D- to G-band region, and all these Raman responses match the spread of different line shapes reported in the literatures so far. From an evaluation of the fine structure in the G-line response we assign each peak to their corresponding vibrational mode and phonon branch. We found the strongest Fano behavior of the G-line at 1510 cm^{-1} in KC_8 and CaC_6, not like in LiC_6, which highlights the importance of this mode to the superconductivity coupling mechanism within the BSC theory, and confirms the importance of this E_{2g_2} mode to non-adiabatic effects. By using this mode, we obtain a very good agreement to the theoretical predicted line-width $\gamma^{EPC} \simeq \Gamma_{ph}$ especially for CaC_6.

Finally, we find a very small EPC $\lambda_{ph} < 0.06$ which is much too low to explain the high T_c in this graphite intercalated compounds. This points out that, other phonons including acoustic modes and other electronic states might play an important role in explaining the superconducting pairing in GIC.

Turning in to the results from *Stage-1* and *Stage-2* GICs, the change in the shape of the G-

line Raman spectrum was well pronounced and associated to the active bond-stretching mode in graphite. This mode is broadened and shifted due to the charge transfer and concomitant Fano interference with non-adiabatic electrons via intercalation of alkali-metals (i.e. K, Ca, Li). Our results allow a detailed analysis of the actual doping from the position and shape of the G-line alone. The G-line in *Stage-1* compounds is confirmed to be composed of more than one component. The $\mathbf{E}_{2g}$ mode in superconducting GICs has an intrinsic Fano line-shape and shows up as peak at 1510 cm^{-1}. Upon laser induced de-intercalation, the line-shape of *Stage-1* GICs is modulated finally reaching the *Stage-2* GIC. The intermediate phase can be explained by a change of the relative intensities of the different components. This confirms the phase separation and is validated by a superposition fitting of the *Stage-1* and *Stage-2* components.

The final *Stage-2* compounds exhibit a constant background with complete absence of the C_z mode. The position above 1600 cm^{-1} and small FWHM of $\simeq$35 cm^{-1} highlights the intrinsic G-line of *Stage-2* compounds ($\mathbf{G}_{S-2}$) in accordance to recent results [85, 195]. Therefore, these in-situ de-intercalation experiments performed on high-vacuum conditions confirm that the $\mathbf{G}_{S-2}$ mode is intrinsic from the de-intercalation process and not due to oxidation after air exposure.

The $\mathbf{G}_{S-2}$ mode also evidence the interaction between the intercalant and the graphitic intra-layer mode due to its slight Fano asymmetry ($\mathbf{q}\simeq 7$). Hence, the universal de-intercalation behavior of the G-line response observed in potassium, lithium and calcium GIC, provides a a clear fingerprint for the correct stage identification in *Stage-1* and *Stage-2* GICs.

Going further in deintercalation, we also analyzed the intrinsic Raman response from strained graphene layers in graphite intercalation compounds. For *stage III* and higher there are two nearest layer environments: heavily charged graphene layers adjacent to an intercalant layer and basically uncharged graphene layers sandwiched between other graphene layers. By *ab-initio* calculations of the charge densities and the electronic band dispersions, we have demonstrated that the charge transfer is incomplete (less than 1 electron per potassium atom) and that most (but not all) of the transferred charge remains on the charged graphene layers adjacent to the intercalants. This leads to an electronic decoupling of the inner (uncharged) from the outer (charged) layers and consequently also to a decoupling of the corresponding Raman spectra: The G-line splits into two peaks and the 2D line is entirely due to the uncharged inner layers while the 2D line of the outer layers is suppressed due to the strong charging. The quantitative interpretation of the peak positions requires that the internal strain of the graphene layers is taken into account. This allows to unambiguously identify the Raman response of strained charged and uncharged graphene layers and to correlate it to the in-plane lattice constant determined by XRD. Therefore Raman spectroscopy is a very powerful tool to identify local internal strain in uncharged and weakly charged single and few-layer graphene yielding even absolute lattice constants. This has important implications for the application of Raman spectroscopy to identify for instance the strain in nanocarbon based nanoelectronic and optoelectronic devices as well as the local interfacial strain in graphene and carbon nanotube polymer composites on an absolute scale.

Much less is known on the complementary p-type intercalation compounds using molecular acceptors like $FeCl_3$, H_2SO_4 or HNO_3. For these p-type intercalation compounds of nanocarbon

systems supramolecular interactions of the acceptor molecules and the nanocarbon system play a key role in the understanding of their structure as well as the complex interplay between charge transfer and covalency. Especially, the fraction of van der Waals, ionic and covalent character whose interaction is a key for understanding their electronic and optical properties as well as their application potential. A future investigations I would like to tackle this issue using a combined spectroscopic and ab-initio theoretical approach to understand in detail the influence of fractional charge transfer as well as orbital hybridization on the supramolecular interactions between the intercalant molecules and the nanocarbons in the presence of molecular acceptors like $FeCl_3$ from which work is already in progress.

Finally, deciding to go trough into doped graphene, the study of nitrogen doped graphene was also performed. By using thermal CVD and a combination of nitrogen precursors, we prepared N-doped graphene with different amounts of N incorporation (0.2-3.8 at. %). XPS confirmed that the nitrogen is substitutionally doped in the hexagonal lattice in graphitic or non-graphitic configurations. Further, we showed that nitrogen bonded in the graphitic configuration (sample S2) leads to subtle changes in the Raman spectrum of graphene while nitrogen doped in the non-graphitic configuration (samples S1 and S3) leads to the activation of D and D$'$ bands with a concomitant downshift in the G$'$ band frequency. We attribute such effects in Raman spectra to the presence of strong electron phonon renormalization in S1 and S2.

Bibliography

[1] A. K. Geim and K. S. Novoselov. The rise of graphene. *Nat. Mater.*, 6:183–191, 2007.

[2] S. Mouras, A. Hamwi, D. Djurado, and J. C. Cousseins. Synthesis of 1st stage graphite-intercalation compounds with fluorides. *Rev. Chim. Miner.*, 24:572–582, 1987.

[3] R. E. Peierls. Quelques proprietes typiques des corpses solides. *Ann. I. H. Poincare*, 5:177–222, 1935.

[4] L. D. Landau. Theorie der phasenumwandlungen ii. *Phys. Z. Sowjetunion*, 11:26–35, 1937.

[5] H. W. Kroto, A. W. Allaf, and S. P. Balm. C_{60} - buckminsterfullerene. *Chem. Rev.*, 91:1213–1235, 1991.

[6] S. Iijima. Helical microtubules of graphitic carbon. *Nature*, 354:56–58, 1991.

[7] J. C. Meyer, A. K. Geim, M. I. Katsnelson, K. S. Novoselov, T. J. Booth, and S. Roth. The structure of suspended graphene sheets. *Nature*, 446:60–63, 2007.

[8] K. I. Bolotin, K. J. Sikes, J. Hone, H. L. Stormer, and P. Kim. Temperature-dependent transport in suspended graphene. *Phys. Rev. Lett.*, 101:096802, 2008.

[9] K. I. Bolotin, K. J. Sikes, Z. Jiang, M. Klima, G. Fudenberg, J. Hone, P. Kim, and H. L. Stormer. Ultrahigh electron mobility in suspended graphene. *Solid State Commun.*, 146:351–355, 2008.

[10] K. S. Novoselov, D. Jiang, F. Schedin, T. J. Booth, V. V. Khotkevich, S. V. Morozov, and A. K. Geim. Two-dimensional atomic crystals. *Proc. Natl. Acad. Sci. U. S. A.*, 102:10451–10453, 2005.

[11] K. S. Novoselov, A. K. Geim, S. V. Morozov, D. Jiang, Y. Zhang, S. V. Dubonos, I. V. Grigorieva, and A. A. Firsov. Electric field effect in atomically thin carbon films. *Science*, 306:666–669, 2004.

[12] Y. B. Zhang, Y. W. Tan, H. L. Stormer, and P. Kim. Experimental observation of the quantum hall effect and berry's phase in graphene. *Nature*, 438:201–204, 2005.

[13] A. A. Balandin, S. Ghosh, W. Bao, I. Calizo, D. Teweldebrhan, F. Miao, and C. N. Lau. Superior thermal conductivity of single-layer graphene. *Nano Lett.*, 8:902–907, 2008.

[14] I. W. Frank, D. M. Tanenbaum, A. M. Van der Zande, and P. L. McEuen. Mechanical properties of suspended graphene sheets. *J. Vac. Sci. Technol., B*, 25:2558–2561, 2007.

[15] K. S. Novoselov, E. McCann, S. V. Morozov, V. I. Fal'ko, M. I. Katsnelson, U. Zeitler, D. Jiang, F. Schedin, and A. K. Geim. Unconventional quantum hall effect and berry's phase of 2π in bilayer graphene. *Nat. Phys.*, 2:177–180, 2006.

[16] Z. Jiang, Y. Zhang, H. L. Stormer, and P. Kim. Quantum hall states near the charge-neutral dirac point in graphene. *Phys. Rev. Lett.*, 99:106802, 2007.

[17] Barbaros Oezyilmaz, Pablo Jarillo-Herrero, Dmitri Efetov, Dmitry A. Abanin, Leonid S. Levitov, and Philip Kim. Electronic transport and quantum hall effect in bipolar graphene p-n-p junctions. *Phys. Rev. Lett.*, 99:166804, 2007.

[18] K. S. Novoselov, Z. Jiang, Y. Zhang, S. V. Morozov, H. L. Stormer, U. Zeitler, J. C. Maan, G. S. Boebinger, P. Kim, and A. K. Geim. Room-temperature quantum hall effect in graphene. *Science*, 315:1379–1379, 2007.

[19] Z. Jiang, Y. Zhang, Y. . W. Tan, H. L. Stormer, and P. Kim. Quantum hall effect in graphene. *Solid State Commun.*, 143:14–19, 2007.

[20] F. Schedin, A. K. Geim, S. V. Morozov, E. W. Hill, P. Blake, M. I. Katsnelson, and K. S. Novoselov. Detection of individual gas molecules adsorbed on graphene. *Nat. Mater.*, 6:652–655, 2007.

[21] K. Novoselov and A. Geim. Graphene detects single molecule of toxic gas. *Materials Technology*, 22:178–179, 2007.

[22] K. S. Novoselov, V. I. Falko, L. Colombo, P. R. Gellert, M. G. Schwab, and K. Kim. A roadmap for graphene. *Nature*, 490:192–200, 2012.

[23] Rod Ruoff. Calling all chemists. *Nat. Nanotechnol.*, 3:10–11, 2008.

[24] D. Li and R. B. Kaner. Materials science - graphene-based materials. *Science*, 320:1170–1171, 2008.

[25] S. Cui, S. Mao, G. Lu, and J. Chen. Graphene coupled with nanocrystals: Opportunities and challenges for energy and sensing applications. *J. Phys. Chem. Lett.*, 4:2441–2454, 2013.

[26] T. Ramanathan, A. A. Abdala, S. Stankovich, D. A. Dikin, M. Herrera-Alonso, R. D. Piner, D. H. Adamson, H. C. Schniepp, X. Chen, R. S. Ruoff, S. T. Nguyen, I. A. Aksay, R. K. Prud'homme, and L. C. Brinson. Functionalized graphene sheets for polymer nanocomposites. *Nat. Nanotechnol.*, 3:327–331, 2008.

[27] M. S. Dresselhaus and G. Dresselhaus. Intercalation compounds of graphite. *Adv. Phys.*, 30(2):139–326, 1981.

[28] N. Emery, C. Herold, M. d'Astuto, V. Garcia, C. Bellin, J. F. Mareche, P. Lagrange, and G. Loupias. Superconductivity of bulk CaC_6. *Phys. Rev. Lett.*, 95:087003, 2005.

[29] P. R. Buseck and B. J. Huang. Conversion of carbonaceous material to graphite during metamorphism. *Geochim. Cosmochim. Acta*, 49:2003–2016, 1985.

[30] Prasanta Sanyal, B. C. Acharya, S. K. Bhattacharya, A. Sarkar, S. Agrawal, and M. K. Bera. Origin of graphite, and temperature of metamorphism in precambrian eastern ghats mobile belt, orissa, india: A carbon isotope approach. *Asian J. Earth Sci.*, 36:252–260, 2009.

[31] John W. Anthony, Richard A. Bideaux, Kenneth W. Bladh, and Monte C. Nichols. *Handbook of Mineralogy. I (Elements, Sulfides, Sulfosalts)*. Chantilly, VA, US: Mineralogical Society of America., 1990.

[32] D. D. L. Chung. Review graphite. *J. Mater. Sci.*, 37:1475–1489, 2002.

[33] Pierre Delhaes. *Carbon-based Solids and Materials*. ISTE Ltd and John Wiley & Sons, 2011.

[34] J. D. Bernal. The structure of graphite. *Proc. R. Soc. London, Ser. A*, 106:749–773, 1924.

[35] M. J. Allen, V. C. Tung, and R. B. Kaner. Honeycomb carbon: A review of graphene. *Chem. Rev.*, 110:132–145, 2010.

[36] S. Bae, H. Kim, Y. Lee, X. Xu, J. S. Park, Y. Zheng, J. Balakrishnan, T. Lei, H. R. Kim, Y. I. Song, Y. J. Kim, K. S. Kim, B. Ozyilmaz, J. H. Ahn, B. H. Hong, and S. Iijima. Roll-to-roll production of 30-inch graphene films for transparent electrodes. *Nat. Nanotechnol.*, 5:574–578, 2010.

[37] Kinam Kim, Jae-Young Choi, Taek Kim, Seong-Ho Cho, and Hyun-Jong Chung. A role for graphene in silicon-based semiconductor devices. *Nature*, 479:338–344, 2011.

[38] S. Garaj, W. Hubbard, A. Reina, J. Kong, D. Branton, and J. A. Golovchenko. Graphene as a subnanometre trans-electrode membrane. *Nature*, 467:190–U73, 2010.

[39] Hook J.R. and Hall H.E. *Solid State Physics (2nd Edition)*. John Wiley & Sons, 2010.

[40] Ruiting Zheng, Jinwei Gao, Jianjian Wang, and Gang Chen. Reversible temperature regulation of electrical and thermal conductivity using liquid-solid phase transitions. *Nat. Commun.*, 2:289, 2011.

[41] P. R. Wallace. The band theory of graphite. *Phys. Rev.*, 71:622–634, 1947.

[42] J.-C. Charlier, P.C. Eklund, J. Zhu, and A.C. Ferrari. Electron and phonon properties of graphene: Their relationship with carbon nanotubes. In *Carbon Nanotubes*, volume 111, pages 673–709. Springer Berlin Heidelberg, 2008.

[43] G. W. Semenoff. Condensed-matter simulation of a three-dimensional anomaly. *Phys. Rev. Lett.*, 53:2449–2452, 1984.

[44] P. Avouris, Z. Chen, and V. Perebeinos. Carbon-based electronics. *Nat. Nanotechnol.*, 2:605–615, 2007.

[45] S. Hernandez-Ortiz, G. Murguia, and A. Raya. Hard and soft supersymmetry breaking for 'graphinos' in uniform magnetic fields. *J. Phys.: Condens. Matter*, 24:015304, 2012.

[46] J. C. Slonczewski and P. R. Weiss. Band structure of graphite. *Phys. Rev.*, 109:272–279, 1958.

[47] J. W. McClure. Diamagnetism of graphite. *Phys. Rev.*, 104:666–671, 1956.

[48] S. Reich, J. Maultzsch, C. Thomsen, and P. Ordejon. Tight-binding description of graphene. *Phys. Rev. B*, 66:035412, 2002.

[49] R. Saito, G. Dresselhaus, and M. S. Dresselhaus. *Physical Properties of Carbon Nanotubes*. Imperial College Press, 1998.

[50] A. Grueneis, C. Attaccalite, L. Wirtz, H. Shiozawa, R. Saito, T. Pichler, and A. Rubio. Tight-binding description of the quasiparticle dispersion of graphite and few-layer graphene. *Phys. Rev. B*, 78:205425, 2008.

[51] A. Allard and L. Wirtz. Graphene on metallic substrates: Suppression of the kohn anomalies in the phonon dispersion. *Nano Lett.*, 10:4335–4340, 2010.

[52] M. S. Dresselhaus. *Graphite and Precursors*. Gordon and Breach Science Publishers, 2001.

[53] M. Orchin and H. H. Jaffe. Symmetry, point groups, and character tables .1. symmetry operations and their importance for chemical problems. *J. Chem. Educ.*, 47:246–&, 1970.

[54] G. Turell. *Infrared and Raman spectra of Crystals*. Academic Press, New York, 1972.

[55] S. Reich and C. Thomsen. Raman spectroscopy of graphite. *Philos. Trans. R. Soc., A*, 362:2271–2288, 2004.

[56] M. S. Dresselhaus, G. Dresselhaus, P. C. Eklund, and D. D. L. Chung. Lattice-vibrations in graphite and intercalation compounds of graphite. *Mater. Sci. Eng.*, 31:141–152, 1977.

[57] J. C. Chacon-Torres, A. Y. Ganin, M. J. Rosseinsky, and T. Pichler. Raman response of stage-1 graphite intercalation compounds revisited. *Phys. Rev. B*, 86:075406, 2012.

[58] P. Lespade, R. Aljishi, and M. S. Dresselhaus. Model for raman-scattering from incompletely graphitized carbons. *Carbon*, 20:427–431, 1982.

[59] P. C. Eklund, J. M. Holden, and R. A. Jishi. Vibrational-modes of carbon nanotubes - spectroscopy and theory. *Carbon*, 33:959–972, 1995.

[60] R. J. Nemanich, S. A. Solin, and D. Guerard. Raman-scattering from intercalated donor compounds of graphite. *Phys. Rev. B*, 16:2665–2672, 1977.

[61] Andrea C. Ferrari and Denis M. Basko. Raman spectroscopy as a versatile tool for studying the properties of graphene. *Nat. Nanotechnol.*, 8:235–246, 2013.

[62] A. Grueneis, C. Attaccalite, A. Rubio, D. V. Vyalikh, S. L. Molodtsov, J. Fink, R. Follath, W. Eberhardt, B. Buechner, and T. Pichler. Electronic structure and electron-phonon coupling of doped graphene layers in KC_8. *Phys. Rev. B*, 79:205106, 2009.

[63] J. Maultzsch, S. Reich, and C. Thomsen. Double-resonant raman scattering in graphite: Interference effects, selection rules, and phonon dispersion. *Phys. Rev. B*, 70:155403, 2004.

[64] J. Maultzsch, S. Reich, C. Thomsen, H. Requardt, and P. Ordejon. Phonon dispersion in graphite. *Phys. Rev. Lett.*, 92:075501, 2004.

[65] M. Mohr, J. Maultzsch, E. Dobardzic, S. Reich, I. Milosevic, M. Damnjanovic, A. Bosak, M. Krisch, and C. Thomsen. Phonon dispersion of graphite by inelastic x-ray scattering. *Phys. Rev. B*, 76:035439, 2007.

[66] L. Wirtz and A. Rubio. The phonon dispersion of graphite revisited. *Solid State Commun.*, 131:141–152, 2004.

[67] N. Bonini, M. Lazzeri, N. Marzari, and F. Mauri. Phonon anharmonicities in graphite and graphene. *Phys. Rev. Lett.*, 99:176802, 2007.

[68] D. L. Rousseau, R. P. Bauman, and S. P. S. Porto. Normal mode determination in crystals. *J. Raman Spectrosc.*, 10:253–290, 1981.

[69] A. Grueneis, J. Serrano, A. Bosak, M. Lazzeri, S. L. Molodtsov, L. Wirtz, C. Attaccalite, M. Krisch, A. Rubio, F. Mauri, and T. Pichler. Phonon surface mapping of graphite: Disentangling quasi-degenerate phonon dispersions. *Phys. Rev. B*, 80:085423, 2009.

[70] S. Piscanec, M. Lazzeri, F. Mauri, A. C. Ferrari, and J. Robertson. Kohn anomalies and electron-phonon interactions in graphite. *Phys. Rev. Lett.*, 93:185503, 2004.

[71] M. S. Dresselhaus, G. Dresselhaus, and A. Jorio. *Group Theory: Application to the Physics of Condensed Matter*. Springer, 2008.

[72] A. C. Ferrari. Raman spectroscopy of graphene and graphite: Disorder, electron-phonon coupling, doping and nonadiabatic effects. *Solid State Commun.*, 143:47–57, 2007.

[73] J. Kurti, V. Zolyomi, A. Gruneis, and H. Kuzmany. Double resonant raman phenomena enhanced by van hove singularities in single-wall carbon nanotubes. *Phys. Rev. B*, 65:165433, 2002.

[74] M. A. Pimenta, G. Dresselhaus, M. S. Dresselhaus, L. G. Cancado, A. Jorio, and R. Saito. Studying disorder in graphite-based systems by raman spectroscopy. *Phys. Chem. Chem. Phys.*, 9:1276, 2007.

[75] L. M. Malard, M. A. Pimenta, G. Dresselhaus, and M. S. Dresselhaus. Raman spectroscopy in graphene. *Phys. Rep.*, 473:51–87, 2009.

[76] IUPAC. *The "Gold book"*. Compendium of Chemical Terminology, 1997. "amphoteric".

[77] W. Zhao, P. H. Tan, J. Liu, and A. C. Ferrari. Intercalation of few-layer graphite flakes with fecl3: Raman determination of fermi level, layer by layer decoupling, and stability. *J. Am. Chem. Soc.*, 133:5941–5946, 2011.

[78] Y. Hernandez, V. Nicolosi, M. Lotya, F. M. Blighe, Z. Sun, S. De, I. T. McGovern, B. Holland, M. Byrne, Y. K. Gun'ko, J. J. Boland, P. Niraj, G. Duesberg, S. Krishnamurthy, R. Goodhue, J. Hutchison, V. Scardaci, A. C. Ferrari, and J. N. Coleman. High-yield production of graphene by liquid-phase exfoliation of graphite. *Nat. Nanotechnol.*, 3:563–568, 2008.

[79] P. J. J. Shaffault. *J. Prakt. Chem.*, 21:186–, 1841.

[80] W. Rüdorff and E. Schulze. über alkaligraphitverbindungen. *Z. Anorg. Chem.*, 277:156, 1954.

[81] N. B. Hannay, T. H. Geballe, B. T. Matthias, K. Andres, P. Schmidt, and D. Macnair. Superconductivity in graphitic compounds. *Phys. Rev. Lett.*, 14:225, 1965.

[82] M. S. Dresselhaus and G. Dresselhaus. Intercalation compounds of graphite. *Adv. Phys.*, 51:1–186, 2002.

[83] G. L. Doll, M. H. Yang, and P. C. Eklund. Comparative optical study of the two-dimensional donor-type intercalation compounds graphite-KH_X and their binary counterparts C_8K and $C_{24}K$. *Phys. Rev. B*, 35:9790–9798, 1987.

[84] M. H. Yang and P. C. Eklund. Optical dielectric function of high-stage potassium graphite-intercalation compounds - experiment and theory. *Phys. Rev. B*, 38:3505–3516, 1988.

[85] C. A. Howard, M. P. M. Dean, and F. Withers. Phonons in potassium-doped graphene: The effects of electron-phonon interactions, dimensionality, and adatom ordering. *Phys. Rev. B*, 84:241404, 2011.

[86] T. E. Weller, M. Ellerby, S. S. Saxena, R. P. Smith, and N. T. Skipper. Superconductivity in the intercalated graphite compounds C_6Yb and C_6Ca. *Nat. Phys.*, 1:39–41, 2005.

[87] A. M. Dimiev, G. Ceriotti, N. Behabtu, D. Zakhidov, M. Pasquali, R. Saito, and J. M. Tour. Direct real-time monitoring of stage transitions in graphite intercalation compounds. *ACS Nano*, 7:2773–2780, 2013.

[88] J. G. Hooley. Physical-chemistry and mechanism of intercalation in graphite. *Mater. Sci. Eng.*, 31:17–24, 1977.

[89] J. E. Fischer and T. E. Thompson. Graphite intercalation compounds. *Phys. Today*, 31:36–&, 1978.

[90] M. Inagaki. Applications of graphite-intercalation compounds. *J. Mater. Res.*, 4:1560–1568, 1989.

[91] M. Endo. *Graphite intercalation compounds and applications*. Oxford University Press, 2003.

[92] L. M. Viculis, J. J. Mack, and R. B. Kaner. A chemical route to carbon nanoscrolls. *Science*, 299:1361–1361, 2003.

[93] L. M. Viculis, J. J. Mack, O. M. Mayer, H. T. Hahn, and R. B. Kaner. Intercalation and exfoliation routes to graphite nanoplatelets. *J. Mater. Chem.*, 15:974–978, 2005.

[94] G. R. Hennig. Interstitial compounds of graphite. In *Progress in Inorganic Chemistry*, pages 125–205. John Wiley & Sons, Inc., 2007.

[95] L. B. Ebert. Intercalation compounds of graphite. *Annu. Rev. Mater. Sci.*, 6:181–211, 1976.

[96] E. Stumpp. Intercalation of metal chlorides and bromides into graphite. *Mater. Sci. Eng.*, 31:53–59, 1977.

[97] D. E. Nixon and G. S. Parry. Expansion of carbon-carbon bond length in potassium graphites. *J. Phys. C: Solid State Phys.*, 2:1732–&, 1969.

[98] S. A. Solin. Raman and ir studies of graphite intercalates. *Physica 99B*, page 443, 1980.

[99] S. A. Solin and N. Caswell. Raman-scattering from alkali graphite-intercalation compounds. *J. Raman Spectrosc.*, 10:129–135, 1981.

[100] S. A. Solin. *The Nature and Structural Properties of Graphite Intercalation Compounds*. John Wiley & Sons, Inc., 1982.

[101] N. Daumas and A. Herold. Relations between phase concept and reaction mechanics in graphite insertion compounds. *C. R. Seances Acad. Sci., Ser. C*, 268:373–375, 1969.

[102] S. Pisana, M. Lazzeri, C. Casiraghi, K. S. Novoselov, A. K. Geim, A. C. Ferrari, and F. Mauri. Breakdown of the adiabatic born-oppenheimer approximation in graphene. *Nat. Mater.*, 6:198–201, 2007.

[103] A. M. Saitta, M. Lazzeri, M. Calandra, and F. Mauri. Giant nonadiabatic effects in layer metals: Raman spectra of intercalated graphite explained. *Phys. Rev. Lett.*, 100:226401, 2008.

[104] G. Hennig and L. Meyer. Search for low temperature superconductivity in graphite compounds. *Phys. Rev.*, 87:439–439, 1952.

[105] M. Kobayashi and I. Tsujikawa. Susceptibility fluctuation in superconducting 1st stage potassium graphite-intercalation compound near transition-temperature. *J. Phys. Soc. Jpn.*, 46:1945–1946, 1979.

[106] Y. Koike, H. Suematsu, K. Higuchi, and S. Tanuma. Superconductivity in graphite-alkali metal intercalation compounds. *Physica B&C*, 99:503–508, 1980.

[107] I. T. Belash, A. D. Bronnikov, O. V. Zharikov, and A. V. Palnichenko. Superconductivity of graphite-intercalation compound with lithium C_2Li. *Solid State Commun.*, 69:921–923, 1989.

[108] T. Enoki, S. Masatsugu, and E. Morinobu. *Graphite Intercalation Compounds and Applications*. Oxford University Press, 2003.

[109] R. M. Fleming, A. P. Ramirez, M. J. Rosseinsky, D. W. Murphy, R. C. Haddon, S. M. Zahurak, and A. V. Makhija. Relation of structure and superconducting transition-temperatures in A_3C_{60}. *Nature*, 352:787–788, 1991.

[110] A. F. Hebard, M. J. Rosseinsky, R. C. Haddon, D. W. Murphy, S. H. Glarum, T. T. M. Palstra, A. P. Ramirez, and A. R. Kortan. Superconductivity at 18-K in potassium-doped C_{60}. *Nature*, 350:600–601, 1991.

[111] M. J. Rosseinsky, A. P. Ramirez, S. H. Glarum, D. W. Murphy, R. C. Haddon, A. F. Hebard, T. T. M. Palstra, A. R. Kortan, S. M. Zahurak, and A. V. Makhija. Superconductivity at 28 k in Rb_xC_{60}. *Phys. Rev. Lett.*, 66:2830–2832, 1991.

[112] A. Y. Ganin, Y. Takabayashi, Y. Z. Khimyak, S. Margadonna, A. Tamai, M. J. Rosseinsky, and K. Prassides. Bulk superconductivity at 38K in a molecular system. *Nat. Mater.*, 7:367–371, 2008.

[113] M. Capone, M. Fabrizio, C. Castellani, and E. Tosatti. Colloquium: Modeling the unconventional superconducting properties of expanded A_3C_{60} fullerides. *Rev. Mod. Phys.*, 81:943–958, 2009.

[114] O. Gunnarsson. Superconductivity in fullerides. *Rev. Mod. Phys.*, 69:575–606, 1997.

[115] J. Winter and H. Kuzmany. Landau damping and lifting of vibrational degeneracy in metallic potassium fulleride. *Phys. Rev. B*, 53:655–661, 1996.

[116] M. Yao, V. Pischedda, and A. San Miguel. Raman study of the electron-phonon interaction in light alkali metal intercalated metallic fullerides. *J. Phys.: Condens. Matter*, 23:115701, 2011.

[117] C. M. Varma, J. Zaanen, and K. Raghavachari. Superconductivity in the fullerenes. *Science*, 254:989–992, 1991.

[118] M. Schlüter, M. Lannoo, M. Needels, G. A. Baraff, and D. Tomanek. Superconductivity in alkali intercalated C_{60}. *J. Phys. Chem. Solids*, 53:1473–&, 1992.

[119] J. Hlinka, I. Gregora, J. Pokorny, C. Herold, N. Emery, J. F. Mareche, and P. Lagrange. Lattice dynamics of CaC_6 by raman spectroscopy. *Phys. Rev. B*, 76:144512, 2007.

[120] J. S. Kim, R. K. Kremer, L. Boeri, and F. S. Razavi. Specific heat of the ca-intercalated graphite superconductor CaC_6. *Phys. Rev. Lett.*, 96:217002, 2006.

[121] D. G. Hinks, D. Rosenmann, H. Claus, M. S. Bailey, and J. D. Jorgensen. Large ca isotope effect in the CaC_6 superconductor. *Phys. Rev. B*, 75:014509, 2007.

[122] M. Calandra and F. Mauri. Theoretical explanation of superconductivity in C_6Ca. *Phys. Rev. Lett.*, 95:237002, 2005.

[123] I. I. Mazin, L. Boeri, O. V. Dolgov, A. A. Golubov, G. B. Bachelet, M. Giantomassi, and O. K. Andersen. Unresolved problems in superconductivity of CaC_6. *Phys. C*, 460:116–120, 2007.

[124] A. Grueneis, C. Attaccalite, A. Rubio, D. V. Vyalikh, S. L. Molodtsov, J. Fink, R. Follath, W. Eberhardt, B. Buechner, and T. Pichler. Angle-resolved photoemission study of the graphite intercalation compound KC_8: A key to graphene. *Phys. Rev. B*, 80:075431, 2009.

[125] Z. . H. Pan, J. Camacho, M. H. Upton, A. V. Fedorov, C. A. Howard, M. Ellerby, and T. Valla. Electronic structure of superconducting KC_8 and nonsuperconducting LiC_6 graphite intercalation compounds: Evidence for a graphene-sheet-driven superconducting state. *Phys. Rev. Lett.*, 106:187002, 2011.

[126] G. Csanyi, P. B. Littlewood, A. H. Nevidomskyy, C. J. Pickard, and B. D. Simons. The role of the interlayer state in the electronic structure of superconducting graphite intercalated compounds. *Nat. Phys.*, 1:42–45, 2005.

[127] D. Allender, J. Bray, and J. Bardeen. Model for an exciton mechanism of superconductivity. *Phys. Rev. B*, 7:1020–1029, 1973.

[128] I. I. Mazin. Intercalant-driven superconductivity in YbC_6 and CaC_6. *Phys. Rev. Lett.*, 95:227001, 2005.

[129] M. Calandra and F. Mauri. Origin of superconductivity of cac_6 and of other intercalated graphites. *Phys. Status Solidi B*, 243:3458–3463, 2006.

[130] P. C. Eklund and K. R. Subbaswamy. Analysis of breit-wigner line-shapes in the raman-spectra of graphite-intercalation compounds. *Phys. Rev. B*, 20:5157–5161, 1979.

[131] T. Valla, J. Camacho, Z. . H. Pan, A. V. Fedorov, A. C. Walters, C. A. Howard, and M. Ellerby. Anisotropic electron-phonon coupling and dynamical nesting on the graphene sheets in superconducting CaC_6 using angle-resolved photoemission spectroscopy. *Phys. Rev. Lett.*, 102:107007, 2009.

[132] C. A. Howard, M. P. M. Dean, and F. Withers. Tunable non-adiabatic renormalization of the phonons in heavily doped graphene. *ArXiv e-prints*, 2010.

[133] M. P. M. Dean, C. A. Howard, S. S. Saxena, and M. Ellerby. Nonadiabatic phonons within the doped graphene layers of XC_6 compounds. *Phys. Rev. B*, 81:045405, 2010.

[134] A. Mialitsin, J. S. Kim, R. K. Kremer, and G. Blumberg. Raman scattering from the CaC_6 superconductor in the presence of disorder. *Phys. Rev. B*, 79:064503, 2009.

[135] J. C. Chacon-Torres and T. Pichler. Defect modulated raman response of KC_8 single crystals. *Phys. Status Solidi B*, 248:2744, 2011.

[136] S. Bhaviripudi, X. Jia, M. S. Dresselhaus, and J. Kong. Role of kinetic factors in chemical vapor deposition synthesis of uniform large area graphene using copper catalyst. *Nano Lett.*, 10:4128–4133, 2010.

[137] Y. Pan, D. X. Shi, and H. J. Gao. Formation of graphene on ru(0001) surface. *Chin. Phys.*, 16:3151–3153, 2007.

[138] P. W. Sutter, J. I. Flege, and E. A. Sutter. Epitaxial graphene on ruthenium. *Nat. Mater.*, 7:406–411, 2008.

[139] X. Li, W. Cai, J. An, S. Kim, J. Nah, D. Yang, R. Piner, A. Velamakanni, I. Jung, E. Tutuc, S. K. Banerjee, L. Colombo, and R. S. Ruoff. Large-area synthesis of high-quality and uniform graphene films on copper foils. *Science*, 324:1312–1314, 2009.

[140] Kim K. S., Zhao Y., Jang H., Lee S. Y., Kim J. M., K. S. Kim, Ahn J. H., P. Kim, Choi J. Y., and Hong B. H. Large-scale pattern growth of graphene films for stretchable transparent electrodes. *Nature*, 457:706–10, 2009.

[141] A. Reina, S. Thiele, X. Jia, S. Bhaviripudi, M. S. Dresselhaus, J. A. Schaefer, and J. Kong. Growth of large-area single- and bi-layer graphene by controlled carbon precipitation on polycrystalline ni surfaces. *Nano Res.*, 2:509–516, 2009.

[142] A. Reina, X. Jia, J. Ho, D. Nezich, H. Son, V. Bulovic, M. S. Dresselhaus, and J. Kong. Large area, few-layer graphene films on arbitrary substrates by chemical vapor deposition. *Nano Lett.*, 9:30–35, 2009.

[143] Q. Yu, J. Lian, S. Siriponglert, H. Li, Y. P. Chen, and S. S. Pei. Graphene segregated on ni surfaces and transferred to insulators. *Appl. Phys. Lett.*, 93:113103, 2008.

[144] J. Vaari, J. Lahtinen, and P. Hautojarvi. The adsorption and decomposition of acetylene on clean and k-covered co(0001). *Catal. Lett.*, 44:43–49, 1997.

[145] C. Berger, Z. Song, X. Li, X. Wu, N. Brown, C. Naud, D. Mayou, T. Li, J. Hass, A. N. Marchenkov, E. H. Conrad, P. N. First, and W. A. de Heer. Electronic confinement and coherence in patterned epitaxial graphene. *Science*, 312:1191–1196, 2006.

[146] W. Strupinski, K. Grodecki, A. Wysmolek, R. Stepniewski, T. Szkopek, P. E. Gaskell, A. Grueneis, D. Haberer, R. Bozek, J. Krupka, and J. M. Baranowski. Graphene epitaxy by chemical vapor deposition on SiC. *Nano Lett.*, 11:1786–1791, 2011.

[147] P. Y. Huang, C. S. Ruiz-Vargas, A. M. van der Zande, W. S. Whitney, M. P. Levendorf, J. W. Kevek, J. S. Garg, S.and Alden, C. J. Hustedt, Y. Zhu, J. Park, P. L. McEuen, and D. A. Muller. Grains and grain boundaries in single-layer graphene atomic patchwork quilts. *Nature*, 469:389–+, 2011.

[148] C. N. R. Rao, K. S. Subrahmanyam, H. S. S. Ramakrishna Matte, and A. Govindaraj. Graphene: Synthesis, functionalization and properties. *Mod. Phys. Lett. B*, 25:427–451, 2011.

[149] Q. Yu, L. A. Jauregui, W. Wu, R. Colby, J. Tian, Z. Su, H. Cao, Z. Liu, D. Pandey, D. Wei, T. F. Chung, P. Peng, N. P. Guisinger, E. A. Stach, J. Bao, S. S. Pei, and Y. P. Chen. Control and characterization of individual grains and grain boundaries in graphene grown by chemical vapour deposition. *Nat. Mater.*, 10:443–449, 2011.

[150] X. Li, C. W. Magnuson, A. Venugopal, J. An, J. W. Suk, B. Han, M. Borysiak, W. Cai, A. Velamakanni, Y. Zhu, L. Fu, E. M. Vogel, E. Voelkl, L. Colombo, and R. S. Ruoff. Graphene films with large domain size by a two-step chemical vapor deposition process. *Nano Lett.*, 10:4328–4334, 2010.

[151] D. Wei, Y. Liu, Y. Wang, H. Zhang, L. Huang, and G. Yu. Synthesis of n-doped graphene by chemical vapor deposition and its electrical properties. *Nano Lett.*, 9:1752–1758, 2009.

[152] Z. Jin, J. Yao, C. Kittrell, and J. M. Tour. Large-scale growth and characterizations of nitrogen-doped monolayer graphene sheets. *ACS Nano*, 5:4112–4117, 2011.

[153] Z. Sun, Z. Yan, J. Yao, E. Beitler, Y. Zhu, and J. M. Tour. Growth of graphene from solid carbon sources. *Nature*, 468:549–552, 2010.

[154] L. S. Panchokarla, K. S. Subrahmanyam, S. K. Saha, Achutharao Govindaraj, H. R. Krishnamurthy, U. V. Waghmare, and C. N. R. Rao. Synthesis, structure, and properties of boron- and nitrogen-doped graphene. *Adv. Mater.*, 21:4726–+, 2009.

[155] X. Wang, X. Li, L. Zhang, Y. Yoon, P. K. Weber, H. Wang, J. Guo, and H. Dai. N-doping of graphene through electrothermal reactions with ammonia. *Science*, 324:768–771, 2009.

[156] J. Dai, J. Yuan, and P. Giannozzi. Gas adsorption on graphene doped with b, n, al, and s: A theoretical study. *Appl. Phys. Lett.*, 95:232105, 2009.

[157] Y. Zou, F. Li, Z. H. Zhu, M. W. Zhao, X. G. Xu, and X. Y. Su. An ab initio study on gas sensing properties of graphene and si-doped graphene. *Eur. Phys. J. B*, 81:475–479, 2011.

[158] J. C. Meyer, S. Kurasch, H. J. Park, V. Skakalova, D. Kuenzel, A. Gross, A. Chuvilin, G. Algara-Siller, S. Roth, T. Iwasaki, U. Starke, J. H. Smet, and U. Kaiser. Experimental analysis of charge redistribution due to chemical bonding by high-resolution transmission electron microscopy. *Nat. Mater.*, 10:209–215, 2011.

[159] L. Feng, Y. Chen, and L. Chen. Easy-to-operate and low-temperature synthesis of gram-scale nitrogen-doped graphene and its application as cathode catalyst in microbial fuel cells. *ACS Nano*, 5:9611–9618, 2011.

[160] H. M. Jeong, J. W. Lee, W. H. Shin, Y. J. Choi, H. J. Shin, J. K. Kang, and J. W. Choi. Nitrogen-doped graphene for high-performance ultracapacitors and the importance of nitrogen-doped sites at basal planes. *Nano Lett.*, 11:2472–2477, 2011.

[161] B. Guo, Q. Liu, E. Chen, H. Zhu, L. Fang, and J. R. Gong. Controllable n-doping of graphene. *Nano Lett.*, 10:4975–4980, 2010.

[162] D. Usachov, O. Vilkov, A. Grueneis, D. Haberer, A. Fedorov, V. K. Adamchuk, A. B. Preobrajenski, P. Dudin, A. Barinov, M. Oehzelt, C. Laubschat, and D. V. Vyalikh. Nitrogen-doped graphene: Efficient growth, structure, and electronic properties. *Nano Lett.*, 11:5401–5407, 2011.

[163] L. Zhao, R. He, K. T. Rim, T. Schiros, K. S. Kim, H. Zhou, C. Gutierrez, S. P. Chockalingam, C. J. Arguello, L. Palova, D. Nordlund, M. S. Hybertsen, D. R. Reichman, T. F. Heinz, P. Kim, A. Pinczuk, G. W. Flynn, and A. N. Pasupathy. Visualizing individual nitrogen dopants in monolayer graphene. *Science*, 333:999–1003, 2011.

[164] T. Cui, R. Lv, Z. H. Huang, H. Zhu, J. Zhang, Z. Li, Y. Jia, F. Kang, K. Wang, and D. Wu. Synthesis of nitrogen-doped carbon thin films and their applications in solar cells. *Carbon*, 49:5022–5028, 2011.

[165] R. Lv, T. Cui, M. S. Jun, Q. Zhang, A. Cao, D. S. Su, Z. Zhang, S. H. Yoon, J. Miyawaki, I. Mochida, and F. Kang. Open-ended, n-doped carbon nanotube-graphene hybrid nanostructures as high-performance catalyst support. *Adv. Funct. Mater.*, 21:999–1006, 2011.

[166] L. Qu, Y. Liu, J. B. Baek, and L. Dai. Nitrogen-doped graphene as efficient metal-free electrocatalyst for oxygen reduction in fuel cells. *ACS Nano*, 4:1321–1326, 2010.

[167] A. L. Elias, J. C. Carrero-Sanchez, H. Terrones, M. Endo, J. P. Laclette, and M. Terrones. Viability studies of pure carbon- and nitrogen-doped nanotubes with entamoeba histolytica: From amoebicidal to biocompatible structures. *Small*, 3:1723–1729, 2007.

[168] J. C. Carrero-Sanchez, A. L. Elias, R. Mancilla, G. Arrellin, H. Terrones, J. P. Laclette, and M. Terrones. Biocompatibility and toxicological studies of carbon nanotubes doped with nitrogen. *Nano Lett.*, 6:1609–1616, 2006.

[169] Y. Wang, Y. Shao, D. W. Matson, J. Li, and Y. Lin. Nitrogen-doped graphene and its application in electrochemical biosensing. *ACS Nano*, 4:1790–1798, 2010.

[170] Lv. Ruitao, L. Qing, A. R. Botello-Méndez, H. Takuya, W. Bei, B. Ayse, H. Qingzhen, A. L. Elías, R. Cruz-Silva, H. R. Gutiérrez, Y. A. Kim, M. Hiroyuki, Z. Jun, E. Morinobu, H. Terrones, J. C. Charlier, P. Minghu, and M. Terrones. Nitrogen-doped graphene: beyond single substitution and enhanced molecular sensing. *Sci. Rep.*, 2:1–8, 2012.

[171] M. N. Groves, A. S. W. Chan, C. Malardier-Jugroot, and M. Jugroot. Improving platinum catalyst binding energy to graphene through nitrogen doping. *Chem. Phys. Lett.*, 481:214–219, 2009.

[172] L. Zhang and Z. Xia. Mechanisms of oxygen reduction reaction on nitrogen-doped graphene for fuel cells. *J. Phys. Chem. C*, 115:11170–11176, 2011.

[173] Haibo Wang, Thandavarayan Maiyalagan, and Xin Wang. Review on recent progress in nitrogen-doped graphene: Synthesis, characterization, and its potential applications. *ACS Catal.*, 2:781–794, 2012.

[174] A. Das, S. Pisana, B. Chakraborty, S. Piscanec, S. K. Saha, U. V. Waghmare, K. S. Novoselov, H. R. Krishnamurthy, A. K. Geim, A. C. Ferrari, and A. K. Sood. Monitoring dopants by raman scattering in an electrochemically top-gated graphene transistor. *Nat. Nanotechnol.*, 3:210–215, 2008.

[175] R. S. Krishnan and R. K. Shankar. Raman effect - history of the discovery. *J. Raman Spectrosc.*, 10:1–8, 1981.

[176] C. Thomsen, S. Reich, and J. Maultzsch. Resonant raman spectroscopy of nanotubes. *Philos. Trans. R. Soc., A*, 362(1824):2337–2359, November 2004.

[177] H. Kuzmany. *Solid-State Spectroscopy: An Introduction*. Springer, 2010.

[178] C. Fantini, A. Jorio, M. Souza, M. S. Strano, M. S. Dresselhaus, and M. A. Pimenta. Optical transition energies for carbon nanotubes from resonant raman spectroscopy: Environment and temperature effects. *Phys. Rev. Lett.*, 93(14):147406, October 2004.

[179] U. Fano. Effects of configuration interaction on intensities and phase shifts. *Phys. Rev.*, 124:1866, 1961.

[180] A. Einstein. Generation and conversion of light with regard to a heuristic point of view. *Ann. Phys.*, 17:132–148, 1905.

[181] J. C. Green. Photoelectron-spectroscopy - study of valence bands in solids. *Annu. Rev. Phys. Chem.*, 28:161–183, 1977.

[182] I. Lindau and W. E. Spicer. Probing depth in photoemission and auger-electron spectroscopy. *J. Electron Spectrosc. Relat. Phenom.*, 3:409–413, 1974.

[183] R. Podila, J. Chacon-Torres, J. T. Spear, T. Pichler, P. Ayala, and A. M. Rao. Spectroscopic investigation of nitrogen doped graphene. *Appl. Phys. Lett.*, 101:123108, 2012.

[184] P. Giannozzi, S. Baroni, N. Bonini, M. Calandra, R. Car, C. Cavazzoni, D. Ceresoli, G. L. Chiarotti, M. Cococcioni, I. Dabo, A. Dal Corso, S. de Gironcoli, S. Fabris, G. Fratesi, R. Gebauer, U. Gerstmann, C. Gougoussis, A. Kokalj, M. Lazzeri, L. Martin-Samos, N. Marzari, F. Mauri, R. Mazzarello, S. Paolini, A. Pasquarello, L. Paulatto, C. Sbraccia, S. Scandolo, G. Sclauzero, A. P. Seitsonen, A. Smogunov, P. Umari, and R. M. Wentzcovitch. QUANTUM ESPRESSO: a modular and open-source software project for quantum simulations of materials. *J. Phys.: Condens. Matter*, 21:395502, 2009.

[185] M. Lazzeri, C. Attaccalite, L. Wirtz, and F. Mauri. Impact of the electron-electron correlation on phonon dispersion: Failure of LDA and GGA DFT functionals in graphene and graphite. *Phys. Rev. B*, 78:081406, 2008.

[186] I. Pocsik, M. Hundhausen, M. Koos, and L. Ley. Origin of the d peak in the raman spectrum of microcrystalline graphite. *J. Non-Cryst. Solids*, 227:1083–1086, 1998.

[187] P. H. Tan, L. An, L. Q. Liu, Z. X. Guo, R. Czerw, D. L. Carroll, P. M. Ajayan, N. Zhang, and H. L. Guo. Probing the phonon dispersion relations of graphite from the double-resonance process of stokes and anti-stokes raman scatterings in multiwalled carbon nanotubes. *Phys. Rev. B*, 66:245410, 2002.

[188] C. Thomsen and S. Reich. Doable resonant raman scattering in graphite. *Phys. Rev. Lett.*, 85:5214–5217, 2000.

[189] J. P. Perdew, J. A. Chevary, S. H. Vosko, K. A. Jackson, M. R. Pederson, D. J. Singh, and C. Fiolhais. Atoms, molecules, solids, and surfaces - applications of the generalized gradient approximation for exchange and correlation. *Phys. Rev. B*, 46:6671–6687, 1992.

[190] D. M. Basko and I. L. Aleiner. Interplay of coulomb and electron-phonon interactions in graphene. *Phys. Rev. B*, 77:041409, 2008.

[191] D. R. Hamann, M. Schluter, and C. Chiang. Norm-conserving pseudopotentials. *Phys. Rev. Lett.*, 43:1494–1497, 1979.

[192] G. Profeta, M. Calandra, and F. Mauri. Phonon-mediated superconductivity in graphene by lithium deposition. *Nat. Phys.*, pages 1–4, 2012.

[193] J. M. Zhang and P. C. Eklund. Optical transmission of graphite and potassium graphite intercalation compounds. *J. Mater. Res.*, 2:858–63, 1987.

[194] Thomas Pichler. *Optische und Infrarot-Spektroskopie an alkalimetall-dotieren Fulleriten (Thesis)*. University of Vienna, 1993.

[195] J. C. Chacon-Torres, A. Y. Ganin, M. J. Rosseinsky, and T. Pichler. De-intercalation process from stage-1 to stage-2 graphite intercalation compounds revisited. *Phys. Status Solidi B*, 249:2640–2643, 2012.

[196] J. C. Chacon-Torres, L. Wirtz, and T. Pichler. Manifestation of charged and strained graphene layers in the raman response of graphite intercalation compounds. *ACS Nano*, 2013. doi: 10.1021/nn403885k.

[197] R. Aljishi and G. Dresselhaus. Lattice-dynamical model for alkali-metal graphite-intercalation compounds. *Phys. Rev. B*, 26:4523, 1982.

[198] G. L. Doll, P. C. Eklund, and J. E. Fischer. Raman-scattering study of the high-frequency graphitic intralayer modes in li-graphite and the stage dependence of the mode frequency in donor graphite-intercalation compounds. *Phys. Rev. B*, 36:4940–4945, 1987.

[199] F. Tuinstra and J. L. Koenig. Raman spectrum of graphite. *J. Chem. Phys.*, 53:1126, 1970.

[200] A. C. Ferrari and J. Robertson. Interpretation of raman spectra of disordered and amorphous carbon. *Phys. Rev. B*, 61:14095–14107, 2000.

[201] L. Pietronero and S. Strässler. Theory of nonadiabatic superconductivity. *Europhys. Lett.*, 18:627–633, 1992.

[202] D. Guerard and A. Herold. Intercalation of lithium into graphite and other carbons. *Carbon*, 13:337–345, 1975.

[203] D. M. Basko, S. Piscanec, and A. C. Ferrari. Electron-electron interactions and doping dependence of the two-phonon raman intensity in graphene. *Phys. Rev. B*, 80:165413, 2009.

[204] M. Schluter, M. Lannoo, M. Needels, G. A. Baraff, and D. Tomanek. Electron-phonon coupling and superconductivity in alkali-intercalated C_{60} solid. *Phys. Rev. Lett.*, 68:526–529, 1992.

[205] W. L. McMillan. Transition temperature of strong-coupled superconductors. *Phys. Rev.*, 167:331–&, 1968.

[206] T. Valla and Z. Pan. *Physics and Applications of Graphene - Experiments; (Superconductivity and Electron-Phonon Coupling in Graphite Intercalation Compunds)*. InTech, 2011.

[207] S. Migge, G. Sandmann, D. Rahner, H. Dietz, and W. Plieth. Studying lithium intercalation into graphite particles via in situ raman spectroscopy and confocal microscopy. *J. Solid State Electrochem.*, 9:132–137, 2005.

[208] Y. Y. Wang, Z. H. Ni, T. Yu, Z. X. Shen, H. M. Wang, Y. H. Wu, W. Chen, and A. T. S. Wee. Raman studies of monolayer graphene: The substrate effect. *J. Phys. Chem. C*, 112:10637–10640, 2008.

[209] L. M. Malard, J. Nilsson, D. C. Elias, J. C. Brant, F. Plentz, E. S. Alves, A. H. Castro Neto, and M. A. Pimenta. Probing the electronic structure of bilayer graphene by raman scattering. *Phys. Rev. B*, 76:201401, 2007.

[210] D. Graf, F. Molitor, K. Ensslin, C. Stampfer, A. Jungen, C. Hierold, and L. Wirtz. Spatially resolved raman spectroscopy of single- and few-layer graphene. *Nano Lett.*, 7:238–242, 2007.

[211] J. Yan, Y. B. Zhang, P. Kim, and A. Pinczuk. Electric field effect tuning of electron-phonon coupling in graphene. *Phys. Rev. Lett.*, 98:166802, 2007.

[212] R. P. Vidano, D. B. Fischbach, L. J. Willis, and T. M. Loehr. Observation of raman band shifting with excitation wavelength for carbons and graphites. *Solid State Commun.*, 39:341–344, 1981.

[213] A. C. Ferrari, J. C. Meyer, V. Scardaci, C. Casiraghi, M. Lazzeri, F. Mauri, S. Piscanec, D. Jiang, K. S. Novoselov, S. Roth, and A. K. Geim. Raman spectrum of graphene and graphene layers. *Phys. Rev. Lett.*, 97:187401, 2006.

[214] Pedro Venezuela, Michele Lazzeri, and Francesco Mauri. Theory of double-resonant raman spectra in graphene: Intensity and line shape of defect-induced and two-phonon bands. *Phys. Rev. B*, 84:035433, 2011.

[215] C. Hartwigsen, W. Witschel, and E. Spohr. Charge density and charge transfer in stage-1 alkali-graphite intercalation compounds. *Phys. Rev. B*, 55:4953–4959, 1997.

[216] F. Ancilotto and F. Toigo. 1st principles study of potassium adsorption on graphite. *Phys. Rev. B*, 47:13713–13721, 1993.

[217] M. Lazzeri and F. Mauri. Nonadiabatic kohn anomaly in a doped graphene monolayer. *Phys. Rev. Lett.*, 97:266407, 2006.

[218] D. Ziegler, P. Gava, J. Guettinger, F. Molitor, L. Wirtz, M. Lazzeri, A. M. Saitta, A. Stemmer, F. Mauri, and C. Stampfer. Variations in the work function of doped single- and few-layer graphene assessed by kelvin probe force microscopy and density functional theory. *Phys. Rev. B*, 83:235434, 2011.

[219] A. Grueneis, C. Attaccalite, T. Pichler, V. Zabolotnyy, H. Shiozawa, S. L. Molodtsov, D. Inosov, A. Koitzsch, M. Knupfer, J. Schiessling, R. Follath, R. Weber, P. Rudolf, L. Wirtz, and A. Rubio. Electron-electron correlation in graphite: A combined angle-resolved photoemission and first-principles study. *Phys. Rev. Lett.*, 100:037601, 2008.

[220] T. Ohno and H. Kamimura. Band structures and charge-distributions along the c-axis of higher stage graphite-intercalation compounds. *J. Phys. Soc. Jpn.*, 52:223–232, 1983.

[221] C. Attaccalite, L. Wirtz, M. Lazzeri, F. Mauri, and A. Rubio. Doped graphene as tunable electron-phonon coupling material. *Nano Lett.*, 10:1172–1176, 2010.

[222] C. Stampfer, F. Molitor, D. Graf, K. Ensslin, A. Jungen, C. Hierold, and L. Wirtz. Raman imaging of doping domains in graphene on SiO_2. *Appl. Phys. Lett.*, 91:241907, 2007.

[223] For the phonon calculations, we used a "simplified" third stage GIC: KC_{36} where each of the three graphene layers contains 8 carbon atoms per unit cell. The K/C ratio is a factor 1.5 higher than in KC_{24} . We are thus probing the influence of intercalation on the phonon frequencies under rather more severe conditions. The phonons are calculated using density-functional perturbation theory as implemented in the quantum-espresso code. The in-plane and perpendicular lattice constants are the same as in the charge-density and band-structure calculations. We use a 15x15x4 k-point sampling for the GIC and 15x15x1 sampling for the isolated layer. A thermal (Gaussian) smearing of 0.02 Rydberg is applied to the occupation of the electronic bands.

[224] C. Metzger, S. Remi, M. Liu, S. V. Kusminskiy, A. H. Castro Neto, A. K. Swan, and B. B. Goldberg. Biaxial strain in graphene adhered to shallow depressions. *Nano Lett.*, 10:6–10, 2010.

[225] O. Frank, M. Mohr, J. Maultzsch, C. Thomsen, I. Riaz, R. Jalil, K. S. Novoselov, G. Tsoukleri, J. Parthenios, K. Papagelis, L. Kavan, and C. Galiotis. Raman 2D-Band splitting in graphene: Theory and experiment. *ACS Nano*, 5(3):2231–2239, 2011.

[226] M. Huang, H. Yan, C. Chen, D. Song, T. F. Heinz, and J. Hone. Phonon softening and crystallographic orientation of strained graphene studied by raman spectroscopy. *Proc. Natl. Acad. Sci. U. S. A.*, 106:7304–7308, 2009.

[227] L. Pietronero and S. Strassler. Bond-length change as a tool to determine charge-transfer and electron-phonon coupling in graphite-intercalation compounds. *Phys. Rev. Lett.*, 47:593–596, 1981.

[228] K. Ishioka, M. Hase, M. Kitajima, L. Wirtz, A. Rubio, and H. Petek. Ultrafast electron-phonon decoupling in graphite. *Phys. Rev. B*, 77:121402(R), 2008.

[229] A. Das, B. Chakraborty, S. Piscanec, S. Pisana, A. K. Sood, and A. C. Ferrari. Phonon renormalization in doped bilayer graphene. *Phys. Rev. B*, 79:155417, 2009.

[230] R. Parret, M. Paillet, J. R. Huntzinger, D. Nakabayashi, T. Michel, A. Tiberj, J. L. Sauvajol, and A. A. Zahab. In situ raman probing of graphene over a broad doping range upon rubidium vapor exposure. *ACS Nano*, 7:165–173, 2013.

[231] P. Ayala, R. Arenal, M. Ruemmeli, A. Rubio, and T. Pichler. The doping of carbon nanotubes with nitrogen and their potential applications. *Carbon*, 48:575–586, 2010.

[232] P. Ayala, J. Reppert, M. Grobosch, M. Knupfer, T. Pichler, and A. M. Rao. Evidence for substitutional boron in doped single-walled carbon nanotubes. *Appl. Phys. Lett.*, 96:183110, 2010.

[233] A. L. Elias, P. Ayala, A. Zamudio, M. Grobosch, E. Cruz-Silva, J. M. Romo-Herrera, J. Campos-Delgado, H. Terrones, T. Pichler, and M. Terrones. Spectroscopic characterization of n-doped single-walled carbon nanotube strands: An x-ray photoelectron spectroscopy and raman study. *J. Nanosci. Nanotechnol.*, 10:3959–3964, 2010.

[234] P. Ayala, A. Grueneis, T. Gemming, D. Grimm, C. Kramberger, M. H. Ruemmeli, F. L. Jr. Freire, H. Kuzmany, R. Pfeiffer, A. Barreiro, B. Buechner, and T. Pichler. Tailoring n-doped single and double wall carbon nanotubes from a nondiluted carbon/nitrogen feedstock. *J. Phys. Chem. C*, 111:2879–2884, 2007.

[235] G. Keskar, R. Rao, J. Luo, J. Hudson, J. Chen, and A. M. Rao. Growth, nitrogen doping and characterization of isolated single-wall carbon nanotubes using liquid precursors. *Chem. Phys. Lett.*, 412:269–273, 2005.

[236] L. G. Cancado, M. A. Pimenta, B. R. A. Neves, M. S. S. Dantas, and A. Jorio. Influence of the atomic structure on the raman spectra of graphite edges. *Phys. Rev. Lett.*, 93:247401, 2004.

[237] J. S. Park, A. Reina, R. Saito, J. Kong, G. Dresselhaus, and M. S. Dresselhaus. G' band raman spectra of single, double and triple layer graphene. *Carbon*, 47:1303–1310, 2009.

[238] Indhira O. Maciel, Neil Anderson, Marcos A. Pimenta, Achim Hartschuh, Huihong Qian, Mauricio Terrones, Humberto Terrones, Jessica Campos-Delgado, Apparao M. Rao, Lukas Novotny, and Ado Jorio. Electron and phonon renormalization near charged defects in carbon nanotubes. *Nat. Mater.*, 7:878–883, 2008.

List of Figures

List of Tables

Appendices

Appendix A

PUBLICATIONS

1. Chacon-Torres, J. C., Wirtz, L., and Pichler, T.
   Manifestation of charged and strained graphene layers in the Raman response of graphite intercalation compounds
   ACS Nano, 2013
   doi: 10.1021/nn403885k
2. Chacon-Torres, J. C., Ganin, A. Y., Rosseinsky, M. J., and Pichler, T.
   De-intercalation process from Stage-1 to Stage-2 graphite intercalation compounds revisited
   Physica Status Solidi (b) Basic Solid State Physics, 2012.
   doi: 10.1002/pssb.201200174
3. Podila, R., Chacon-Torres, J., Spear, J. T., T. Pichler, P. Ayala, and A. M. Rao
   Spectroscopic investigation of nitrogen doped graphene
   Applied Physics Letters, 2012.
   doi: 10.1063/1.4752736
4. Chacon-Torres, J. C., Ganin, A. Y., Rosseinsky, M. J., and Pichler, T.
   Raman response of stage-1 graphite intercalation compounds revisited
   Physical Review B, 2012.
   doi: 10.1103/PhysRevB.86.075406
5. Chacon-Torres, J. C., and Pichler, T.
   Raman response of KC_8 single crystals
   Physica Status Solidi (b) Basic Solid State Physics, 2011.
   doi: 10.1002/pssb.201100135

Appendix B

AWARDS

1. **Best Poster Award IWEPNM 2013**
   XXVII International Winter School on Electronic Properties of Materials (IWEPNM)
   Kirchberg in Tirol, Austria (02-09 March, 2013)

2. **"Insignia Bicentenario 2012" International Award**
   Guanajuatense Youth Institute, Mexico
   León, Guanajuato, Mexico (18 January, 2013)

3. **Best Poster Award SIWAN5 2012**
   5th Szeged International Workshop on Advances in Nanoscience 2012
   Szeged, Hungary (27 October, 2012)

Appendix C

CURRICULUM VITAE

CURRICULUM VITAE

Julio Cesar Chacón Torres

University of Vienna
Vienna, Austria

julio.chacon@univie.ac.at
Tel. +43 699 15041467

Personal Information

Gender – Man
Birthday – 15.10.1983
Place of birth – Mexico

Nationality – Mexican
Family status – Married

Research interests

My main interest as a researcher lies in the development of new materials, technologies, and the disentangling of scientific standards for the up-coming nanotechnology field. My expertise as Mechatronics Engineer focuses on the design of electronic circuits, RF and RS-232 communication systems, Pneumatic and Hydraulic actuators and sensors. During my PhD, I have synthesized and characterized novel materials like Graphene, Carbon Nanotubes, and Graphite Intercalation Compounds. The possibility to combine my expertise in Engineering and in Solid State Physics has attracted my attention to the so called Engineering Physics towards the new technology development. I consider myself a dedicated, and industrious researcher highly adaptable to multidisciplinary and diverse groups. Language skills: Spanish (Mutter tongue), English (Fluent - Write/Speak), and German (Basic).

Experience

- **PhD Student** University of Vienna
  Austria *Current - Graduation time August 2013*
  - Synthesis and characterization of Graphene and Graphite Intercalation Compounds.
  - Characterization equipment: Multifrequency Raman spectroscopy (HORIBA LabRaman), Photoemission spectroscopy (XPS, ARPES, UPS), and LEED.
  - Synchrotron Radiation experience at Bessy II - Berlin, Germany.
  - Basic knowledge of ab-initio calculations in ABINIT
- **PhD Student** Institute for Scientific and Technological Research of San Luis Potosi
  Mexico *2008 – 2010*
  - Synthesis and characterization of Multi-walled Carbon Nanotubes
  - Characterization equipment: electronic transmission and scanning microscopes (HRTEM, JEOL, and UHRSEM).
  - Specialized laboratories: FIB Dual Beam FEI HELIOS 600 NANOLAB, and Micro-Raman RENISHAW.
  - Programming analysis: Fortran, SIESTA, and Materials Studio under Linux environment.

- **Commercial and Service Manager at Pneumatic Division** Mangueras Pepes
  Consulting-Manager *Jan 2008 – Aug 2008*
  - Technical advisement to enterprises seeking system improvement regarding Pneumatic, Electro pneumatic and Actuator systems to enhance their machinery and lower their costs.

- **Electronics Technician** ACCSYS-3000
  Technician *Jan 2002 – Aug 2003*
  - Design, and development of RFID systems based in RS232 communication with Palms m100 for diverse applications at short-range.

Academic Qualifications

- **University of Vienna** Vienna, AUT
  PhD Materials Science in Electronic Properties of Materials *2010 – present*
  - Advisor: Prof. Dr. Thomas Pichler
  - Thesis: Theory and Spectroscopy on functionalized graphene and GICs
- **Institute for Scientific and Technological Research of San Luis Potosi** SLP, MEX
  PhD. Appied Sciences in Nanoscience and Nanotechnology *2008 – 2010*
  - Advisor: Dr. Yadira I. Vega Cantú
  - Thesis: Integration of nanocarbon structures and nanotubes into micro-fabricated magnetic devices
- **Tecnológico de Monterrey** León, Gto. MEX
  B.Sc. Mechatronics Engineering (IMT) *2001 – 2008*

Teaching Experience

- **Solid State Physics (260111-1)** University of Vienna
  Exercises *Winter 2011*
  - Created assignments, exercises, course notes, and taught the course.

Awards, Grants & Honours

Best Poster Award IWEPNM 2013 (Kirchberg in Tirol, Austria) 2013
"Insignia Bicentenario 2012" International Award (Guanajuato, Mex) 2013
Poster Award - Scientific merit and visual appeal (SIWAN 2012, Hungary) 2012
Doctoral Fellowship FWF-I377-N16 and OEAD Amadeus Program . . . . . 2010 – 2013
Doctoral Scholarship CONACyT . . . . . 2008 – 2010
Bachelor Scholarship (45 %) Tecnológico de Monterrey . . . . . 2001 – 2008
Undergraduate Scholarship EDUCAFIN, Mex . . . . . 2001 – 2008
Undergraduate Scholarship (90 %) Tecnológico de Monterrey . . . . . 1998 – 2001

Publications (available at www.jchacon.webs.com)

Peer-Reviewed Journal Articles

5. Chacon-Torres, J. C., Wirtz, L., and Pichler, T. Manifestation of charged and strained graphene layers in the Raman response of graphite intercalation compounds *ACS Nano*, 2013. Submitted

4. Chacon-Torres, J. C., Ganin, A. Y., Rosseinsky, M. J., and Pichler, T. De-intercalation process from Stage-1 to Stage-2 graphite intercalation compounds revisited *Physica Status Solidi (b) Basic Solid State Physics*, 2012. doi: 10.1002/pssb.201200174

3. Podila, R., Chacon-Torres, J., Spear, J. T., T. Pichler, P. Ayala, and A. M. Rao Spectroscopic investigation of nitrogen doped graphene *Applied Physics Letters*, 2012. doi: 10.1063/1.4752736

2. Chacon-Torres, J. C., Ganin, A. Y., Rosseinsky, M. J., and Pichler, T. Raman response of stage-1 graphite intercalation compounds revisited *Physical Review B*, 2012. doi: 10.1103/PhysRevB.86.075406

1. Chacon-Torres, J. C., and Pichler, T. Raman response of KC_8 single crystals *Physica Status Solidi (b) Basic Solid State Physics*, 2011. doi: 10.1002/pssb.201100135

Conference Proceedings

1. A. Torales-Rivera, O. Arzola and Chacón J. C. INGENIERÍA MECATRÓNICA: TENDENCIAS ACTUALES Y PERSPECTIVAS *Memories, 6th Meeting - Participation of women in science*, 2009.

Participation in Workshops and Conferences

- **14th Int. Conference on the Science and Application of Nanotubes** — Espoo, FI
  Dipoli Congress Center — *Jun 24 – Jun 28, 2013*
- **Int. Winterschool on Electronic Properties of Novel Materials** — Kirchberg, AUT
  Hotel Sonnalp — *Mar 02 – Mar 9, 2013*
- **5th Szeged International Workshop on Advances in Nanoscience** — Szeged, HUN
  Hunguest Hotel Forrás — *Oct 24 – Oct 27, 2012*
- **Int. Winterschool on Electronic Properties of Novel Materials** — Kirchberg, AUT
  Hotel Sonnalp — *Mar 03 – Mar 10, 2012*
- **Int. Winterschool on Electronic Properties of Novel Materials** — Kirchberg, AUT
  Hotel Sonnalp — *Feb 26 – Mar 05, 2011*
- **11th Int. Conference on the Science and Application of Nanotubes** — Montréal, CAN
  Hilton Montréal Bonaventure — *Jun 27 – Jul 2, 2010*
- **First National Workshop of users LINAN** — San Luis Potosí, MEX
  Institute for Scientific and Technological Research of San Luis Potosi — *Sep, 2009*
- **6th Meeting - Participation of women in science** — León, Gto. MEX
  Optics Research Center — *Aug, 2009*

Certifications and Accreditations

- **Pneumatics and Hydraulics NORGREN Course** — Guadalajara, MEX
  Gates Mexico — *2008*
- **Electric Machinery Course** — León Gto. MEX
  Tecnológico de Monterrey — *2001*

Language Skills

Spanish – Mother tongue English – Advanced (TOEFL iBT – 89) German – Basic (A2)